

UNIVERSITY OF CONCEPCIÓN

Faculty of Engineering

Department of chemical engineering

Advisor:

Ph.D. Katherina Fernández E.

Study of Graphitic Materials for Drug Delivery



Author: Toribio Figueroa Aguilar

Doctoral Thesis

A thesis submitted in fulfillment of the requirements for the degree of Doctorate in Engineering Sciences with a major in Chemical Engineering

Biomaterials Group

June 2020

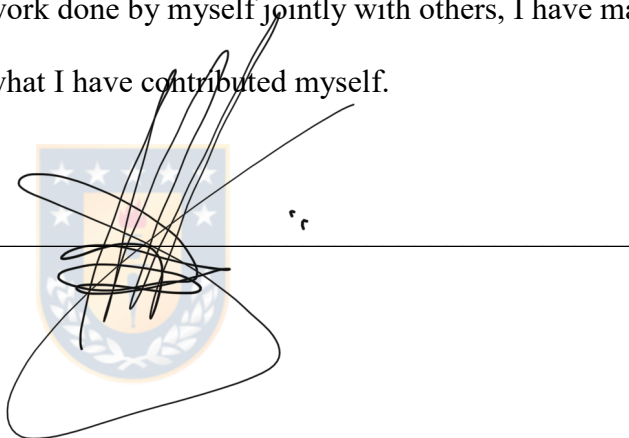
1.1 Declaration of authorship

I, Toribio Figueroa Aguilar, declare that this thesis titled “Study of graphitic materials for drug delivery” and the work presented in it is my own. I confirm that:

- This work was done wholly or mainly while in candidature for a research degree at this university.
- Where I have quoted from the work from others, I always gave the source. Except for such quotations, this thesis is entirely my work.
- I have acknowledged all of the primary sources of help.
- Where the thesis is based on work done by myself jointly with others, I have made clear what was done by others and what I have contributed myself.

Signed: _____

Date: 31/08/2020

A handwritten signature in black ink is written over a horizontal line. The signature is stylized and somewhat illegible. In the background, there is a faint watermark of a university crest featuring a shield with stars and a laurel wreath.

“Prejudice is an emotional commitment to ignorance.”

Nathan Rutstein

.



1.2 Abstract

In modern medicine, the development of new and efficient drug delivery systems is one of the most significant challenges facing science. Various drug carriers have been developed that protect the transported drug from hostile physiological environments and release it continuously at the site of application. For this purpose, materials based on graphene oxide (GO) are widely used, as GO is used as a precursor to suitably functionalized graphene. GO can be easily exfoliated into a few layers in a stable suspension in water, due to a large amount of hydrophilic oxygenated groups present in its structure. These groups also allow both covalent and non-covalent functionalization with polymers of well-known biocompatibility, and this improve the stability of GO in physiological solutions, are useful in drug transport and decrease its cytotoxicity. One of these polymers is chitosan (CS), which responds to pH by changing its solubility, is biocompatible and mucoadhesive. It also displays an impressive range of therapeutic functions such as hemostatic, antimicrobial, antitumor, and anti-inflammatory activity. Moreover, the GO-CS composites have superior mechanical properties and controllable drug delivery, making them a very promising drug delivery device.

We are interested in the use as phytodrug of proanthocyanidins (PAs), which have anti-cancer capacity and several properties, including antiviral, anti-inflammatory, cardio-protective, anti-diabetic and anti-aging effects, among others. However, the major drawback of such phytodrugs is their premature degradation in physiological media (gastric and intestinal fluids), short biological half-life, and early elimination from the body. These problems could be overcome immobilizing PAs on GO/CS based biomaterials.

Therefore, the aim of this study is to explore the development of a GO-CS biomaterials for the drug delivery of Pas from grape extracts (Ext.), characterizing them and determining their cytotoxicity in human cell models. The focus is on two possible applications of the extracts' properties, (i) a covalently bonded nanocomposite between GO and CS is developed (nanocomposite), for intravenous use, and (ii) a physically bonded hemostatic aerogel, for transdermal transport.

The synthesized materials were physicochemically characterized by Fourier transform infrared spectroscopy (FTIR), X-ray photoelectron spectroscopy (XPS), scanning electron microscopy (SEM), atomic force microscope (AFM), thermogravimetric analysis (TGA), UV-

visible spectroscopy (UV), Raman spectroscopy, X-ray diffraction (XRD), dynamic light scattering (DLS) and uniaxial compression test. We performed the loading and release of the extract of GO-CS materials in simulated physiological media. The cytotoxicity of the raw materials (GO and Ext.) and both developed materials were determined using a human kidney cell line (HEK 293) for the nanoparticles and human dermal fibroblasts for the aerogels.

Results for the nanocomposite, showed that a covalent union was successfully achieved between the GO and CS, with 44 wt. % CS in the material. The GO-CS nanocomposite was thermostable and presented an average diameter of 480 nm (by DLS). The Ext. loading capacity was approximately 20 wt. %, and under simulated physiological conditions, 28.4 wt.% Ext. was released. The GO-CS-Ext. was non-cytotoxic, presenting a 97% survival rate compared with 11% for the raw extract and 48% for the GO-CS nanocomposite at a concentration of 500 $\mu\text{g mL}^{-1}$ after 24 hours.

In the case of aerogels, those synthesized under basic conditions and loaded with grape extracts were more rigid, negatively charged, and had smaller pores than the not loaded acidic ones. In all aerogels, hemoglobin absorption was above 90% in the first 30 seconds. A higher density of adsorbed blood cells was observed on the aerogels with a higher amount of skin (SK) or seed (SD) extracts added, and the blood cell absorption was not selective to the change of pH. The release of the extract from the aerogels synthesized at basic pH reached 14% and 23.8% for the loading of SD and SK extracts, respectively; for the aerogels at acidic conditions the value was 24 %; however, it was dissolved in the media. The cytotoxicity of the aerogels on human dermal fibroblasts showed that alkaline SK extracts loaded aerogels were no cytotoxic, with cell viability above 90%.

Due to π - π stacking and hydrophilic interactions between the planar zones, oxygenated groups of GO, the amino group of CS and the the synthesized biomaterials were reasonably efficient in binding Ext., with high loading capacity and Ext. release from the composites. The GO-CS composites also reduces the cytotoxicity of PAs-rich Ext. Therefore, they represent a new platform for the sustained release of phytochemicals and have the potential to be used as hemostatic agents in wound treatment in the case of the aerogel.

1.3 Acknowledgments

The process of developing this doctorate has been a great one that involves the contribution of many people who motivate me and give support in their unique forms. So, in no particular order, I must thank:

To Professor Katherina who motivates me to be a scientist and rewards, it has supported my goals, and we have worked for the development of the glorious biomaterials laboratory.

To Toribio Figueroa (Father), without him, none of this is possible, who, together with my Mother Eugenia Aguilar, supports without further ado. Their love is infinite, and I hope to make them proud after they manage to have a son who is a "doctor".

To Jacqueline Parra, whom I admire and love, helps me to survive since I was a child and especially at this end of the world.

To Nicolás Almendras for being my safe place during most of this journey.

To Veronica Sanhueza, who guided me from the beginning and then cooperated with us as a laboratory, and then shared some lunch with us.

To Constanza Mellado with whom we started this path of graphene-based materials in the lab and learned by forcing things that are now basic in our lab.

To Camila Mora and her beautiful family with whom we shared carbonaceous, sponsored, and gastronomic experiences.

To Satchary Carmona who accompanies us in our work and supports us in moments of despair in the lab during our research.

To Jessica for her support and patience and her willingness to try to listen to me.

To the Biomaterials Lab for all the support and endurance we have

To Sebastian Guajardo, a great friend with whom we share knowledge, philosophy and can discuss everything. A great companion of drinks and forks and who has become a real friend.

1.4 Contents

1.1	Declaration of authorship.....	ii
1.2	Abstract.....	iv
1.3	Acknowledgments.....	vi
1.4	Contents	vii
1.5	Figures.....	x
1.6	Tables	xiii
1.7	Abbreviations.....	14
2	Scope of Work.....	17
2.1	Motivations	17
2.2	Hypothesis.....	20
2.3	Goals	20
2.3.1	Specific Goals	20
2.4	Thesis Layout.....	21
3	General Background	22
3.1	Graphene and Graphene Oxide.....	22
3.1.1	GO Synthesis and Modifications	24
3.1.2	Graphene-based materials cytotoxicity.....	29
3.1.3	Graphene oxide as a drug deliver device	32
3.2	Chitosan	34
3.2.1	CS applications	36
3.2.2	CS on drug delivery	36
3.3	Graphene Oxide and Chitosan Combinations.....	38
3.4	Proanthocyanidins.....	40

3.4.1	Characterization of PAs	42
3.4.2	Bioactivities of PAs.....	44
3.5	Coagulation Process on Artificial Surfaces.....	46
3.5.1	Protein Adsorption	46
3.5.2	Cell adhesion.....	48
3.6	References.....	49
4	Design and Characterization of Chitosan-Graphene Oxide Nanocomposites for the Delivery of Proanthocyanidins	56
4.1	Abstract.....	57
4.2	Introduction.....	58
4.3	Materials and Methods.....	60
4.3.1	Materials	60
4.3.2	País Grape Seed Extract Production	60
4.3.3	Preparation of the Chitosan-Grafted GO Nanocomposite (GO-CS).....	61
4.3.4	Nanocomposite Characterization	61
4.3.5	Loading and In-vitro Release of PAs from GO-CS	62
4.3.6	<i>In vitro</i> Cytotoxicity Study of the Nanocomposites.....	63
4.3.7	Statistics	64
4.4	Results.....	65
4.4.1	Characterization of GO-CS Nanocomposites	65
4.4.2	Loading and Release of PAs	70
4.4.3	Cell Viability.....	71
4.5	Discussion.....	73
4.6	Conclusion	76
4.7	References.....	77

5	Synthesis and Characterization of Flavan-3-ols Reinforced Graphene Oxide Chitosan Aerogels as Hemostatic Agent	80
5.1	Abstract	81
5.2	Introduction	82
5.3	Materials and Methods	84
5.3.1	Production of País grape seed extract	84
5.3.2	Preparation of GO-CS aerogels	84
5.3.3	GO-CS aerogels characterization	85
5.3.4	Absorption kinetics	86
5.3.5	Coagulation assay	87
5.3.6	Extract release profile	87
5.3.7	Cytotoxicity assay	88
5.3.8	Statistical analysis	89
5.4	Results and Discussion	90
5.4.1	Formation of GO-CS aerogels	90
5.4.2	Effects of addition of seed (SD) and skin (SK) extracts on aerogels	92
5.4.3	Characterization of GO-CS aerogels	95
5.4.4	Absorption capacities of the aerogels	98
5.4.5	Aerogels and media interaction	101
5.5	Conclusion	104
5.6	References	105
6	Conclusions	110
6.1	The direction of future work	111
6.2	Publications	111
6.3	Posters and Presentations	112

7	Appendix A.....	113
7.1	Phloroglucinolysis.....	114
7.2	Gel permeation chromatography (GPC).....	116
8	Appendix B.....	117

1.5 Figures

Figure 3-1	Graphene as a generator of all graphical forms.[6].....	22
Figure 3-2	Images of chemically converted graphene suspensions. a) GO in a glass bottle and b) is the dispersion after the addition of hydrazine. Below them, the reaction scheme that occurs. (where C is grey, O is red, and H is white) c) SEM images and d) AFM of chemically converted graphene on Si/SiO ₂ substrate.....	23
Figure 3-3	GO structure model (Georgakilas, 2014).....	24
Figure 3-4	a) AFM image in Tapping mode in 8 micrometer area per side of thermally exfoliated graphite sheets. b) 3D representation of graphite sheet. c) illustration of a different sheet in contact mode to measure dimensions. d) cross -section of a flatter area of GO sheet in b), cross- section of sheet in c). e) histogram of average sheet heights in a) [23].....	25
Figure 3-5	<i>TGA curve of natural graphite, reduced GO (chemically modified graphite sheets) and exfoliated GO [27]</i>	26
Figure 3-6	Deacetylation of chitin to chitosan.....	34
Figure 3-7	Chemical structure of flavonoids.....	40
Figure 3-8	Flavan-3-ol monomer examples. (From: Aron and Kennedy (2008)).....	41
Figure 3-9	Procyanidin example (From: Aron and Kennedy (2008)).....	42
Figure 3-10	Hypothetical reaction mechanism explaining acid-catalyzed cleavage of proanthocyanidins (from: Kenned and Jones (2001)).....	43
Figure 3-11	Protein adsorption on the surface of medical devices induces platelet adhesion, activation and aggregation. Factor XII adsorbed to the surface undergoes autoactivation, and the resulting factor XIIa converts prekallikrein to kallikrein and initiates coagulation and thrombin generation. In addition to inducing fibrin deposition on the surface, thrombin promotes platelet activation. Platelet aggregates deposited on the surface are stabilized by fibrin strands to form a platelet-fibrin thrombus. Kallikrein, thrombin and other coagulation enzymes activate complement,	

inducing a local inflammatory response. Leukocytes also adhere to the surface where they become activated and can contribute to both inflammation and thrombosis. [30].....	47
Figure 4-1 FTIR of GO (blue), CS (purple) and GO-CS (orange)	65
Figure 4-2 XPS spectra of GO (blue), CS (purple) and GO-CS (orange)	66
Figure 4-3 The N 1s band (black) of CS with the deconvoluted peaks of N-C (red), amine C-NH ₂ (green), amide N-C=O (yellow) and protonated C-NH ₄ ⁺ (blue) bonds.	66
Figure 4-4 The N 1s band (black) of GO-CS with the deconvoluted peaks of N-C (red), amine C-NH ₂ (green), amide N-C=O (yellow) and protonated C-NH ₄ ⁺ (blue) bonds.	67
Figure 4-5 TGA curves of GO (blue), CS (purple) and GO-CS (orange).....	68
Figure 4-6) SEM image of a GO sample	69
Figure 4-7 Extracted height profile of a GO-CS sample from AFM.	69
Figure 4-8 No-contact AFM image of a GO-CS sheet	69
Figure 4-9) UV-Vis absorption spectra of GO-CS (orange) and loaded GO-CS-Ext. (green).	70
Figure 4-10 Adsorption profile of Ext. on GO-CS in water (orange ●) and in vitro release profile of Ext. from GO-CS-Ext. (green ■) in PBS buffer (pH 7.4) at 37 °C.	71
Figure 4-11 In vitro cell toxicity assay. Relative cell viability of HEK cells treated with GO (blue ▲), Ext. (dark red ◆), GO-CS (orange ●) and GO-CS-Ext. (green ■) at different concentrations. Controls were cells without the addition of the studied samples.	72
Figure 5-1 FTIR spectra of graphene oxide (GO) and not loaded aerogels synthesized under basic conditions (GC0pH10).	90
Figure 5-2 XRD patterns of graphene oxide (GO) and not loaded aerogels synthesized under basic conditions (GC0pH10).	91
Figure 5-3 Raman spectrum of not loaded aerogel synthesized under basic conditions (GC0pH10).	92
Figure 5-4 Raman spectra comparison between loaded aerogel with 12% of seed extract (GC12pH10 SD) and not loaded aerogel (GC0pH10) both at pH 10.	93
Figure 5-5 Deconvolution of Raman D and G peaks for not loaded aerogel synthesized under basic conditions (GC0pH10).	94
Figure 5-6 Deconvolution of Raman D and G peaks for aerogels loaded with 12% SD extracts synthesized under basic conditions (GC12pH10 SD).	94

Figure 5-7 Elastic modulus calculated from the compression tests of SD extract loaded aerogel samples.....	95
Figure 5-8 SEM images of aerogels under acidic conditions, GC0pH4 (A); aerogel loaded with 6% SD extract, GC6pH4 SD (B); aerogel loaded with 12% SD extract, GC12pH4 SD (C); aerogel under alkaline conditions, GC0pH10 (D); aerogel loaded with 6% SD extract, GC6pH10 SD (E); and aerogel loaded with 12% SD extract, GC12pH10 SD (F).	97
Figure 5-9 Absorption of water (dotted lines) and PBS (straight lines) on aerogels synthesized under acidic conditions GC0pH4 (red) and alkaline conditions GC0pH10 (green) not loaded with extracts.	99
Figure 5-10 Hemoglobin UV absorbance of supernatants for blood absorption tests with aerogels.	99
Figure 5-11 SEM images of absorbed blood aerogels synthesized under basic conditions loaded with 6% SD extracts. (A), GC6pH10 SD; (B), GC12pH10 SD; (C), GC6pH10 SK; and (D), GC12pH10 SK aerogels.....	101
Figure 5-12 Release profiles of extracts from aerogels in PBS (pH 7.4, 37 °C)	102
Figure 5-13 Cell viability of human dermal fibroblast cells after 24 h of incubation with exudate from aerogels samples and GO, CS, and extracts.....	103
Figure 7-1 DTG curves of GO (blue), CS (purple) and GO-CS (orange).	116
Figure 8-1 Outline of the method for determining the pore size of aerogels (P1), (P2) and (P3) are the pore size determined from the SEM image using contrast comparison, and (1), (2), (3) and (4) are the determination of the wall width of the 3D aerogel structures	120

1.6 Tables

Table 3-1 Summary of covalent and non-covalent functionalities of graphene and GO for sustained drug delivery [4].	27
Table 3-2 Collection table of studies on pristine graphic materials	30
Table 3-3 In vitro toxicity table of covalently functional graphitic materials.	31
Table 3-4 In vivo toxicity of pristine and functionalized graphitic materials.	32
Table 5-1 Nomenclature for Aerogel samples.....	85
Table 5-2 Total Blood Count results of supernatant after blood absorption in aerogels.....	100
Table 7-1 Structure composition, mean degree of polymerization (mDP), average molecular weight (aMW) and concentration of the grape extract.	115
Table 7-2 Molecular weight distribution of grape seed extract.....	116
Table 8-1 Structure composition, mean degree of polymerization (mDP), average molecular weight (aMW) and concentration of the grape extract.	118
Table 8-2 Molecular weight distribution of grape seed extract	119



1.7 Abbreviations

ADP	Adenosine Diphosphate
AFM	Atomic Force Microscopy
aMW	Average Molecular Weight
C	(+)-Catechins
C.V.	Cell Viability
CPT	Camptothecin
CS	Chitosan
DAD	Diode Array Detectors
DD	Deacetylation Degree
DLS	Dynamic Light Scattering
DMEM	Dulbecco's Modified Eagles Medium
DMF	2,5-Dimethylfuran
DMSO	Dimethyl Sulfoxide
DNA	Deoxyribonucleic Acid
DOX	Doxorubicin
DTG	Differential Thermal Analysis
E	Elastic Modulus
e.V.	Electron Volt
EC	(-)-Epicatechin
ECG	Epigallocatechin
EDC	N-(3-Dimethylaminopropyl-N-Ethylcarbodiimide) Hydrochloride
EDTA	Ethylenediaminetetraacetic Acid
EGC-P	(-)-Epicatechin-Phloroglucinol
Ext.	Extract
F	Factor
FA	Folic Acid
FBS	Fetal Bovine Serum
FTIR	Fourier Transform Infrared Spectroscopy

GO	Graphene Oxide
GPC	Gel Permeation Chromatography
HPLC	High-Performance Liquid Chromatography
I.V.	Intravenous
LD	Lethal Dose
mDP	Mean Degree Of Polymerization
MEM	Minimum Essential Medium
MES	2-(N-Morpholino)Ethanesulfonic Acid
MTT	3-(4,5-Dimethylthiazol-2-Yl)-2,5-Diphenyltetrazolium Bromide
MWCO	Molecular-Weight Cutoff
NHS	N-Hydroxysuccinimide
NSAID	Non-Steroidal Anti-Inflammatory Drug
PAA	Poly(Acrylic) Acid
PAs	Proanthocyanidins
PBS	Phosphate-Buffered Saline
PEG	Polyethylene Glycol
PEI	Polyethylamine
PLL	Poly Lysine
PNIPAM	Poly(N-Isopropylacrylamide)
PSA	Polysebasic Anhydride
PVA	Polyvinyl Alcohol
RBC	Red Blood Cells
RNA	Ribonucleic Acid
RPM	Revolutions Per Minute
SD	Seed
SEM	Scanning Electron Microscopy
SK	Skin
STM	Scanning Tunneling Microscopy
SWGGO	Single Wall Graphene Oxide
TBC	Total Blood Counter
TEM	Transmission Electron Microscopy

TGA	Thermo Gravimetric Analysis
UV-Vis	Ultra Violet Visible
WBC	White Blood Cells
XPS	X-Ray Photoelectron Spectroscopy
XRD	X-Ray Diffraction



2 Scope of Work

2.1 Motivations

In today's medicine, the transport and sustained release mechanism of drugs may be more important than the drug itself. Most drugs suffer from poor solubility, rapid clearance from the bloodstream, failure to reach their target, or reduced permeability through the cell membrane [1]. For this purpose, sustained-release drug transport systems have been developed, which have the challenge of being able to cross obstacles such as endo- or epithelial membranes and also survive the attack of the host's defenses. To achieve these challenges, the carrier must offer some form of encapsulation or trapping of the drug, which takes it to a given location and then releases it [2].

Among the materials that we developed for this purpose are: aerogels, xerogels, nanoparticles, carbon nanotubes, liposomes, polymers, graphene, and graphene oxide [3], [4]. These materials have promising applications in medicine, as well as in interdisciplinary areas due to their chemical, physical and mechanical qualities [5]. One of these materials is graphene, a monoatomic layer of sp^2 carbons arranged in a two-dimensional network of hexagonal a, which has gained worldwide attention since its isolation in 2004. The structure and atomic distribution of graphene results in favorable properties, such as a high surface area ($2630 \text{ m}^2\text{g}^{-1}$), low resistance to load transport ($\sim 2.5 \times 10^5 \text{ cm}^2\text{V}^{-1} \text{ s}^{-1}$), excellent thermal conductivity in the basal plane ($\sim 5000 \text{ W m}^{-1} \text{ K}^{-1}$), among others [6]. However, this material also presents limitations such as difficulty for achieving high purity, the quality of exfoliation in monolayers, the prevention of self-aggregation of graphite-like structures, its still-debated biocompatibility and its activity in the physiological system. To improve these drawbacks materials derived from graphite have been developed, such as graphene oxide (GO), which have been chemically modified to improve its biocompatibility, prevent its aggregation and expand its use [5].

The medical applications of GO, including drug delivery and GO containing aerogels for blood adsorption to accelerate coagulation has been extensively researched in recent years, however, systematic assessment of its potential health risk is of paramount importance. Research shows that the cytotoxicity of GO films is due to the strong interaction between the cell membrane and the GO film, which results in physical damage to the cell membrane. This damage occurs during initial contact and is independent of the time of exposure [7]. In addition to dose-dependent toxicity, it is also essential to take into account the dependence on the environment (e.g. whether

or not there is a state of aggregation) and the mode of interaction with the cells (e.g. the difference between adherent cells and in suspension).

To use GO as a biomaterial pre-treatments are needed to increase dispersibility, stability and promote its biocompatibility with cells, including loaded drugs. To improve these aspects, functionalization techniques with biocompatible polymers such as Chitosan (CS), have been performed positioning these materials as candidates for sustained component release. CS is a biodegradable and positively charged polysaccharide, derived from the deacetylation of chitin, a polymer of N-acetylglucosamine found in the exoskeleton of crustaceans [8]. CS has been used to develop several biomaterials for tissue engineering and drug delivery due to its biocompatibility, mucoadhesivity, and impressive range of therapeutic functions such as hemostatic, antimicrobial, antitumor, and anti-inflammatory activity [9]–[11][12].

The GO and CS can be combined to yield favorable properties in a GO-CS composite, and used as a biocompatible drug delivery agent (or carrier) [13]. Typical forms of these composites for drug delivery have included composite films, hydrogels, aerogels, nanofibers, and nanoparticles [8]. Nanoparticles have mainly been used for the simultaneous release of genes and chemotherapy drugs [14]–[16]. Although such carriers are useful for the transport of chemical compounds, no studies have immobilized phytodrugs on GO-CS composites.

One promising phytodrug has arisen in the form of grape seed extract, which has a high concentration of proanthocyanidins (PAs). PAs are flavonols, a class of polyphenols that have different substitution patterns in the C₆-C₃-C₆ rings and are present in fruits and vegetables. PAs possess several bioactive effects, including antiviral, anti-inflammatory, cardioprotective, antidiabetic, anticancer, and anti-aging effects, among others [17]. Despite the promising biological activities of raw plant extracts, their poor solubility and stability, short biological half-life, and rapid elimination hinder their clinical application [18]. These aspects, together with concerns associated with the biocompatibility and toxicity of natural compounds, severely limit phytochemical therapeutic action, leading research interests towards the synthesis of systems that can effectively deliver these substances based on their applications. Specifically, in this work, we developed two new different materials for use in applications of the properties of PAs:

- The usage of nanoparticles offers the possibility to develop specially adapted delivery systems to improve the therapeutic efficacy of bioactive natural molecules

[19]. Indeed, nanocarriers have drawn increasing attention as potential alternatives to traditional formulation approaches, reducing toxicity, increasing bioavailability, and permitting site-specific targeted delivery [20]. Taking advantage of PAs, especially its cardio-protective, anti-cancer and anti-diabetic properties, it is desired to introduce it into the bloodstream intravenously protected by a carrier. Considering the kidney as the first biological barrier when entering the bloodstream, it is proposed to use a nanocomposite based on GO and CS covalently bonded that could deliver the grape extract rich in PAs.

- In the other hand, the use of CS-based hemostatic aerogels is well known, it is believed that the hemostatic property of CS arises from its electrostatic interaction with negatively-charged cell membranes of erythrocytes, leading to an erythrocyte agglutination and formation of a hemostatic plug at the site of the injury, preventing blood loss by adhering to tissues and injured vessels, sealing off the wound. However, chitosan-containing dressings have shown that the erythrocyte aggregates formed by CS are mechanically unstable [22]. For this reason, we are interested in improving the performance of CS aerogels, creating an aerogel based on GO with CS which, in addition to the grape extract, can promote coagulation and release the phytodrug into the very wound and promote its bioproperties. PAs possess several bioactive effects that can be used for wounds, including antiviral, anti-inflammatory, and antiaging effects, among others [21] which can synergize with the CS.

Thus, the purpose of this work is to develop GO and CS-based biomaterials to transport the grape extract, rich in PAs, and to study their physicochemical properties, their release capacities and cytotoxicity with human cellular models.

2.2 Hypothesis

The GO-based material that has been functionalized with CS can be used as a nano-carrier of the natural polyphenolic phytoextract thanks to its electrostatic interaction.

The use of GO and CS-based aerogels promotes blood clotting and absorbs it quickly due to their physicochemical properties. The addition of the extract to GO and CS-based aerogels improves their mechanical properties due to the rearrangement of their 3D structure.

2.3 Goals

The aim of this study is to development of a GO and CS biomaterials for the drug delivery of PAs from grape extracts, characterizing them and determining their cytotoxicity in human cell models. Focusing on two possible applications of the extracts' properties, a covalently bonded nanocomposite between GO and CS was developed for intravenous use and a physically bonded hemostatic aerogel for transdermal transport.

2.3.1 Specific Goals

For the development of nanocarrier:

- Develop GO-CS nanocomposite materials (carrier), characterizing its physical and chemical properties.
- Establish the loading capacity and release of the grape extracts immobilized in the carriers.
- Determine the cytotoxicity of the nanocomposite, the grape extract and their complex in a human kidney cell model (HEK 293)

In the case of the development of Aerogels:

- Develop GO-CS aerogels, characterizing and comparing their physical and chemical properties, and determining their capacity to absorb physiological media.
- Establish effects and the release amount of the phytoextract stabilized in the aerogel.
- Determine the cytotoxicity of the loaded aerogel in a human dermal fibroblast cell model.

2.4 Thesis Layout

The thesis is organized as follows:

Chapter 2 develops a description of the main components used in the manufacture of the materials used in medical research, which are graphene oxide, chitosan, and proanthocyanidins. Their synthesis methods, as well as their possible modifications for biomedical use together with their applications in drug delivery. Also, the combination of graphite and chitosan oxide in different composites and biomedical applications in drug delivery and hemostasis. Finally, in chapter 2, a section is devoted to reporting the coagulation phenomenon on composites that will be important for the discussion of the aerogels synthesized in this work, later on in chapter 4.

In chapter 3, we reported the synthesis and cytotoxicity of a nanocomposite composed of graphene oxide with chitosan that carries grape proanthocyanidins. This chapter is part of a manuscript published in the International Journal of Nanomedicine, issued online in February 2020, 15: 1229–1238. DOI :10.2147/IJN.S240305

Chapter 4 focuses on the synthesis of chitosan and graphite oxide-based aerogels loaded with grape extract, for use as a hemostatic agent. This chapter is part of a manuscript submitted for publication, which was sent to review by ACS Biomaterials Science & Engineering.

Chapter 5 presents the conclusions as well as some directions for future work.

3 General Background

3.1 Graphene and Graphene Oxide

Graphene is a single atom thick flat sheet of carbon sp^2 . In this sheet, the carbon atoms are arranged in hexagonal crystals in the shape of a honeycomb. This material has revolutionized the scientific boundaries of nanoscience and condensed matter physics due to its electrical, chemical and physical properties [5]. It is used as a theoretical model to explain the features of various carbon-based materials such as graphite, fullerenes and carbon nanotubes [6], outlined in Figure 3-1. Ideally, graphite should be single-layer and flat, but due to temperature, the sheets wrinkled. Graphene, with two or more layers, is being investigated with equal interest [3], this is because of the difficulty of achieving, in practice, graphene in monolayers. Graphene has been characterized by various microscopic and other physical techniques including atomic force microscopy (AFM) Transmission Electron Microscopy (TEM), Tunneling Microscopy (STM), X-Ray Diffraction

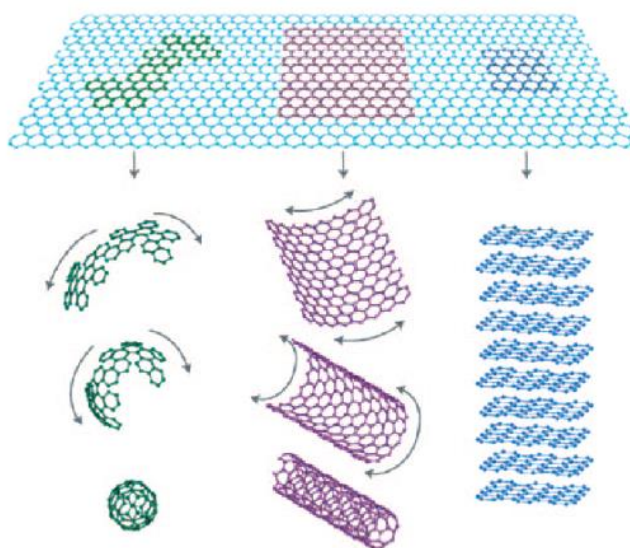


Figure 3-1 Graphene as a generator of all graphical forms.[6]

(XRD) and Raman Microscopy. Rao et al. (2009) reported that a graphite monolayer mounted on a silicon base with silicon dioxide, 300 nm thick, becomes visible in an optical microscope and besides in the AFM the number of layers can be directly determined by knowing the total thickness [6]. Images of graphene in STM and TEM are essential for determining its morphology and structure, while Raman microscopy is important for its chemical characterization. These

techniques will be used in this study to characterize the developed compounds and are introduced in chapter 5.2. The flat structure of graphene offers an excellent capacity to immobilize, with intermolecular forces, a large number of substances including metals, biomolecules, and drugs. It is not surprising then that graphene has generated significant interest in nanomedicine and biomedical applications, where it has served as an excellent platform for the sustained release of components [4]

Although graphene can be obtained by micromechanical exfoliation, chemical vapor deposition, preparation of colloidal suspensions in selected solvents, and by reduction of graphene oxide (GO) sheets as outlined in Figure 3-2. The latter method, using GO, which is obtained by the oxidation of graphite, contains a large amount of surface oxygen in the form of alcohol groups and carboxylic acids. The thermal or mechanical exfoliation of GO generates single-layer sheets (SWGGO) which can be reduced by hydrogen, hydrazine, or any reducing agent, to create single-layer graphite sheets. Schniepp et al. 2006 demonstrate that graphite oxide was peeling releases SWGO through the expansion of CO₂ released in the space between the layers during rapid heating [23]. Chemically modified graphite is produced in various forms, including hydrazine reduction of colloidal SWGO solutions in DMF/water solution or water only, and then electrostatic stabilization allows stable aqueous dispersion of SG.

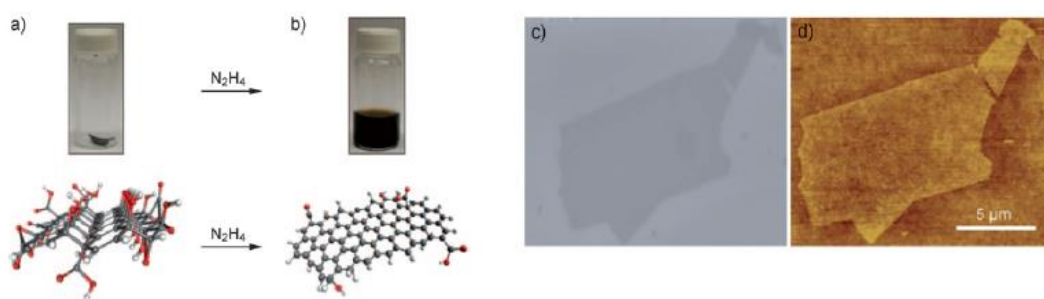


Figure 3-2 Images of chemically converted graphene suspensions. a) GO in a glass bottle and b) is the dispersion after the addition of hydrazine. Below them, the reaction scheme that occurs. (where C is grey, O is red, and H is white) c) SEM images and d) AFM of chemically converted graphene on Si/SiO₂ substrate

Graphene oxide (GO) is a two-dimensional material prepared from natural graphite that serves as a chemically converted precursor to graphene. GO can be easily exfoliated into laminar monolayers and form stable suspensions in water due to its hydrophilicity, which is due to the presence of oxygenated functional groups at the edges and in its basal plane [7]. Although it is

difficult to determine the exact structure of GO, it is clear that the aromatic carbon lattice of graphene is broken down by epoxy groups, alcohols, ketones and carboxyl groups (schematized in Figure 3-3), which allow GO to be functionalized by covalent and non-covalent processes, and thus to be a very versatile basis for the synthesis of functional materials [8]. Recently there has been a great deal of interest in research on GO and its derivatives for medical and biological applications (e.g. drug delivery) because of their biocompatibility, unique conjugate structure, large surface area, and relatively low cost [7]. This material was chosen to be the basis for the materials to be synthesized in this research, in line with the above, as it is more versatile than graphene for its functionalization and use as a nanocarrier.

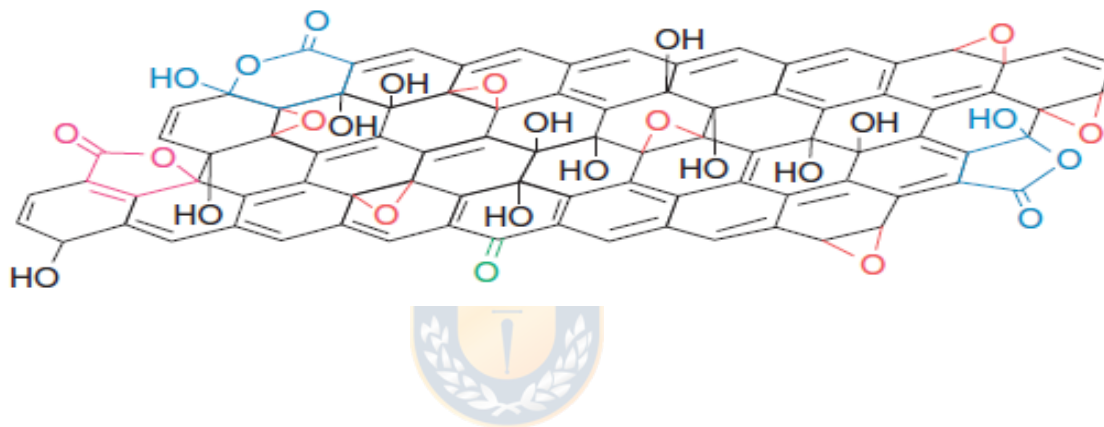


Figure 3-3 GO structure model (Georgakilas, 2014)

3.1.1 GO Synthesis and Modifications

The most common source of graphite used for synthetic chemical reactions, including oxidation, is sheet-ground graphite, which occurs naturally in the mineral and is purified to remove heteroatomic contamination. In this research, GO will be synthesized from natural graphite, through 2 methods, which are based on the method reported by Hummers in 1958 and which is the most widely used method today: in it, graphite is oxidized by treatment with potassium permanganate and silver nitrate in concentrated sulfuric acid [24]. The disadvantage of this procedure is that toxic gases such as nitrous and/or chlorine oxides are generated. In 2010, Marcano et al. published an improved method (called Enhanced Hummers) that has significant advantages, such as the absence of strongly exothermic reactions and the non-release of toxic gases,

in addition to improving reaction performance, which means a more substantial fraction of well-oxidized hydrophilic graphite material [25]. Thus, both methods will be included in a similar way for the synthesis of the following GO-based complexes.

Schniepp et al. 2006 [23] reported the characterization of SWGO in AFM by contact mode and tapping mode for the measurement of GO sheet topography (Figure 3-4). It shows that the presence of oxygenated groups alters the surface by increasing the height from a non-oxygenated flat zone of 0.38 nm to a minimum height of 1.1 nm, thus confirming the structure proposed in Figure 3-3. These images serve as a comparison for the materials to be developed in this research.

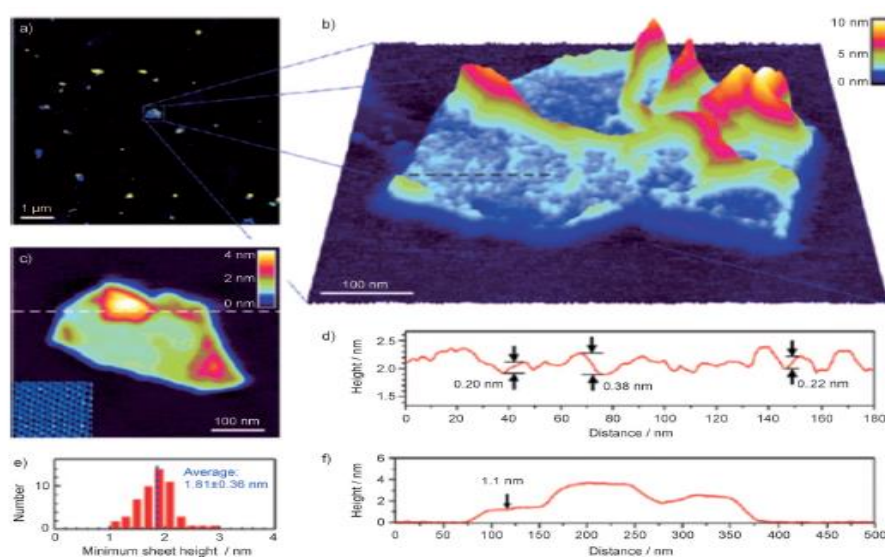


Figure 3-4 a) AFM image in Tapping mode in 8 micrometer area per side of thermally exfoliated graphite sheets. b) 3D representation of graphite sheet. c) illustration of a different sheet in contact mode to measure dimensions. d) cross -section of a flatter area of GO sheet in b), cross-section of sheet in c). e) histogram of average sheet heights in a) [23].

Figure 3-5 presented by Wang et al. 2008 [26] shows the TGA curve for graphite, reduced GO and GO, where it can be seen that graphite combustion starts at 650 °C when the sample is heated in air, while GO loses 20% of its mass at 200 °C and finally decomposes at 550 °C. This first loss is attributed to the removal of oxygenated groups that occurs at a lower temperature than combustion, showing later lower thermal stability, which is produced by the spaces damaged by the oxygenated groups when leaving the carbonate skeleton. An intermediate behavior is presented in the reduced GO that shows less number of oxygenated groups in the material, due to this it is preferred to call reduced GO (rGO) to the chemically modified graphene generated by the reduction of GO since the efficiency of the reduction is not assured, and the leaves of graphene are left with imperfections or radical groups even in the surface. Furthermore, it is mentioned that the degree of exfoliation of the rGO and GO also influences their thermal behavior, by facilitating exposure to oxygen and temperature achieving early combustion.

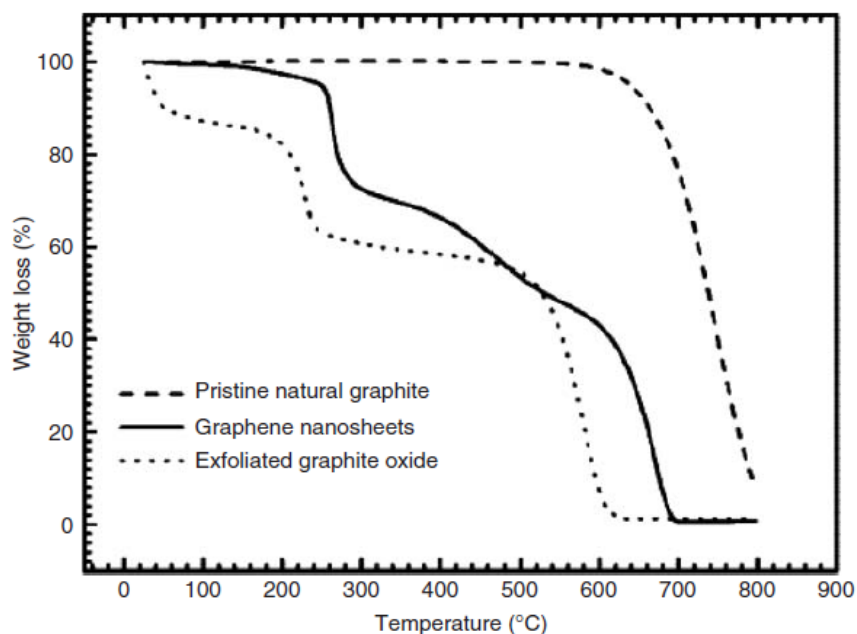


Figure 3-5 TGA curve of natural graphite, reduced GO (chemically modified graphite sheets) and exfoliated GO [27]

Typically, two methods are used to modify the surface of GO: covalent and non-covalent [27]. Examples of possible functionalization are mentioned in Table 4-1, where the chitosan method, which is developed later in this work, should be highlighted.

Table 3-1 Summary of covalent and non-covalent functionalities of graphene and GO for sustained drug delivery [4].

Method	Precursor or mechanism
<i>Covalent</i>	<i>Polyethylene glycol (PEG)</i>
	<i>Poly(acrylic) acid (PAA)</i>
	<i>Poly Lysine (PLL)</i>
	<i>Polyvinyl alcohol (PVA)</i>
	<i>Polyethylamine (PEI)</i>
	<i>Poly(N-isopropyl acrylamide) (PNIPAM)</i>
	<i>Polybasic Anhydride (PSA)</i>
	<i>Amphiphilic copolymers</i>
	<i>Folic Acid (FA)</i>
	<i>Sulfonic acid and amino groups</i>
	<i>Dextran</i>
	<i>Chitosan (CS)</i>
	<i>Fe₃O₄</i>
<i>Non-covalent</i>	<i>Interaction π-π stacking</i>
	<i>Van der Waals' forces</i>
	<i>Electrostatics</i>
	<i>Hydrogen Bridges</i>
	<i>Coordinated links</i>

3.1.1.1 Covalent functionalizations

Covalent functionalization can be achieved by various methods, including nucleophilic substitution, condensation, and addition. The most active sites for the reaction are the epoxy groups of GO, which allow binding to groups with an amino (-NH₂) group, as having the unshared electron pair enables the attack of amino groups. These are simple reactions, which occur at room temperature, in an aqueous medium and are easily scalable, being a promising method of modification for GO, using a wide range of molecules including all types of aliphatic and aromatic

amines. For example, Polyethylene glycol (PEG) is a biocompatible hydrophilic polymer used to functionalize several nanomaterials, as it improves their biocompatibility by reducing non-specific adsorption on biological molecules and cells, which allows enhancing pharmacokinetics in vivo to reach more quickly the point of action [4].

3.1.1.2 Non-covalent modification

Non-covalent modifications are also adsorptions of molecules on the surface of the GO, due to intermolecular forces that include van der Waals forces, electrostatic interactions, hydrogen bridges, coordinated bonds, and stacking π - π . Non-covalent functionalization can be achieved by polymer entrapment, adsorption of surfactants, or small molecules and by their interactions with biomolecules such as peptides and DNA. There are some disadvantages to using non-covalent modifications, such as less polymer adsorption on the surface of the GO and being affected by the external environment, making it less stable for use in a sustained component release. Also, functionalized GO with non-covalent methods may carry less aromatic drugs because the conjugated areas of the GO sheets are partially covered by polymers [4].

3.1.1.3 Covalent-non-covalent combination

The covalent functionalization associated with non-covalent adsorption is used as a method of manufacturing sustained release systems, which was born from the need to transport insoluble drugs and have a controlled release from the carrier. Covalent modification with polymers is the most used [27] and then these used for non-covalent loading of genes and drugs, forming complexes that are used for the detection of enzymatic activity, radio imaging, biosensing and sustained release of components, which is the purpose of this research.

The aim is to create a functionalization of GO with biopolymers Chitosan (CS) to then load them with a phytopharmaceutical and study their behavior against human cell models.

3.1.2 Graphene-based materials cytotoxicity

The surface chemistry of GO is varied, so are the interactions with cells, biomolecules, and tissues. Zhang et al. (2016) [28] mention that graphite materials can induce effects of evident cytotoxicity and that these depend on their concentration and surface chemistry. This is explained by the assumption that graphite materials can intervene in the interaction between membrane proteins and force separation into two functional proteins, damaging the phospholipid layer of the cell [29], which can interrupt cell metabolism and even lead to cell death. Zhang further mentions that graphite materials may have genetic risks affecting future generations (genotoxicity) and potential lung toxicity, which is related to the size that generates tissue damage by friction in small capillaries. Research shows that GO modified with carboxylic groups was able to weaken the hydrophobic interaction between GO and the cell membrane and suppress its toxicity.

In vitro and in vivo studies show that the cytotoxicity of human somatic cells is sensitive to the dose used. The direct interaction of GO slices and cells generates apoptosis in human and animal cells, which shows different results in different research groups presented in Table 4-2 . Hence the clinical application of GO alone seems to be remote until its biosafety is clarified. The results of several toxicological studies are shown below for comparison and evaluation.

3.1.2.1 *in vitro* tests

Cytotoxicity is defined as a modification of basic cellular functions that leads to damage that is visible. Several in vitro tests are available to predict the toxic effects of drugs and chemical compounds, using primary cultures and isolated organs as established cell lines as experimental models [30]. The results are significant, depending on the intended use. As the objective of this study is the creation of a drug, more considerable attention is paid to studies on red blood cells for the blood transport of the carrier and the phytodrug to be transported.

For the adequate comparison of the numerous following studies, three summary tables were created where the factors of interest are reported, which are: the applied dose, the in vitro or in vivo model used, the particle size and the z-potential. We separated between pristine GO, functionalized materials, and finally in vivo tests. Each research presents important factors but fails in another. For example, in the study by Hashemi et al. (2014) [31], the z-value is measured

in a physiological-like medium with a hefty dose and in human cells, all of which are desirable factors, the issue being its size, which reaches one micron, which is negative for its toxicity

In the group of Table 2-2, the work of Vallabani et al. (2011) [32] stands out, where all factors are desirable (human cells, normal dose, small size, and z-value far from 0) but still found apoptosis in their experimentation. These results represent the cytotoxicity of pristine GO.

Table 3-2 Collection table of studies on pristine graphic materials

Material	Cell model	Dose ($\mu\text{g mL}^{-1}$)	Average Size	z-Potential (mV)	Biological effect	Reference
GO	Human lung cells	10-100	72 nm	-11,7	Concentration- and time-dependent apoptosis.	[32]
GO	Spermatozoa	0.1-400	1 μm	-23.5 in HTF media	Cytotoxicity and dose-dependent genotoxicity	[31]
GO	HeLa human cervical cancer cells	10 -100	180 nm	-60,6 in water	Cellular viability is reduced from 85% to 70% with increasing dose	[33]
GO	HeLa	10	100 nm	-	100 % cell viability	[34]
GO	A549	7.8 -125	500 nm	-	80% cell viability at a dose of 125	[35]
GO	Red blood cells	10-75	200 nm		No observed hemolysis or risk of thrombosis	[36]

In Table 2-3, the functionalized materials, in general, show better biocompatibility than those of pristine materials, but they have factors that affect them, for example in the study by Liu et al. in 2008 where it occupied GO nanoparticles and then functionalized with PEG and showed zero toxicity, in cancer cells and without reporting its z-potential, which makes it difficult to compare with the rest of the studies.

Liao et al. 2011 [37] perform tests in different buffer media, which are present in the physiological medium called PBS (phosphate-buffered saline) and MEM (minimum essential medium), reporting the z-potentials of different GO and graphene in the various media, which makes them change their aggregation depending on the medium. It also shows that added graphene is more cytotoxic than reversibly added GO particles in human fibroblastic cells and that they associate strongly on the cell surface. This study is interesting when considering the present medium, and it is what we want to replicate to perform a simulation of molecular dynamics as close to reality as possible and that is why we propose to use a PBS medium in the simulation of the functionalized and charged material approaching the cell membrane.

Table 3-3 In vitro toxicity table of covalently functional graphitic materials.

Material	Cell model	Dose ($\mu\text{g mL}^{-1}$)	Average Size	z-Potential (mV)	Biological effect	Reference
GO-PEG	Saos 2 Osteoblastic	75	100 nm	-	Apoptosis, alteration of the cell cycle	[38]
NGO-PEG	MCF-7	100	<50 nm	-	No toxic	[39]
NGO-S-S-mPEG	HeLa	50-1000	<200 nm	-	>100% C.V. Much better sustained solubility than GO	[40]
GO-CS	RBC	100	2 μm	-	No hemolytic action	[37]
GO-CS	HepG2 and HeLa	1-100	500 μm - 800 μm -	-	>80 % c.v. and <40% c.v. loaded with CPT	[10]

3.1.2.2 *in vivo* tests

Although *in vitro* tests are a good approximation, the complexity of the toxic effects is more demonstrated in trials directly on animals. The results of these *in vitro* studies of both pristine and functionalized GO compounds are presented in Table 2-4 below.

Table 3-4 In vivo toxicity of pristine and functionalized graphitic materials.

Material	Animal Model	Dose	Biological effect (administration via)	Referencia
nGO	Lab Mouse	2mg mL ⁻¹	Pulmonary edema, pulmonary granuloma and extreme pathological effects (oral)	[41]
GO-PEG	Mice	20 mg kg ⁻¹	Gradual elimination. Significant accumulation in the tumor (i.v.)	[42]
GO-PEG	Mices	80 mg kg ⁻¹	100% survival (i.v.)	[43]

The biggest problem in being able to compare these results is that they do not report a particle size, let alone a z-potential, of what was given to the test animals. Even so, the most significant effect is seen at the lung level, since rigid particles of a specific size in the bloodstream damage the walls of the smaller alveoli in the lungs where oxygen exchange occurs. But in the case of Akhavan's study (2015) [41], he reports having a particle size less than 100 nm, which produces a positive biological effect.

The in vivo studies were not in the scope of this thesis but are reported with the intention of being able to compare their results with the in vitro ones and to demonstrate that there are differences and that even if conclusive results are obtained in this study, it would be under verification of more research, including in vivo tests.

3.1.3 Graphene oxide as a drug deliver device

Nanoparticles derived from graphene have been of more interest than graphene itself because their smaller size can be used as a drug carrier. As a consequence of their superior permeability, nanoparticles deliver better biocompatibility. The use of GO has been studied for the delivery of anti-cancer drugs, poorly soluble drugs, antibiotics, antibodies, peptides, DNA, RNA, and genes [4], [43], [44].

As a result of its aromatic planes and functional groups on the surface of the GO, it creates a high capacity to absorb aromatic compounds through hydrogen bridges and π - π stacking. GO nanoparticles can enter the bloodstream through M cells (enterocytes specialized in the uptake of luminal antigens) in the intestine due to their small size, which leads to an increase in the absorption of oral drugs. GO nanoparticles are absorbed by liver cells as the phagosomes of liver macrophages, being this a critical point in the use of graphene nano-oxide in the use of oral drug transport.

Targeting drug delivery systems have been shown by Zhang et al. [27], who covalently functionalized GO with folic acid for targeted delivery to MCF-7 cells, which are breast cancer cells that have receptors for folic acid. This composite was then loaded with doxorubicin (DOX) and camptothecin (CPT), two widely occupied anticancer drugs, which were loaded into GO-Folic Acid by hydrophobic interactions and π - π stacking and their results show significant cytotoxicity on MCF-7 cells with selectivity on them compared to only DOX or CPT loaded GO. But the exclusive use of GO as a carrier is reduced and is often combined with other components to improve the load capacities and controlled release [5].



3.2 Chitosan

Chitosan is a natural polysaccharide obtained from the partial or total deacetylation of chitin (Figure 3-6), which is the most abundant natural polysaccharide after cellulose. Chitin is an integral part of the cell wall of fungi, the exoskeleton of crustaceans and insects. Chitosan is the N-acetyl derivative of chitin, a linear, semi-crystalline polysaccharide composed of glucosamine and N-acetyl glucosamine bound by β -(1 \rightarrow 4) glycoside. When the fraction of glucosamine units is greater than 50 %, the polymer is commonly called chitosan, and the number of glucosamine units determines the degree of deacetylation (DD). Besides, when the DD exceeds 50% (depending on the origin of the polymer and the process conditions), it becomes soluble in acidic media [12].

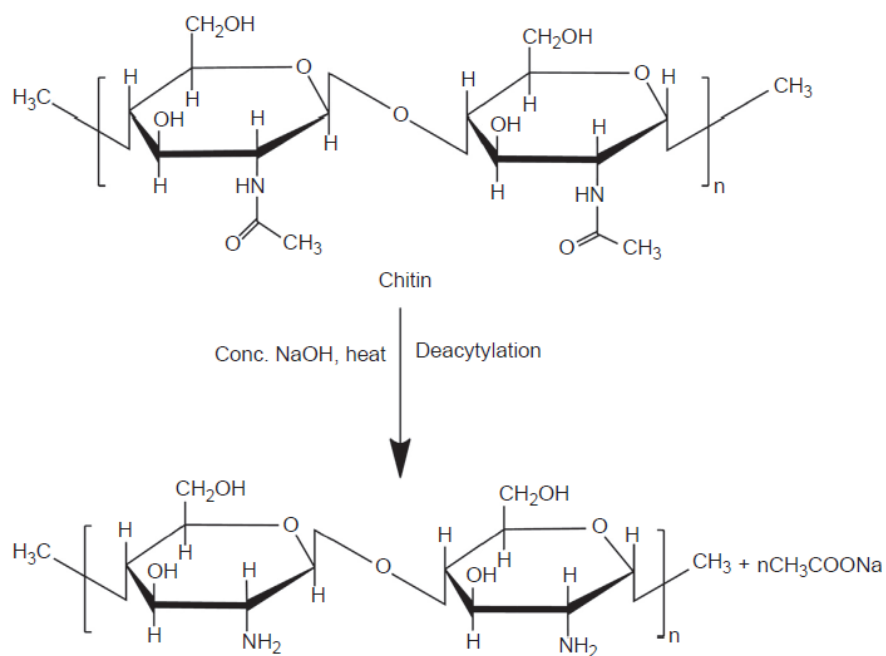


Figure 3-6 Deacetylation of chitin to chitosan

The chitosan in its crystalline form is a white or pinkish solid depending on the process conditions and the level of residual pigments, it is insoluble in aqueous solutions that have a pH above 7, but in diluted acids (pH<6), the free amino groups of the glucosamine units help the solubility of the polymer molecule. In acidic medium, the polysaccharide is converted into a polyelectrolyte, which means that it is a polymer containing both positive and negative ionizable groups. Solubilization occurs by protonation of the amine group (-NH₂) at the C-2 position of the

D-glucosamine unit. Depending on the method of obtention and preparation, its molecular weight can vary from 300 to 1000 kDa with DD 30% to 95% (taking into account the convention that only polymers with DD>50% are called chitosan). The functional properties of CS such as film formation, antimicrobial activity, and use as a thickening agent are related to its molecular weight and DD.

Commercially, CS has a DD range of 70-95%, which is critical to know for possible chemical modification and medical use. Studies have shown that its antimicrobial effect is related to both molecular weight and DD. Besides, the antimicrobial activity of chitosan against Gram-negative bacteria increases with decreasing molecular weight and pH.

Chitosan has very low toxicity, with an LD₅₀ in rats of 16g·kg⁻¹ body mass, which is very close to the value of ordinary sugar or table salt. Also, it has been shown to be safe in rats by up to 10% in the diet [46]. Its physiological effects include lowering cholesterol, lowering blood pressure, inhibiting fat absorption, and increasing intestinal microflora. It has been included in foods because of its safety in humans and animals [45]. The advantages for the biomedical application of chitosan, are its biocompatibility and biodegradability, the latter generates harmless products (amino sugars) that are absorbed by the human body, not making inflammatory reactions or rejections.

Besides, chitosan is easily chemically modified through one of its three reactive functional groups: the amino group and both primary and secondary hydroxyl groups at C(2), C(3), and C(6) respectively [45]. The chemical nature of chitosan provides the possibility of covalent and ionic modifications, which allows it to adjust to the biological and mechanical properties of chitosan-based medical devices. Unlike plant fibers, chitosan has positive ionic charges, allowing it to bond chemically with fats, lipids, proteins, cholesterol, macromolecules, and metal ions [12].

Because this biopolymer has a unique polycationic nature, biodegradability, biocompatibility, zero toxicity and its ability to be reabsorbed, chitosan has a full application in medicine for applications such as gene therapy (drug or gene delivery), wound dressings, tissue engineering, hypocholesterolemic agent, biomedical bone regeneration and anti-microbial agent.

It is because of these properties, which are ideal for biomedical use that we use CS in this work for its combination with GO improving the biocompatibility of GO alone.

3.2.1 CS applications

CS is used in the industrial area in the manufacture of cosmetics, paper, pulp, water treatment, and as a food additive. But for the applications of interest in this work, chitosan has important properties with implications for its use in drug transport and hemostasis, which are its mucoadhesiveness, coagulation capacity, immunostimulant character and its ability to pass through narrow epithelial junctions.

These abilities have been exploited by drug transport in complex epithelia such as the nasal, intestinal, ocular, oral and pulmonary epithelia. Also, with the positive surface charge, CS can interact with negatively charged nucleic acid molecules forming polyelectrolyte complexes. These complexes have been shown to protect nucleic acids from degradation by nucleases. The positive charge also allows interaction with negatively charged membranes leading to increased cell interaction and absorption efficiency across the membrane.

CS is widely used as a nanoparticle in drug delivery, which is generally manufactured by the ion gelation method. Also, these chitosan-based non-viral nanocarriers have been engaged in siRNA transport, to carry out efficient blocking of several therapeutically relevant genes, such as TGF β 1, Bcl-2, etc. CS-based matrixes and gels are also beneficial, showing advantages over materials commonly used in wound healing. Although chitosan is known to have a broad antimicrobial spectrum, the treatment of wounds that are easily infected remains a severe problem to chitosan-based dressings.

3.2.2 CS on drug delivery

The drug delivery in micro and nanoparticle systems can be achieved through two methods; one is during the preparation of the particles (called incorporation) or after the formation of the particles (called incubation). In these systems, the drug is either adsorbed to the surface or absorbed into the matrix, and various loading mechanisms depending on both the preparation method and the physicochemical properties of the drug. The maximum drug loading on these transporters can be achieved by incorporating the drug during the formation of the particles, but this can be altered by the parameters of the preparation process, such as the presence of additives or pH conditions, etc.

Soluble and insoluble drugs can be loaded onto chitosan-based particles. Soluble drugs are mixed in solution with chitosan forming a homogeneous mixture, and then the particles are produced in any method. Meanwhile, insoluble drugs and those that precipitate in acidic media can be charged after particle formation through impregnation of the particles in saturated drug solutions. Also, insoluble active ingredients can be loaded by using multiple emulsion techniques, or by using some surfactant to disperse the drug in a chitosan solution and obtain a suspension.

The release of drugs from CS-based systems depends on the degree of cross-linking, morphology, size, and density of the system, and physicochemical properties of the drug. In vitro release also depends on the pH, polarity, and presence of enzymes in the medium.



3.3 Graphene Oxide and Chitosan Combinations

As mentioned above, CS and GO have applications in drug transport, the results of which tend to be auspicious. The result of combining these materials for drug transport using the benefits of both substances may be promising. This combination generates carriers that are stable, biocompatible, and biodegradable, and that have new and improved properties that are important for drug release [30].

The addition of GO to chitosan is reported to increase the ability of chitosan to carry drugs. For example, the introduction of GO improves the mechanical properties of CS, which is one of the problems in the use of CS-based carriers in drug delivery. In the study by Pan et al. (2011) [31] GO is added in a CS matrix for mechanical reinforcement of CS. With the addition of 1% wt of GO, the tensile strength reaches 93%, and the stress modulus reaches 51% (much higher results than the matrix without GO additive). In the study by Justin et al. (2007) [32], it is shown that the strain and tensile stress curves of CS nanocomposites containing between 0.25 and 5% GO Samples containing GO show failure between 17.7% and 35.1% of stress, which is better than pure CS (14.5%), which is explained by an increase in CS ductility due to the orientation and delamination of graphite sheets under stress. In addition, the rate of CS biodegradation is reduced in the presence of GO [30].

The addition of CS to GO drug carriers benefits the transport efficiency of GO leaves makes them more stable by increasing and changing their surface load generating a higher modulus load at 30 mV which makes them more stable in suspension [30]. CS increases biocompatibility and has been shown to create an option to design efficient drug transporters with desirable properties for that purpose [23], [30], [31], [33], [34].

Considering that the materials that will be dealt with later in work are nanocomposites and aerogels, it is shown below some materials already reported for applications similar to our objective.

For example, in the work of Justin et al. (2014) [47], chitosan nanocomposites containing varying GO contents and drug loading ratios were investigated. The nanocomposite with 2 wt % GO provided the optimal combination of mechanical properties and drug-loading capacity. It offered a faster and a more substantial release of the drug than chitosan as well as a slower

biodegradation rate, owing to the abundant oxygenated functional groups, hydrophilicity and large specific surface area of GO sheets. The drug delivery profiles of the nanocomposite were dependent on the drug loading ratio, with 0.84:1 is the best ratio of drug to GO for a quick and high release of the loaded drug. The nanocomposite also demonstrated pH sensitivity of drug release, releasing 48% less drug in an acidic condition than in a neutral environment.

Also, there are reports on aerogels for the absorption of physiological fluids as in the work of Song et al. (2019) [11] Chitin and GO-based aerogel beads were prepared in a NaOH/urea aqueous solution, followed dried by supercritical carbon dioxide. The results indicated that GO was successfully bound to the chitin matrix with enhanced surface area, thermal stability, and mechanical strength. Batch adsorption results revealed that the Chitin/GO composite aerogel beads showed excellent bilirubin adsorption capacity ($484.1 \pm 16.9 \text{ mg g}^{-1}$) and short adsorption equilibrium time (0.5 h) under optimized condition. Furthermore, the Chitin/GO aerogel beads exhibited a lowered hemolysis property.

Furthermore, some absorption kinetics is studied in the work of Yu et al. (2013) [48] GO-CS composite was lyophilized to develop GO-CS aerogel for Cu^{2+} removal. The separation of adsorbents after adsorption was easily achieved by filtration or low-speed centrifugation. GO-CS was an excellent adsorbent of Cu^{2+} with a large adsorption capacity of $2.54 \times 10^1 \text{ mg g}^{-1}$ according to the Langmuir model. The adsorption kinetics was well described by the pseudo-second-order model with a k_2 of $4.14 \times 10^{-3} \text{ min}^{-1}$. The intraparticle diffusion model was adopted to reveal the diffusion mechanism. Higher pH, lower ionic strength, and higher temperature benefited the adsorption. The adsorption identity was physio sorption and driven by the increase of randomness.

3.4 Proanthocyanidins

Phenolic compounds are classified into subcategories depending on their structural skeleton, varying in nature from simple molecules such as phenolic acids to compounds of a polymeric nature such as proanthocyanidins. Flavonoids are one of the best-known families of polyphenolic compounds. So much, so that polyphenolic compounds are commonly divided into flavonoids and non-flavonoids.

The chemical structure of the flavonoids consists of a skeleton of diphenyl propane ($C_6-C_3-C_6$) formed by two aromatic rings (A and B) joined by three carbon atoms that form an oxygenated heterocycle (C) (see Figure 3-7). The flavonoids are divided into different families depending on the oxidation status of the heterocycle. Thus we distinguish between flavones, isoflavones, flavanones, flavonols, flavanols and anthocyanidins.

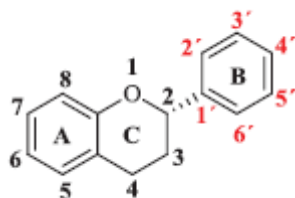
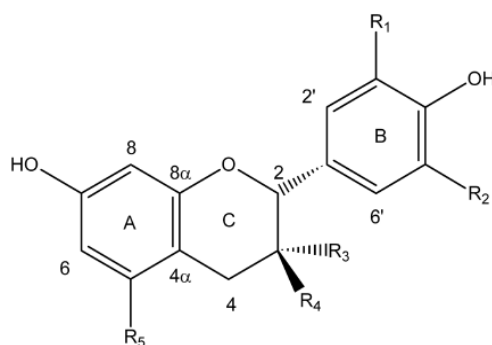


Figure 3-7 Chemical structure of flavonoids

Proanthocyanidins are structurally differentiated according to the hydroxyl group number, their position in the aromatic rings and their spatial configuration in the constituent flavanol units (see Figure 3-8). Flavan-3-ols have two chiral carbon atoms, i.e. there are four diastereoisomers for each of them. Enantiomers with a cis configuration have the prefix "epi" while units with a trans configuration have no prefix. Sometimes the prefix "epi" is included in parentheses to indicate either one or the other compound.



2R Flavan-3-ol Monomers	R₁	R₂	R₃	R₄	R₅
(+)-afzelechin	H	H	H	OH	OH
(-)-epiafzelechin	H	H	OH	H	OH
(+)-catechin	H	OH	H	OH	OH
(-)-epicatechin	H	OH	OH	H	OH
(+)-gallocatechin	OH	OH	H	OH	OH
(-)-epigallocatechin	OH	OH	OH	H	OH
(+)-fisetinidol	H	OH	H	OH	H
(-)-epifisetinidol	H	OH	OH	H	H
(+)-robinetinidol	OH	OH	H	OH	H

Figure 3-8 Flavan-3-ol monomer examples. (From: Aron and Kennedy (2008))

Flavonoids are found in nature mainly as (epi)catechin or (epi)catechin gallates, either in monomeric form or as polymeric compounds. These flavanol polymers are called proanthocyanidins or condensed tannins and are found in foods such as tea, cocoa, and grapes. In that sense, proanthocyanidins are mainly responsible for the astringent properties of red wine.

Proanthocyanidins have been described as antimicrobial, antioxidant, anticarcinogenic and anti-inflammatory compounds, in addition to being beneficial for the prevention of diseases related to metabolic syndromes. There are a variety of classes of proanthocyanidins depending on the monomeric unit of which they are composed (Figure 3-9).

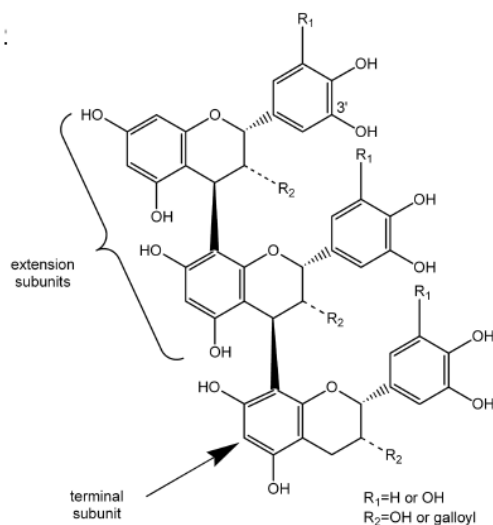


Figure 3-9 Procyanidin example (From: Aron and Kennedy (2008))

3.4.1 Characterization of PAs

To evaluate the composition content of these polymeric compounds in various foods and plant sources implies an added difficulty due to the complexity of their extraction.

UV-Vis spectroscopy is one of the most commonly used methods for the detection and quantification of different types of polyphenols. Due to the phenolic rings of these compounds, polyphenols are excellent chromophores, which facilitates their detection with UV-vis spectroscopy. The different families absorb at a characteristic wavelength, which depends on the number, position and type of substituents of the compound. For example, flavonols present their maximum absorbance at 280 nm, flavanols at 360nm and anthocyanidins at 550nm. The use of diode array detectors (DAD) allows the analysis of a sample at different wavelengths and therefore, the determination of different families of phenolic compounds.

Several colorimetric methods are available for the determination of polyphenolic compounds. The Folin-Ciocalteu test is used as a measure of the total phenolic compound content in natural products and is the primary test used in this study. The mechanism of this test is governed by a redox reaction based on the oxidation of hydroxyl groups, so it is frequently used in studies of antioxidant properties of foods for the measurement of total antioxidant activity. The oxidation of the phenols present in the sample by a molybdenum and tungsten reagent in a basic medium

causes the appearance of a blue coloration that has a maximum absorption at 765 nm and is quantified by spectrophotometry using a standard gallic acid line as reference.

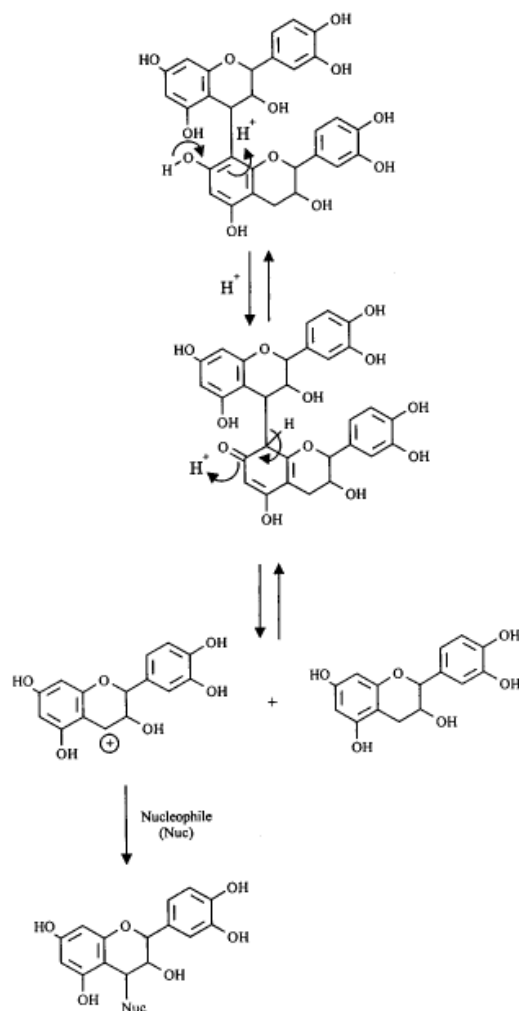


Figure 3-10 Hypothetical reaction mechanism explaining acid-catalyzed cleavage of proanthocyanidins (from: Kenned and Jones (2001))

Chromatography methods are used for the analysis of proanthocyanidins, which can use proanthocyanidins after acid catalysis. This method allows us to obtain their average molecular weight (aMW) while giving information on the distribution, together with the composition of their subunits and the location of the interflavanic link. It is possible to determine the composition of the subunits of the proanthocyanidins by the relative ease with which their bonds are separated, and thus, under acidic conditions, releasing terminal subunits as Flava-3-ols monomers and extension subunits as electrophilic Flava-3-ols intermediates. The electrophilic intermediates are then captured by the nucleophilic agent to generate analyzable adducts.

3.4.2 Bioactivities of PAs

The consumption of grape-derived dietary flavonoids in the form of grape extracts and grape seed powders has been shown to effectively suppress oxidative stress and prevent oxidative damage in vivo, due to their high antioxidant potential [17].

The PAs in these grape extracts exhibit inhibitory properties of the angiotensin I converting enzyme (an enzyme that catalyzes the degradation of angiotensin I to angiotensin II, a potent vasoconstrictor) [49], which makes them a possible option for anti-hypertensive treatment. A rich source of PAs is found in the skin and seeds of País grape (*Vitis vinifera* L.), which is an underutilized resource in areas of the country, mainly in the regions of Maule, Ñuble and Bío-Bío, Chile.

The antimicrobial activities of grapes, wine, and grape by-products have been widely discussed demonstrating that grape seed extract from *V. vinifera* variety Bangalore blue grapes exhibits potent antibacterial activity against Gram-positive bacteria compared to the response of Gram-negative bacteria [50]. Grape polyphenols have been shown to reduce chronic inflammation, either by modulating inflammatory pathways or by reducing levels of reactive oxygen species (ROS). Freeze-dried extract of "Jacquez" grape wine (*Vitis aestivalis-cinerea* × *Vitis vinifera*), containing mainly flavonoids, anthocyanins, proanthocyanidins and hydroxycinnamic acid derivatives, showed increased anti-inflammatory activity compared to Indomethacin, a commercial non-steroidal anti-inflammatory drug (NSAID) [51].

Furthermore, Lodhi et al. (2013) [52] evaluated the healing potential of flavonoid fractions of *Martynia annua* Linn plant leaves. And luteolin in diabetic rats; their results indicated that the flavonoid and luteolin fraction (0.5% wt, one of the most common flavonoids, 2-(3,4-Dihydroxyphenyl)-5,7-dihydroxy-4-chromenone) might benefit wound healing under diabetic conditions, possibly due to the free radical scavenging activity of the plant. Nayak et al. (2010) [53] evaluated the healing activity of grape skin powder (*L. Vitaceae*) using a model of excision wounds in rats; their results showed an increase in wound contraction rate, hydroxyproline content, and decreased epithelialization time in treated animals, making the use of grape skin powder for wound healing management possible.

The large amount of hydroxyl groups that PAs compounds possess makes them highly reactive with other molecules; in particular, they have a high affinity for proteins. This reactivity

is determined by the polymerization fraction of the compound, types of interglavanic bonds and hydroxylation pattern. It is necessary to know these differences to understand what biological effects they may have and how they may affect metabolism [54].



3.5 Coagulation Process on Artificial Surfaces

The external surfaces from the body promote blood clotting through the activation of a series of interconnected processes, which include the adsorption of proteins, platelets and leukocytes, thrombin generation and complimentary activation (see Figure 3-11). The first processes will be described below, emphasizing the effect of the surface and its characteristics on the initiation of the coagulation process.

3.5.1 Protein Adsorption

While knowledge of protein-surface interactions is substantial, in the context of blood, in particular, it remains fragmented and lacking in cohesion [55].

The first process is the rapid adsorption of proteins from the plasma, which initiates the formation of thrombus because the adsorbed proteins modulate the subsequent reactions. The dynamics of protein adsorption are related to the physical and chemical properties of the surface and the proteins. The adsorbed proteins can form a surface with a thickness of 2 to 10 nm and the concentration of proteins on the surface can be up to 1000 times higher than those present in the plasma [56]. The adsorption on the surface is regularly reversible, and the composition of the adsorbed proteins changes over time. This phenomenon was first described by Leo Vroman and is known as the Vroman effect [57]. This effect is more present on hydrophilic negative surfaces and seems to be independent of the flow [58].

It is assumed that the proteins would be the first to reach the surfaces before the cells due to the difference in size and concentration. It has been reported that the protein layer is formed in order of a few seconds [59]. There is evidence that the composition of this layer varies over time [60]. Perhaps the most extensive information on the dependence of protein coat composition over time comes from Vroman's studies. Initial work shows that fibrin is adsorbed in a short time, but then it is displaced by other plasma constituents. Vroman proposed that the proteins of the intrinsic coagulation pathway, particularly high molecular weight kininogen, are primarily responsible for the displacement of fibrinogen [61].

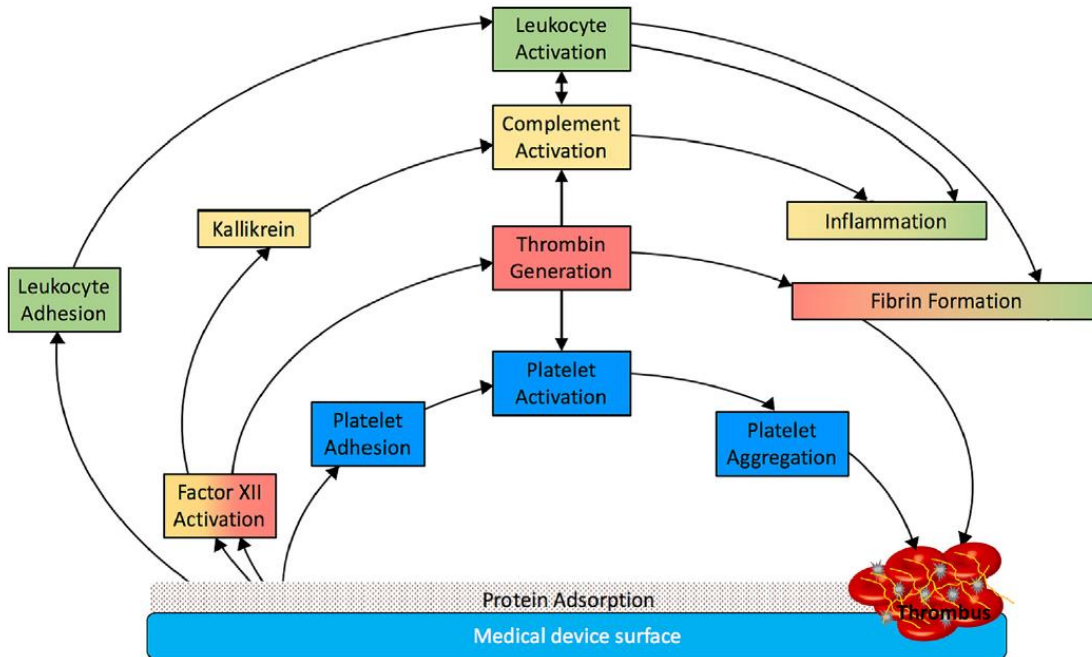


Figure 3-11 Protein adsorption on the surface of medical devices induces platelet adhesion, activation and aggregation. Factor XII adsorbed to the surface undergoes autoactivation, and the resulting factor XIIa converts prekallikrein to kallikrein and initiates coagulation and thrombin generation. In addition to inducing fibrin deposition on the surface, thrombin promotes platelet activation. Platelet aggregates deposited on the surface are stabilized by fibrin strands to form a platelet-fibrin thrombus. Kallikrein, thrombin and other coagulation enzymes activate complement, inducing a local inflammatory response. Leukocytes also adhere to the surface where they become activated and can contribute to both inflammation and thrombosis. [30]

Other proteins are also attached, such as von Willebrand factor and fibronectin, and together with fibrinogen, they mediate platelet adhesion. The adsorbed fibrinogen is frequently replaced by other proteins belonging to the coagulation chain, including factor (F) XII, high molecular weight kininogen, Fletcher's factor and FXI [62]. Activation of the adsorbed FXII not only triggers the generation of thrombin through the intrinsic coagulation pathway but also activates the complementary immune system. With the activation of both the coagulation system and the system, thrombin generation is amplified [55].

While it is clear that the composition of the protein layer is dependent on time, the nature of that dependence on surface properties such as loading and hydrophobicity is not fully understood. There is a great deal of evidence of protein absorption in systems with a single type of protein that adsorption increases with surface hydrophobicity, which was obtained using surfaces with hydrophobic gradients [63]. This trend has not been consistent in other studies [55].

3.5.2 Cell adhesion

The adsorbed proteins mediate the adsorption of platelets, leukocytes and red cells to artificial surfaces. Fibrinogen is the main protein responsible for platelet adhesion. The interaction between platelet and fibrinogen is mediated by $\alpha_{IIb}\beta_3$ (the most abundant integrin on the surface of platelets). This interaction is of high affinity, and low concentrations of adsorbed fibrin (from 7 ng cm^{-2}) are capable of generating platelet adhesion. Although von Willebrand factor and fibronectin also bind platelets, they are less essential mediators of platelet adhesion compared to fibrinogen.

Platelet adhesion to artificial surfaces is activated and begins to release thromboxane A_2 , adenosine diphosphate (ADP) and other agonists. By activating nearby platelets, these substances amplify platelet adhesion leading to thrombus formation.

In addition to tissue factor-mediated coagulation, components of the contact system are adsorbed into artificial surfaces, thus facilitating the intrinsic pathway of coagulation. The adsorbed FXII goes through a self-activation to become the FXIIa enzyme, which then activates the Fletcher factor and FXI. As the high molecular weight kininogen is adsorbed into artificial surfaces, further activation of FXII occurs, and contact system pathways occur. Activation of FXI initiates a series of protein reactions that culminate in thrombin generation. Thrombin not only converts fibrinogen into fibrin monomer but also serves as a potent platelet agonist, generating a local accumulation of platelets. Fibrin monomers polymerize and cross-linked by FXIIIa. Crosslinked fibrin traps and stabilizes platelet accumulation creating a platelet thrombus and fibrin [64].

These processes are expected to occur once the blood adsorption over the aerogel matrix of GO and CS reported in chapter 4 has been completed. These coagulation processes are the reason that would allow the biomaterial to have its hemostatic capacity.

3.6 References

- [1] R. Surudžić *et al.*, “The effect of graphene loading on mechanical, thermal and biological properties of poly (vinyl alcohol)/graphene nanocomposites,” *Journal of industrial and engineering chemistry*, vol. 34, pp. 250–257, 2016, doi: 10/f79dgp.
- [2] M. Ramezanpour, S. S. W. Leung, K. H. Delgado-Magnero, B. Y. M. Bashe, J. Thewalt, and D. P. Tieleman, “Computational and experimental approaches for investigating nanoparticle-based drug delivery systems,” *Biochimica et Biophysica Acta (BBA)-Biomembranes*, vol. 1858, no. 7, pp. 1688–1709, 2016, doi: 10/gd4t9d.
- [3] W. H. De Jong and P. J. A. Borm, “Drug delivery and nanoparticles: Applications and hazards,” *International journal of nanomedicine*, vol. 3, no. 2, pp. 133–149, 2008.
- [4] J. Liu, L. Cui, and D. Losic, “Graphene and graphene oxide as new nanocarriers for drug delivery applications,” *Acta biomaterialia*, vol. 9, no. 12, pp. 9243–9257, 2013, doi: 10/gd4t9p.
- [5] Q. Zhang *et al.*, “Advanced review of graphene-based nanomaterials in drug delivery systems: Synthesis, modification, toxicity and application,” *Materials Science & Engineering C-Materials for Biological Applications*, vol. 77, pp. 1363–1375, Aug. 2017, doi: 10.1016/j.msec.2017.03.196.
- [6] C. emsp14N emsp14R Rao, A. emsp14K Sood, K. emsp14S Subrahmanyam, and A. Govindaraj, “Graphene: the new two-dimensional nanomaterial,” *Angewandte Chemie International Edition*, vol. 48, no. 42, pp. 7752–7777, 2009, doi: 10.1002/anie.200901678.
- [7] S. Y. Wu, S. S. A. An, and J. Hulme, “Current applications of graphene oxide in nanomedicine,” *International journal of nanomedicine*, vol. 10, pp. 9–24, 2015, doi: 10.2147/ijn.s88285.
- [8] S. Gooneh-Farahani, M. R. Naimi-Jamal, and S. M. Naghib, “Stimuli-responsive graphene-incorporated multifunctional chitosan for drug delivery applications: a review,” *Expert opinion on drug delivery*, vol. 16, no. 1, pp. 79–99, 2019.
- [9] T. S. Yan, F. Cheng, X. J. Wei, Y. D. Huang, and J. M. He, “Biodegradable collagen sponge reinforced with chitosan/calcium pyrophosphate nanoflowers for rapid hemostasis,” *Carbohydrate Polymers*, vol. 170, pp. 271–280, Aug. 2017, doi: 10.1016/j.carbpol.2017.04.080.
- [10] H. Bao *et al.*, “Chitosan-functionalized graphene oxide as a nanocarrier for drug and gene delivery,” *Small*, vol. 7, no. 11, pp. 1569–1578, 2011, doi: 10/c7k2nc.

- [11] X. Song *et al.*, “Construction of blood compatible chitin/graphene oxide composite aerogel beads for the adsorption of bilirubin,” *Carbohydrate polymers*, vol. 207, pp. 704–712, 2019.
- [12] A. Baranwal *et al.*, “Chitosan: An undisputed bio-fabrication material for tissue engineering and bio-sensing applications,” *International journal of biological macromolecules*, 2018, doi: 10/gdchxn.
- [13] Y. Pan, T. Wu, H. Bao, and L. Li, “Green fabrication of chitosan films reinforced with parallel aligned graphene oxide,” *Carbohydrate Polymers*, vol. 83, no. 4, pp. 1908–1915, Feb. 2011, doi: 10/bmn3fm.
- [14] X. Zhao *et al.*, “Design and development of graphene oxide nanoparticle/chitosan hybrids showing pH-sensitive surface charge-reversible ability for efficient intracellular doxorubicin delivery,” *ACS applied materials & interfaces*, vol. 10, no. 7, pp. 6608–6617, 2018, doi: 10/gd4t9k.
- [15] S. S. Saravanabhavan *et al.*, “Graphene oxide functionalized with chitosan based nanoparticles as a carrier of siRNA in regulating Bcl-2 expression on Saos-2 & MG-63 cancer cells and its inflammatory response on bone marrow derived cells from mice,” *Materials Science & Engineering C-Materials for Biological Applications*, vol. 99, pp. 1459–1468, Jun. 2019, doi: 10.1016/j.msec.2019.02.047.
- [16] F. Zhang *et al.*, “Chitosan and dextran stabilized GO-iron oxide nanosheets with high dispersibility for chemotherapy and photothermal ablation,” *Ceramics International*, vol. 45, no. 5, pp. 5996–6003, Apr. 2019, doi: 10.1016/j.ceramint.2018.12.070.
- [17] V. Georgiev, A. Ananga, and V. Tsoleva, “Recent advances and uses of grape flavonoids as nutraceuticals,” *Nutrients*, vol. 6, no. 1, pp. 391–415, 2014, doi: 10/f5qzgb.
- [18] N. Vale, A. Ferreira, J. Matos, P. Fresco, and M. J. Gouveia, “Amino Acids in the Development of Prodrugs,” *Molecules (Basel, Switzerland)*, vol. 23, no. 9, p. 2318, 2018, doi: 10.3390/molecules23092318.
- [19] S. S. Bansal, M. Goel, F. Aqil, M. V. Vadhanam, and R. C. Gupta, “Advanced drug delivery systems of curcumin for cancer chemoprevention,” *Cancer prevention research*, vol. 4, no. 8, pp. 1158–1171, 2011.
- [20] T. Gunasekaran, T. Haile, T. Nigusse, and M. D. Dhanaraju, “Nanotechnology: an effective tool for enhancing bioavailability and bioactivity of phytomedicine,” *Asian Pacific journal of tropical biomedicine*, vol. 4, no. Suppl 1, pp. S1-7, May 2014, doi: 10.12980/apjtb.4.2014c980.

- [21] P. M. Aron and J. A. Kennedy, "Flavan-3-ols: Nature, occurrence and biological activity," *Molecular Nutrition & Food Research*, vol. 52, no. 1, pp. 79–104, 2008, doi: 10.1002/mnfr.200700137.
- [22] R. Gu *et al.*, "The performance of a fly-larva shell-derived chitosan sponge as an absorbable surgical hemostatic agent," *Biomaterials*, vol. 31, no. 6, pp. 1270–7, Feb. 2010, doi: 10.1016/j.biomaterials.2009.10.023.
- [23] H. C. Schniepp *et al.*, "Functionalized single graphene sheets derived from splitting graphite oxide," *The Journal of Physical Chemistry B*, vol. 110, no. 17, pp. 8535–8539, 2006.
- [24] W. S. Hummers and R. E. Offeman, "Preparation of Graphitic Oxide," *Journal of the American Chemical Society*, vol. 80, no. 6, pp. 1339–1339, Mar. 1958, doi: 10.1021/ja01539a017.
- [25] D. C. Marcano *et al.*, "Improved synthesis of graphene oxide," *ACS nano*, vol. 4, no. 8, pp. 4806–4814, 2010, doi: 10/bp734k.
- [26] G. Wang *et al.*, "Facile Synthesis and Characterization of Graphene Nanosheets," *The Journal of Physical Chemistry C*, vol. 112, no. 22, pp. 8192–8195, Jun. 2008, doi: 10.1021/jp710931h.
- [27] V. Georgakilas, "Functionalization of Graphene by other Carbon Nanostructures," in *Functionalization of Graphene*, Wiley-VCH Verlag GmbH & Co. KGaA, 2014, pp. 255–282.
- [28] B. Zhang, Y. Wang, and G. Zhai, "Biomedical applications of the graphene-based materials," *Materials Science and Engineering: C*, vol. 61, pp. 953–964, Apr. 2016, doi: <https://doi.org/10.1016/j.msec.2015.12.073>.
- [29] M. Dallavalle, M. Calvaresi, A. Bottoni, M. Melle-Franco, and F. Zerbetto, "Graphene can wreak havoc with cell membranes," *ACS applied materials & interfaces*, vol. 7, no. 7, pp. 4406–4414, 2015.
- [30] D. F. A. Arrebola, L. Fernández, and D. Sánchez, "Principales ensayos para determinar la citotoxicidad de una sustancia, algunas consideraciones y su utilidad," *Revista toxicológica en línea*, pp. 40–53, 2003.
- [31] E. Hashemi, O. Akhavan, M. Shamsara, R. Rahighi, A. Esfandiar, and A. R. Tayefeh, "Cytotoxic and genotoxicities of graphene oxide and reduced graphene oxide sheets on spermatozoa," *Rsc Advances*, vol. 4, no. 52, pp. 27213–27223, 2014, doi: 10/gd4t9n.

- [32] N. V. Vallabani *et al.*, “Toxicity of graphene in normal human lung cells (BEAS-2B),” *Journal of biomedical nanotechnology*, vol. 7, no. 1, pp. 106–107, 2011, doi: 10/ckt2xq.
- [33] J. Hong, K. Char, and B.-S. Kim, “Hollow capsules of reduced graphene oxide nanosheets assembled on a sacrificial colloidal particle,” *The Journal of Physical Chemistry Letters*, vol. 1, no. 24, pp. 3442–3445, 2010.
- [34] K. Yang *et al.*, “Multimodal imaging guided photothermal therapy using functionalized graphene nanosheets anchored with magnetic nanoparticles,” *Advanced materials*, vol. 24, no. 14, pp. 1868–1872, 2012.
- [35] H. Ali-Boucetta, D. Bitounis, R. Raveendran-Nair, A. Servant, J. Van den Bossche, and K. Kostarelos, “Purified graphene oxide dispersions lack in vitro cytotoxicity and in vivo pathogenicity,” *Advanced healthcare materials*, vol. 2, no. 3, pp. 433–441, 2013.
- [36] A. Sasidharan *et al.*, “Hemocompatibility and macrophage response of pristine and functionalized graphene,” *Small*, vol. 8, no. 8, pp. 1251–1263, 2012.
- [37] K.-H. Liao, Y.-S. Lin, C. W. Macosko, and C. L. Haynes, “Cytotoxicity of graphene oxide and graphene in human erythrocytes and skin fibroblasts,” *ACS applied materials & interfaces*, vol. 3, no. 7, pp. 2607–2615, 2011.
- [38] M.-C. Matesanz *et al.*, “The effects of graphene oxide nanosheets localized on F-actin filaments on cell-cycle alterations,” *Biomaterials*, vol. 34, no. 5, pp. 1562–1569, 2013.
- [39] Z. Liu, J. T. Robinson, X. Sun, and H. Dai, “PEGylated Nanographene Oxide for Delivery of Water-Insoluble Cancer Drugs,” *Journal of the American Chemical Society*, vol. 130, no. 33, pp. 10876–10877, Aug. 2008, doi: 10.1021/ja803688x.
- [40] Y. Wen, H. Ding, and Y. Shan, “Preparation and visible light photocatalytic activity of Ag/TiO₂/graphene nanocomposite,” *Nanoscale*, vol. 3, no. 10, pp. 4411–4417, 2011.
- [41] O. Akhavan, “Bacteriorhodopsin as a superior substitute for hydrazine in chemical reduction of single-layer graphene oxide sheets,” *Carbon*, vol. 81, pp. 158–166, 2015.
- [42] X. Yang, Y. Tu, L. Li, S. Shang, and X. Tao, “Well-Dispersed Chitosan/Graphene Oxide Nanocomposites,” Jun. 07, 2010. <https://pubs.acs.org/doi/abs/10.1021/am100222m> (accessed Sep. 25, 2018).
- [43] X. Sun *et al.*, “Nano-Graphene Oxide for Cellular Imaging and Drug Delivery,” *Nano research*, vol. 1, no. 3, pp. 203–212, 2008, doi: 10.1007/s12274-008-8021-8.

- [44] S. Khoee, R. Bafkary, and F. Fayyazi, "DOX delivery based on chitosan-capped graphene oxide-mesoporous silica nanohybride as pH-responsive nanocarriers," *Journal of Sol-Gel Science and Technology*, vol. 81, no. 2, pp. 493–504, 2017.
- [45] E. Vunain, A. K. Mishra, and B. B. Mamba, "Fundamentals of chitosan for biomedical applications," in *Chitosan Based Biomaterials Volume 1*, Elsevier, 2017, pp. 3–30.
- [46] P. R. Sivashankari and M. Prabakaran, "Chitosan/carbon-based nanomaterials as scaffolds for tissue engineering," in *Biopolymer-Based Composites*, Elsevier, 2017, pp. 381–397.
- [47] R. Justin and B. Chen, "Characterisation and drug release performance of biodegradable chitosan–graphene oxide nanocomposites," *Carbohydrate polymers*, vol. 103, pp. 70–80, 2014.
- [48] B. Yu *et al.*, "Adsorption behavior of copper ions on graphene oxide–chitosan aerogel," *Journal of Environmental Chemical Engineering*, vol. 1, no. 4, pp. 1044–1050, Dec. 2013, doi: <https://doi.org/10.1016/j.jece.2013.08.017>.
- [49] V. Muñoz, T. Kappes, M. Roeckel, J. C. Vera, and K. Fernández, "Modification of chitosan to deliver grapes proanthocyanidins: Physicochemical and biological evaluation," *LWT - Food Science and Technology*, vol. 73, pp. 640–648, 2016, doi: 10.1016/j.lwt.2016.07.006.
- [50] G. K. Jayaprakasha, T. Selvi, and K. K. Sakariah, "Antibacterial and antioxidant activities of grape (*Vitis vinifera*) seed extracts," *Food Research International*, vol. 36, no. 2, pp. 117–122, Jan. 2003, doi: [https://doi.org/10.1016/S0963-9969\(02\)00116-3](https://doi.org/10.1016/S0963-9969(02)00116-3).
- [51] A. M. Panico *et al.*, "The in vitro effect of a lyophilized extract of wine obtained from Jacques grapes on human chondrocytes," *Phytomedicine*, vol. 13, no. 7, pp. 522–526, Jul. 2006, doi: 10.1016/j.phymed.2005.06.009.
- [52] S. Lodhi and A. K. Singhai, "Wound healing effect of flavonoid rich fraction and luteolin isolated from *Martynia annua* Linn. on streptozotocin induced diabetic rats," *Asian Pacific journal of tropical medicine*, vol. 6, no. 4, pp. 253–9, Apr. 2013, doi: 10.1016/s1995-7645(13)60053-x.
- [53] B. S. Nayak *et al.*, "Wound-healing activity of the skin of the common grape (*Vitis Vinifera*) variant, Cabernet Sauvignon," *Phytotherapy research : PTR*, vol. 24, no. 8, pp. 1151–7, Aug. 2010, doi: 10.1002/ptr.2999.
- [54] S. Khanna *et al.*, "Dermal wound healing properties of redox-active grape seed proanthocyanidins," *Free radical biology & medicine*, vol. 33, no. 8, pp. 1089–96, Oct. 2002.

- [55] J. L. Brash, T. A. Horbett, R. A. Latour, and P. Tengvall, “The blood compatibility challenge Part 2: protein adsorption phenomena governing blood reactivity,” *Acta biomaterialia*, 2019.
- [56] C. J. Wilson, R. E. Clegg, D. I. Leavesley, and M. J. Pearcey, “Mediation of Biomaterial–Cell Interactions by Adsorbed Proteins: A Review,” *Tissue Engineering*, vol. 11, no. 1–2, pp. 1–18, Jan. 2005, doi: 10.1089/ten.2005.11.1.
- [57] L. Yu, L. Zhang, and Y. Sun, “Protein behavior at surfaces: Orientation, conformational transitions and transport,” *Journal of Chromatography A*, vol. 1382, pp. 118–134, Feb. 2015, doi: 10.1016/j.chroma.2014.12.087.
- [58] J. L. Ortega-Vinuesa, P. Tengvall, B. Wälivaara, and I. Lundström, “Stagnant versus dynamic conditions: a comparative adsorption study of blood proteins,” *Biomaterials*, vol. 19, no. 1, pp. 251–262, Jan. 1998, doi: 10.1016/S0142-9612(97)00206-8.
- [59] R. E. Baier and R. C. Dutton, “Initial events in interactions of blood with a foreign surface,” *Journal of Biomedical Materials Research*, vol. 3, no. 1, pp. 191–206, 1969, doi: 10.1002/jbm.820030115.
- [60] M. Hadjidemetriou, Z. Al-Ahmady, and K. Kostarelos, “Time-evolution of in vivo protein corona onto blood-circulating PEGylated liposomal doxorubicin (DOXIL) nanoparticles,” *Nanoscale*, vol. 8, no. 13, pp. 6948–6957, Mar. 2016, doi: 10.1039/C5NR09158F.
- [61] L. Vroman, A. L. Adams, G. C. Fischer, and P. C. Munoz, “Interaction of high molecular weight kininogen, factor XII, and fibrinogen in plasma at interfaces,” *Blood*, vol. 55, no. 1, pp. 156–159, Jan. 1980, doi: 10.1182/blood.V55.1.156.156.
- [62] P. Turbill, T. Beugeling, and A. A. Poot, “Proteins involved in the Vroman effect during exposure of human blood plasma to glass and polyethylene,” *Biomaterials*, vol. 17, no. 13, pp. 1279–1287, Jul. 1996, doi: 10.1016/S0142-9612(96)80004-4.
- [63] H. Elwing, S. Welin, A. Askendal, U. Nilsson, and I. Lundström, “A wettability gradient method for studies of macromolecular interactions at the liquid/solid interface,” *Journal of Colloid and Interface Science*, vol. 119, no. 1, pp. 203–210, Sep. 1987, doi: 10.1016/0021-9797(87)90260-8.
- [64] I. H. Jaffer and J. I. Weitz, “The blood compatibility challenge Part 1: Blood-contacting medical devices: The scope of the problem,” *Acta biomaterialia*, 2019.

- [65] C. Morales, M. Roeckel, and K. Fernández, “Microscopic modeling of país grape seed extract absorption in the small intestine,” *AAPS PharmSciTech*, vol. 15, no. 1, pp. 103–110, 2014.
- [66] Y. Chen *et al.*, “Green fabrication of porous chitosan/graphene oxide composite xerogels for drug delivery,” *Journal of Applied Polymer Science*, vol. 131, no. 6, 2014.
- [67] K. H. Van het Hof, G. A. A. Kivits, J. A. Weststrate, and L. B. M. Tijburg, “Bioavailability of catechins from tea: the effect of milk,” *European Journal of Clinical Nutrition*, vol. 52, no. 5, p. 356, 1998.
- [68] P. C. Hollman, “Absorption, bioavailability, and metabolism of flavonoids,” *Pharmaceutical biology*, vol. 42, no. sup1, pp. 74–83, 2004.



4 Design and Characterization of Chitosan-Graphene Oxide Nanocomposites for the Delivery of Proanthocyanidins

This chapter is part of a manuscript published in the *International Journal of Nanomedicine* 2020; 15: 1229–1238, Published online 2020 Feb 20. DOI :10.2147/IJN.S240305 .

The co-authors of the manuscript are mentioned below:



Toribio Figueroa^a, Claudio Aguayo^b, Katherina Fernández^a

^aLaboratory of Biomaterials, Department of Chemical Engineering, Faculty of Engineering, University of Concepción, Concepción, Chile.

^bDepartment of Clinical Biochemistry and Immunology, Faculty of Pharmacy, University of Concepción, Concepción, Chile.

4.1 Abstract

Introduction: In the last years, the utilization of phytomedicines has increased given their good therapeutic activity and fewer side effects compared to allopathic medicines. However, concerns associated with the biocompatibility and toxicity of natural compounds, limit the phytochemical therapeutic action, opening the opportunity to develop new systems that will be able to effectively deliver these substances. This study has developed a nanocomposite of chitosan (CS) functionalized with graphene oxide (GO) for the delivery of proanthocyanidins (PAs), obtained from a grape seed extract (Ext.).

Methods: The GO-CS nanocomposite was covalently bonded and was characterized by Fourier transform infrared spectroscopy (FTIR), X-ray photoelectron spectroscopy (XPS), thermogravimetric analysis (TGA), scanning electron microscopy (SEM), atomic force microscopy (AFM) and by dynamic light scattering (DLS). The loading and release of Ext. from the GO-CS nanocomposite were performed in simulated physiological, and the cytotoxicity of the raw materials (GO and Ext.) and nanocomposites (GO-CS and GO-CS-Ext.) was determined using a human kidney cell line (HEK 293).

Results: The chemical characterization indicated that the covalent union was successfully achieved between the GO and CS, with 44 wt. % CS in the nanocomposite. The GO-CS nanocomposite was thermostable and presented an average diameter of 480 nm (by DLS). The Ext. loading capacity was approximately 20 wt. %, and under simulated physiological conditions, 28.4 wt.% Ext. (g) was released per g of the nanocomposite. GO-CS-Ext. was noncytotoxic, presenting a 97% survival rate compared with 11% for the raw extract and 48% for the GO-CS nanocomposite at a concentration of 500 $\mu\text{g mL}^{-1}$ after 24 hours.

Conclusion: Due to π - π stacking and hydrophilic interactions, GO-CS was reasonably efficient in binding Ext., with high loading capacity and Ext. release from the nanocomposite. The GO-CS nanocomposite also increased the biocompatibility of PAs-rich Ext., representing a new platform for the sustained release of phytodrugs.

4.2 Introduction

In recent decades, the utilization of phytomedicines has increased given their good therapeutic activity and fewer side effects compared to allopathic medicines. One promising phytodrug has arisen in the form of grape seed extract (Ext.), which has a high concentration of proanthocyanidins (PAs). PAs are flavonols, a class of polyphenols that have different substitution patterns in the C₆-C₃-C₆ rings and are present in fruits and vegetables. PAs possess several bioactive effects, including antiviral, anti-inflammatory, cardioprotective, antidiabetic, anticancer, and anti-aging effects, among others [1]. Despite the promising biological activities of raw plant extracts, their poor solubility and stability, short biological half-life, and rapid elimination hinder their clinical application [2]. These aspects, together with concerns associated with the biocompatibility and toxicity of natural compounds, severely limit phytochemical therapeutic action, leading research interests towards the synthesis of systems that are able to effectively deliver these substances [3], [4].

Various carbonaceous materials have been used as drug delivery carriers, including carbon nanotubes, graphene, and graphene oxide (GO). Among these materials, GO stands out for its biomedical applications, enabled by its chemical, physical and mechanical properties [5]. GO has a closely packed honeycomb two-dimensional lattice structure with sp²-bonded carbon atoms and is easily functionalized via π - π interaction with functional groups, such as epoxy, hydroxyl and carboxylic acid groups [6]. Nevertheless, the major drawback of GO for biomedical applications is its jagged edges, which often lead to the disruption of nontargeted cells [7]. Moreover, GO has been reported to exhibit dose-dependent hemolytic activity and controversial cytotoxicity [8]. To minimize the risks associated with the biomedical application of GO, it is often functionalized with biocompatible polymers. A commonly used polymer that interacts with GO is chitosan (CS), which also has favorable properties of mucoadhesivity, biodegradability, antibacterial activity, low immunogenicity, a polyelectrolyte nature and solubility in various media [9]. The cross-linked nature of CS makes it permeable to large molecules [10]. Therefore, CS can be a suitable candidate for the delivery of phytodrugs, such as PAs obtained from Ext.

The GO and CS can be combined to yield favorable properties in a GO-CS composite, to be used as a biocompatible drug delivery agent (or carrier) [11]. Common forms of these composites for drug delivery have included composite films, hydrogels, aerogels, nanofibers and nanoparticles [6]. Nanoparticles have mainly been used for the simultaneous release of genes and

chemotherapy drugs [12]–[14]. Although such carriers are useful for the transport of chemical compounds, no studies have immobilized phytochemicals on GO-CS nanoparticles.

The use of nanoparticles offers the possibility to develop delivery systems that are particularly adapted to improve the therapeutic efficacy of natural bioactive molecules [15]. Indeed, nanocarriers have drawn increasing attention as potential alternatives to traditional formulation approaches, reducing toxicity, increasing bioavailability and permitting site-specific targeted delivery [3].

Thus, this study aimed to develop a GO-CS nanocomposite loaded with Ext. for drug (PAs) delivery. The GO-CS and GO-CS-Ext. nanocomposites were physicochemically characterized; the loading efficiency and release profile of Ext. from the nanocomposite was determined, and the cytotoxicity of both nanocomposites was evaluated and compared to that of the raw materials.



4.3 Materials and Methods

4.3.1 Materials

Graphite powder (Flake, mesh 325) was purchased from Asbury Online (Asbury Carbons, New Jersey, USA). All other chemicals and solvents, such as sulfuric acid (H₂SO₄, 98%), potassium permanganate powder (KMnO₄, 99.9%) and hydrochloric acid (HCl, 37% v/v), were purchased from Merck (Darmstadt, Germany). Ethanol, acetone, 2-propanol, N-(3-dimethylaminopropyl-N-ethylcarbodiimide) hydrochloride (EDC), N-hydroxysuccinimide (NHS), CS, acetic acid, dimethyl sulfoxide (DMSO), 3-(4,5-dimethylthiazol-2-yl)-2,5-diphenyltetrazolium bromide (MTT) reagent, Dulbecco's modified Eagles medium (DMEM), fetal bovine serum (FBS), phosphate-buffered saline (PBS), and 2-(N-morpholino)ethanesulfonic acid (MES) were purchased from Sigma Aldrich (Saint Louis, USA). These chemicals were used as received without further purification. Milli-Q water was used throughout the study. For the sonication treatments, a probe sonicator (Branson 450 model, 42 kHz, 240 W) was used.

4.3.2 País Grape Seed Extract Production

Natural extracts rich in PAs were produced from the seed of grapes from the cultivar País, following the methodology described by Morales et al. (2014). The seeds of 200 País grapes were separated manually and extracted separately in Erlenmeyer flasks with a solution of acetone in water (250 mL, 33% v/v) using a New Brunswick G24 gyratory shaker (New Brunswick Scientific Co., Edison, NJ) for 15 h at room temperature and in the dark to avoid oxidation [16]. The acetone was removed under reduced pressure and temperature (<35 °C) in a rotary evaporator (Bibby Sterilin Ltd., RE-100B, Stone Staffordshire, England) until 50 mL of Ext. remained. The liposoluble compounds in the grape extracts were removed by washing with n-hexane (50 mL, three times).

The raw extracts were purified according to size exclusion chromatography using Toyopearl HW-40F resin packed in an Omnifit column (420 Å, 35 mm, 7 mL min⁻¹) [17]. The column was equilibrated with ethanol/water (55:45, v/v) (two-column volumes). The skin and seed extracts were separately loaded into the column; the sugars and phenolic acids were removed with ethanol/water (55:45, v/v) (three column volumes). This fraction was discarded and not analyzed.

Then, acetone/water (60:40, v/v) (one column volume) was used to elute the PAs fraction. Acetone present in this fraction was evaporated at reduced pressure and temperature (<35 °C), and the seed extracts (Ext.) were lyophilized separately to yield 2.31 mg g⁻¹ grape seed, which was stored at 4 °C for further analysis.

The PAs in each extract was characterized by total phenol content, mean degree of polymerization (mDP) (determined by acid-catalyzed depolymerization (phloroglucinolysis) followed by HPLC detection) [18], average molecular weight (aMW), and molar composition of the extracts. The molecular weight distribution of the extracts was determined by gel permeation chromatography (GPC) [19]. The details of the methodology and results for these assays are presented in Table S1 and Table S2, which are included in the supplementary information.

4.3.3 Preparation of the Chitosan-Grafted GO Nanocomposite (GO-CS)

The GO precursor was synthesized from natural graphite powder using a modified Hummers method [20]. Then, the nanocomposite GO-CS was prepared by the amidation of GO with CS in the presence of EDC and NHS [21]. First, CS (0.5 g, 2.77 mmol) and GO (0.1 g, 0.17 mmol) were dispersed in 50 mL of MES buffer (0.1 M, pH adjusted to 5) and sonicated in a probe sonicator for 15 min to obtain a homogeneous colloidal suspension. EDC (0.652 g, 3.4 mmol) and NHS (0.782 g, 6.8 mmol) were charged into the flask in an inert atmosphere (N₂). The reaction proceeded at room temperature under bath sonication for six h, after which magnetic stirring was performed at 250 RPM for another 16 h. After the reaction was finished, the suspension was washed with an acetic acid solution (0.1 M) to remove unreacted CS. Then, the solid material was redispersed and dialyzed (MW cutoff =12 kDa) against Milli-Q water at 4°C for 3 days. The final product was lyophilized to obtain a powder.

4.3.4 Nanocomposite Characterization

The developed nanocomposites and their components were characterized using different analytical methods. Fourier transform infrared (FTIR) spectroscopy (Perkin Elmer UATR Two FTIR Spectrometer, USA) was used to characterize GO, GO-CS and CS samples at wavenumbers ranging from 500 to 4000 cm⁻¹. X-ray photoelectron spectroscopy (XPS) (Surface Analysis Station, model RQ300/2, USA) was used for the surface chemistry analysis of the samples, with a

monochromatic Al K α X-ray source operating at 15 kV and 5 mA. The core-level spectra were obtained at a photoelectron take-off angle of 90° measured with respect to the sample surface. Thermogravimetric analysis (TGA) was used to evaluate the thermal stability of the GO, CS and GO-CS samples by using a NETZSCH STA 409 PC/PG at a heating rate of 10°C min⁻¹; the temperature was scanned from room temperature to 500°C in a nitrogen atmosphere (100 mL min⁻¹). Atomic force microscopy (AFM) measurements were performed in AC mode using an OmegaScope 1000 (AIST-NT Inc., USA). The samples for AFM were prepared by dropping the GO solutions onto a silica wafer (≈ 0.01 mg mL⁻¹) and incubating for 20 min, followed by washing the samples in 2-propanol and drying them under ambient conditions for 2 h. Scanning electron microscopy (SEM) was performed using a JEOL JSM-6380LV microscope at 10 kV. The aqueous GO and GO-CS suspensions (50 mg mL⁻¹) were freeze-dried for 2 days. The powdered samples were coated using a gold sputter coater, and the surfaces were observed at different resolutions to compare the internal structures. The hydrodynamic size and z-potential of the samples were determined using a dynamic light scattering (DLS) analyzer (SZ-100-Z, Horiba Ltda., Japan). The nanocomposites were suspended in Milli-Q® water at a concentration of 0.05 g L⁻¹. Each sample was measured in a polystyrene container (DTS0012). To confirm Ext. loading, UV-vis spectra of GO-CS and GO-CS-Ext. were recorded by using a Spectroquant® Prove 600 spectrometer (Merck KGaA, Germany) from 250 to 700 nm with a resolution of 0.1 nm. Additionally, UV-vis at 765 nm was used for phenolic concentration determination with Folin-Ciocalteu reagent.

4.3.5 Loading and In-vitro Release of PAs from GO-CS

Initially, 10 mL Milli-Q water was added to 0.5 mg mL⁻¹ GO-CS over the course of one hour to hydrate the powdered nanocomposite. Then, 100 mL Ext. (0.5, 1 and 1.5 mg mL⁻¹) was poured into Milli-Q water solutions of the nanocomposite and magnetically stirred for 72 h. Sixteen samples of supernatant (0.5 mL) were extracted at selected time intervals, and the total phenol concentrations were measured using Folin-Ciocalteu reagent [22]. The nanocomposite was recovered by centrifugation (2000 g, 20 min), resuspended in Milli-Q water (20 mL) and then filtered through a 2 μ m filter to fully remove any solid. The obtained solution was then dialyzed (Spectra/Por® Dialysis membrane, MWCO =12 kDa) against Milli-Q water for 6 h to remove the small amount of solubilized free extract and impurities. The resulting GO-CS-Ext. solution was

preserved at 4°C or lyophilized and then powdered for later use. To evaluate the Ext. release from GO-CS-Ext., 50 mg of GO-CS-Ext. nanocomposite powder was dissolved in 10 mL of PBS, placed into an inner dialysis tube (MWCO =12 kDa) and dialyzed against 90 mL PBS buffer in an outer flask, which was incubated in an orbital shaker (100 rpm) at 37°C for 3 days. At selected time intervals, 0.5 mL of the dialyzate was removed from the flask and replaced with an equal volume of fresh PBS buffer. The difference in total phenol content between the original PBS solution and the dialyzate (with dissolved extract) at time t_i was determined by Folin-Ciocalteu assay [22], using a Spectroquant® Prove 600 (Merck KGaA, Germany) at a wavelength of 765 nm. The amount of extract released from the nanocomposite, $Qd(t_i)$, at time t_i was calculated using the following equation: $Qd(t_i) = qd(t_i) m^{-1}$, where $qd(t_i)$ is the content of total phenols in the medium (mg eq. gallic acid mg^{-1} extract) and m is the mass of nanocomposite (mg).

4.3.6 *In vitro* Cytotoxicity Study of the Nanocomposites

The cytotoxicity was determined using the MTT assay. HEK 293 cells (purchased from Merck KGaA, Germany) were cultured in DMEM medium supplemented with 5% heat-inactivated FBS, 100 units per mg penicillin, and 100 $\mu\text{g mL}^{-1}$ streptomycin at 37 °C, 5% CO_2 , and 95% relative humidity. MTT was used as an indicator of cell viability as determined by its mitochondrial-dependent reduction to formazan. In detail, 100 μL of cells were seeded into 96-well plates at a density of 10^5 cells mL^{-1} . After incubation for 24 h, the culture media were replaced with fresh media (100 μL) containing free extract, GO-CS or GO-CS-Ext. at selected concentrations (50, 100, 200, 250, 300, 400 and 500 mg mL^{-1}) for an additional 24 h. In the case of GO-CS-Ext., the concentration of Ext. released was calculated based on previous studies of drug loading and release, e.g., to obtain a 100 $\mu\text{g mL}^{-1}$ Ext. concentration in media culture, 1.6 mg mL^{-1} GO-CS-Ext. should be used to yield an equivalent concentration to that of free extract. After the cells were washed with PBS to remove the media and remaining particles, 10 μL MTT (5 mg mL^{-1} in PBS) was added to the wells for 4 h. Then, the supernatant was removed by aspiration, and the formazan crystals were dissolved in DMSO (100 μL per well), followed by shaking for 5 min. The absorbance was read using a microplate reader (Spectra Plus, TECAN, USA) at a wavelength of 570 nm. The cell viability (%) relative to control cells was calculated from $A_{\text{test}}/(A_{\text{control}}) \times 100\%$, where A_{test} and A_{control} are the absorbance values of the wells (with the

nanocomposites) and control wells (without the nanocomposites), respectively. For each sample, the final absorbance was the average of measured values from six wells in parallel.

4.3.7 Statistics

All experimental designs were performed at least in triplicate, and the results are expressed as arithmetic means with the standard deviation (mean \pm S.D.), as determined using Statgraphics Centurion XVI® software, with a statistical significance of $p \leq 0.05$. The mean values and the error bars are reported in each figure.



4.4 Results

4.4.1 Characterization of GO-CS Nanocomposites

In the FTIR spectra (Figure 4-1), GO shows the following characteristic peaks: 3354 cm^{-1} , indicating O-H deformation; 1710 cm^{-1} , corresponding to C=O bonds; 1599 cm^{-1} , corresponding to C=C bonds; and 1386 cm^{-1} and 1042 cm^{-1} , indicating the presence of C-O groups. The CS spectra show peaks at 3294 cm^{-1} (O-H deformation); 1715 cm^{-1} , indicating the presence of C=O bonds; 1554 cm^{-1} , corresponding to the bending of N-H in amide groups; and 1460 cm^{-1} and 1030 cm^{-1} , corresponding to C-O bonds. The GO-CS spectra show peaks at 3352 cm^{-1} (O-H distortion) and 1634 cm^{-1} , as well as a superposition band assigned to the amine groups of CS and carboxylated groups of GO, 1333 cm^{-1} and 1245 cm^{-1} , indicating C-O bonds. Additionally, the characteristic signal of secondary amides (N-H bending) shifts from 1541 to 1569 cm^{-1} (between the CS and GO-CS signals).

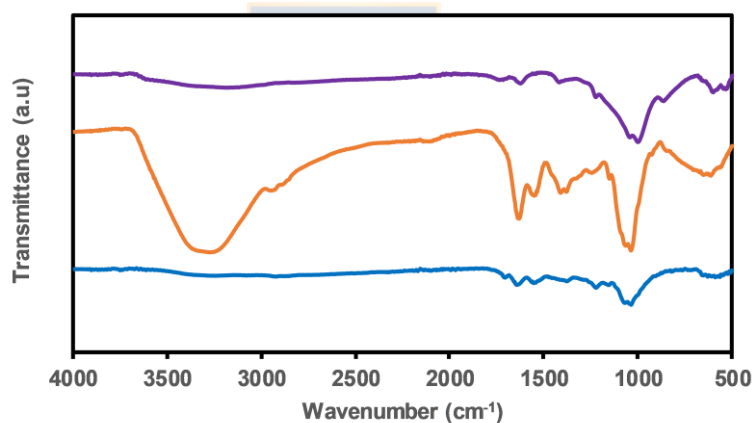


Figure 4-1 FTIR of GO (blue), CS (purple) and GO-CS (orange)

The XPS spectra of GO, GO-CS, and CS are shown in Figure 4-2, where the GO spectrum differs from those of CS and GO-CS by the absence of the N 1s band at 399 e.V. Figures 4-3 (c) and 4-4 (d) compare the N 1s peaks after deconvolution, and the area ratios were evaluated to determine the compositions. The N 1s bands existing only in CS and GO-CS represent N-C (398.6 e.V.), amine C-NH₂ (399 e.V.), amide N-C=O (400.5 e.v.) and protonated C-NH₄⁺ bonds (401.6 e.V.). The area ratio of the amide bond peak increased from 12.7% in CS to 24.8% in the GO-CS nanocomposite, and a decrease in the amine peak from 32.2% in CS to 23.6% in GO-CS was observed.

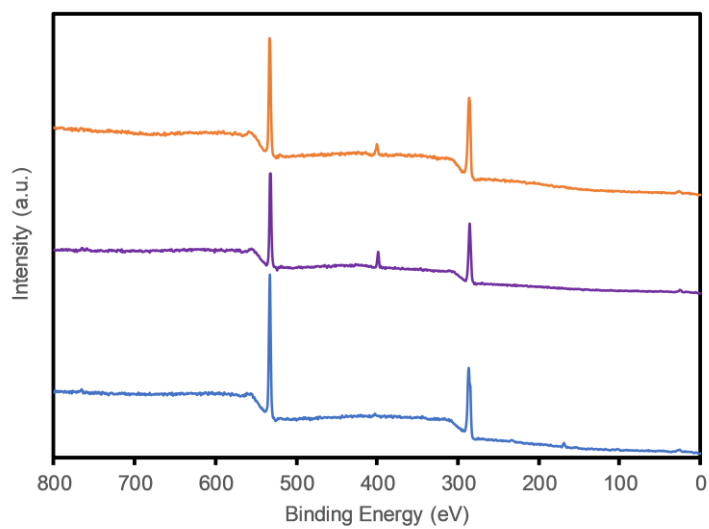


Figure 4-2 XPS spectra of GO (blue), CS (purple) and GO-CS (orange)

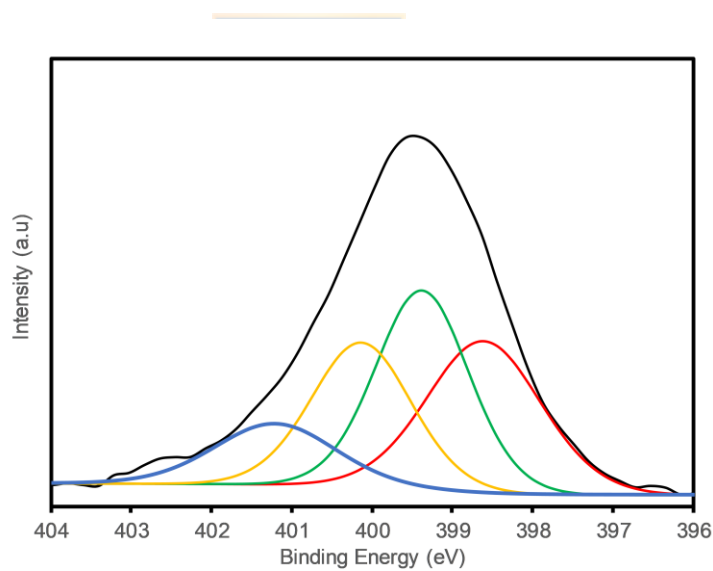


Figure 4-3 The N 1s band (black) of CS with the deconvoluted peaks of N-C (red), amine C-NH₂ (green), amide N-C=O (yellow) and protonated C-NH₄⁺ (blue) bonds.

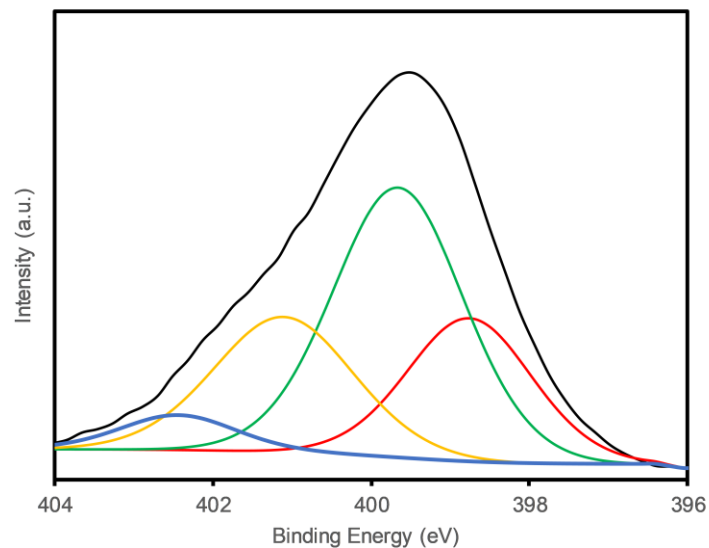


Figure 4-4 The N 1s band (black) of GO-CS with the deconvoluted peaks of N-C (red), amine C-NH₂ (green), amide N-C=O (yellow) and protonated C-NH₄⁺ (blue) bonds.

TGA revealed the composition and changes in the thermal stability of the GO, CS and GO-CS nanocomposite (Figure 4-5). GO and GO-CS start to lose mass below 120°C, and mass loss decreases rapidly close to 196 °C; for CS, the mass loss begins sooner. The DTG curves show rapid weight loss in GO at 198 °C and CS at 240 °C and show 2 rapid weight loss peaks in the GO-CS nanocomposite at 203 °C and 255 °C (the DTG curves are shown in Figure 7-1 in the supplementary information). Finally, at 400°C, GO-CS shows a 48% weight loss, whereas GO and pure CS have weight losses of 32% and 61%, respectively. Based on these results, we calculated a 44% mass content of CS in the GO-CS nanocomposite.

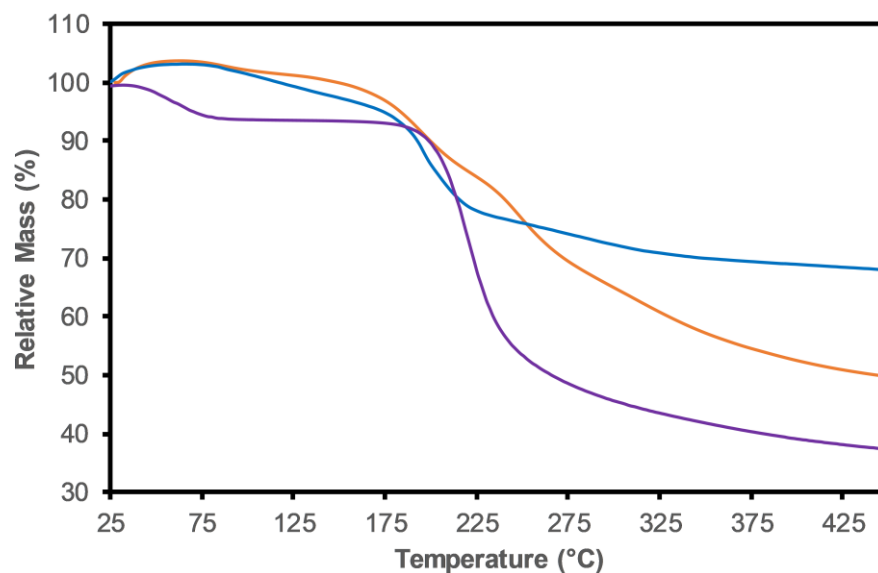


Figure 4-5 TGA curves of GO (blue), CS (purple) and GO-CS (orange).

The GO surface morphology was analyzed by SEM (Figure 4-8). The GO sheets became smooth and layered in macrostructures formed during lyophilization during sample preparation. The particle morphology was further analyzed by AFM (Figure 4-7), where a GO-CS sheet was isolated with a diameter of 850 nm. This value was higher than the hydrodynamic diameter measured by DLS (480 ± 70 nm), probably caused by the AFM sampling preparation technique. Additionally, a height profile (Figure 4-6) was extracted, and a single plane of a GO-CS particle presented a 1.5 nm height. Finally, a CS particle approx. 3 nm in height can be seen on the sheet border. The z-potential of the GO was -54.7 ± 4.1 mV, and this value changed as a result of CS addition to $+47.2 \pm 3.2$ mV for the GO-CS nanocomposite.

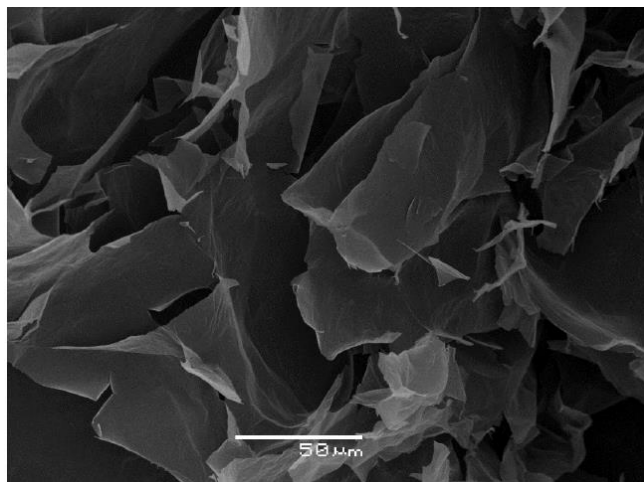


Figure 4-6) SEM image of a GO sample

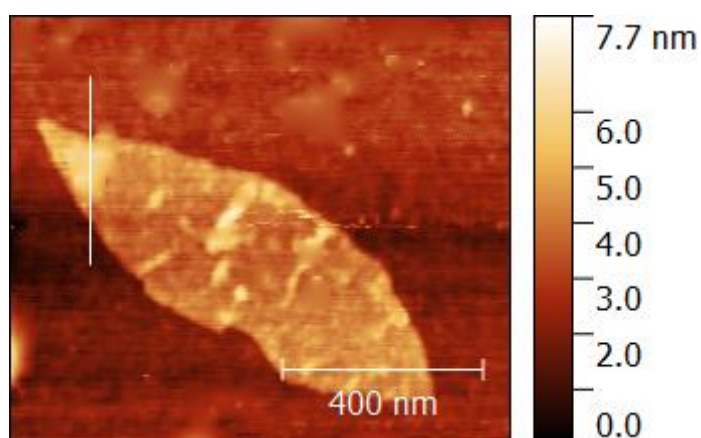


Figure 4-8 No-contact AFM image of a GO-CS sheet

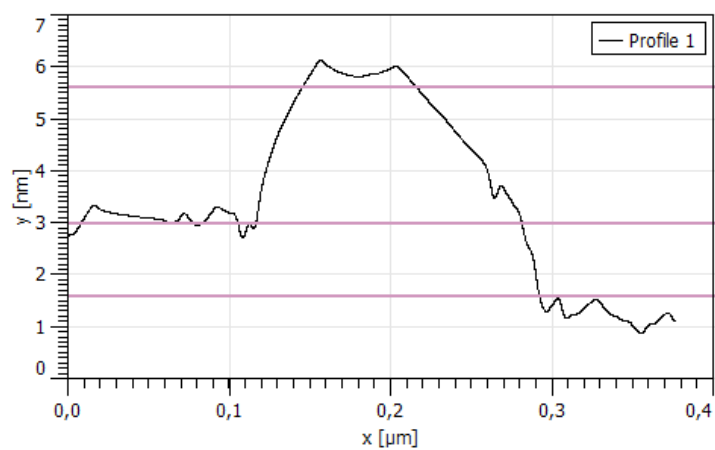


Figure 4-7 Extracted height profile of a GO-CS sample from AFM.

4.4.2 Loading and Release of PAs

The loading of Ext. onto the GO-CS nanocomposite was evidenced via UV-Vis spectra (Figure 4-9), which show absorbance peaks at 300 nm for the GO-CS nanocomposite and 300 nm for the GO-CS-Ext. spectrum. The shift of 30 nm is explained by the strong π - π interactions and hydrogen bonds between Ext. and the hydrophobic zones of the GO surface and hydrogen bonds with oxygenated groups.

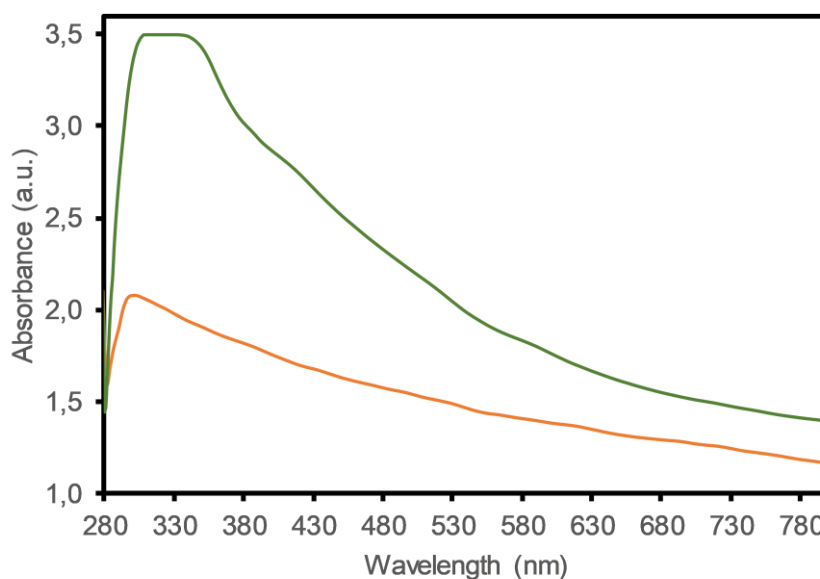


Figure 4-9) UV-Vis absorption spectra of GO-CS (orange) and loaded GO-CS-Ext. (green).

The adsorption of the extract on the nanocomposite is shown in Figure 4-10 (left axis). In the beginning, high-speed adsorption was observed, and after only 5 min, smooth changes were present (approx. 20% absorbed). After 25 min, the sample measurements were not significantly different, reaching a steady-state (data not shown). The extract loading capacity on the GO-CS nanocomposite was 0.22 ± 0.02 g (n =6) of extract per g of nanocomposite (equivalent to 72.8 μ mol of extract per g of nanocomposite). With extract loading, the electrical charge of the nanocomposite surface was reduced from $+47.2 \pm 3.1$ mV for GO-CS to $+30.5 \pm 1.6$ mV for GO-CS-Ext.

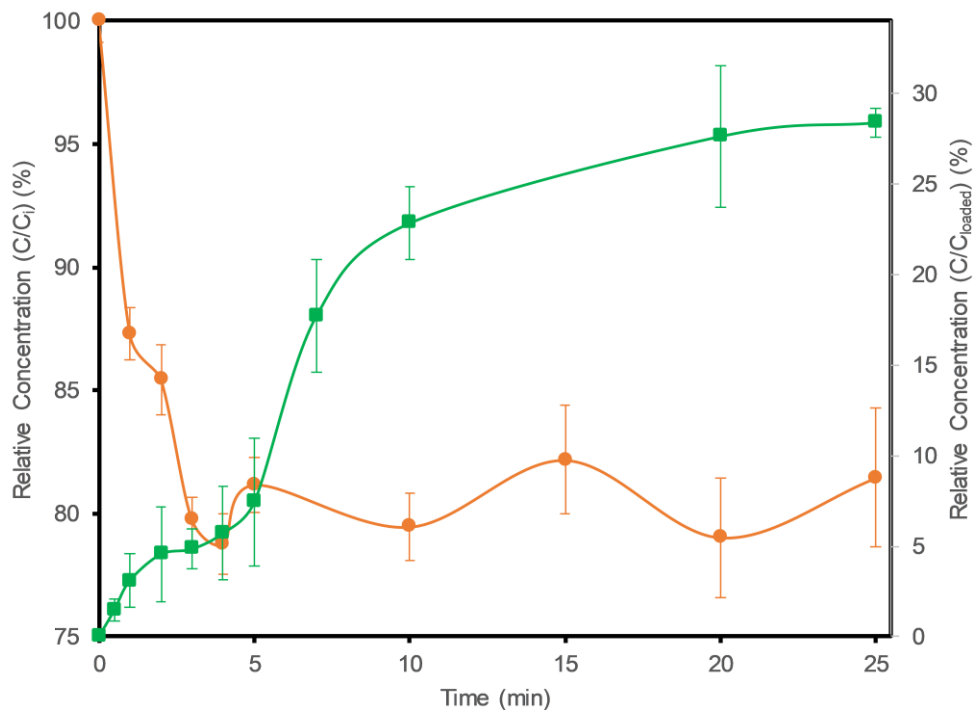


Figure 4-10 Adsorption profile of Ext. on GO-CS in water (orange ●) and in vitro release profile of Ext. from GO-CS-Ext. (green ■) in PBS buffer (pH 7.4) at 37 ° C.

The release profile of PAs extract from GO-CS was simulated under physiological conditions (PBS, pH 7.4, 37 °C). In the profile (Figure 4-10 right axis), a change in velocity was observed at approximately 5 min, but release then occurred until 10 min, reaching a plateau value close to 25 min. No significant difference was observed after 24 h of sampling (data not shown). Thus, 28.4% (in mass) of the loaded extract in the nanocomposite was released in 25 min.

4.4.3 Cell Viability

In this study, we used human embryonic kidney (HEK) cells as an *in vitro* model since the kidney participates in the metabolism of flavonoids in the body [23]. Figure 4-11 presents the cell viability of HEK cells, measured by MTT assay, for GO, Ext. and nanocomposites. GO cytotoxicity (blue line) was not present below 100 $\mu\text{g mL}^{-1}$ ($p < 0.05$ compared with the control). Higher concentrations of GO particles decreased the cell viability ($p < 0.05$) via a directly dependent relation, with only 48% viability of the cell population at 500 $\mu\text{g mL}^{-1}$. The addition of CS to form the GO-CS nanocomposite (orange line) increased the cell viability for all tested concentrations

studied. The samples did not show a significant difference from the control ($p>0.05$), with a 97% survival rate observed at a concentration of $500 \mu\text{g mL}^{-1}$.

The cell viability of the raw extract (red line) decreased rapidly with increasing concentration compared with the control ($p<0.05$), reaching 11% at $500 \mu\text{g mL}^{-1}$ extract (165 mM). The immobilization of the extract on the GO-CS nanocomposite increased cell viability for all the extract concentrations evaluated (green line), showing no significant difference from the control ($p>0.05$), with the final cell viability of 97% at $500 \mu\text{g mL}^{-1}$ extract (165 mM).

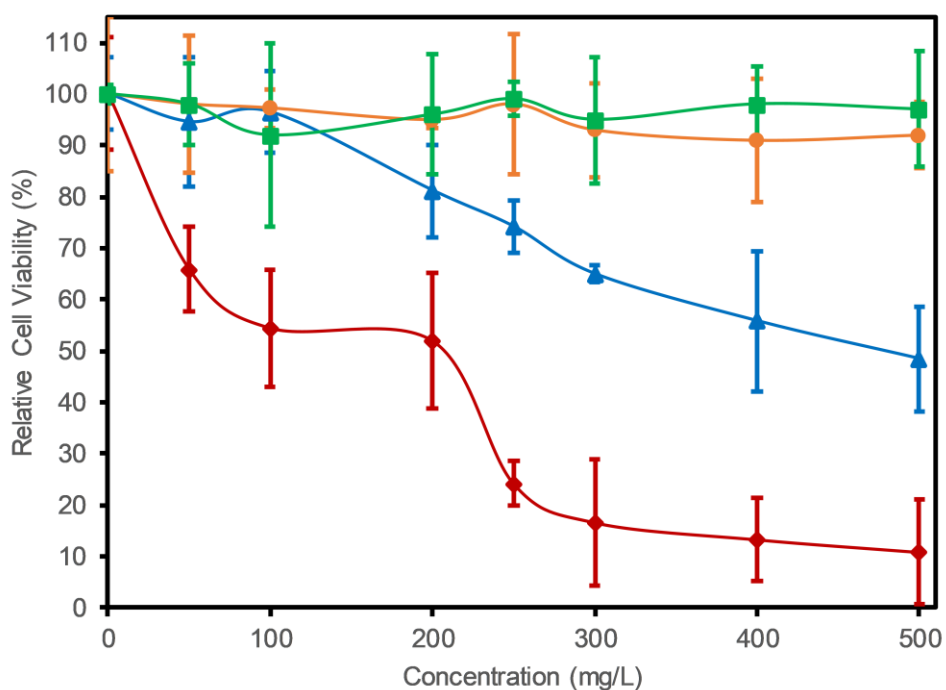


Figure 4-11 *In vitro* cell toxicity assay. Relative cell viability of HEK cells treated with GO (blue ▲), Ext. (dark red ◆), GO-CS (orange ●) and GO-CS-Ext. (green ■) at different concentrations. Controls were cells without the addition of the studied samples.

4.5 Discussion

To form the GO-CS nanocomposites, we used a covalent combination of GO and CS, as reported in Bao et al (2011). The covalent bonding between GO and CS was evidenced by FTIR spectroscopy, presenting peaks at 3294 cm^{-1} , indicative of CS and GO conjugation, and 3352 cm^{-1} , corresponding to GO-CS bonds, as previously reported [21]. The XPS spectra showed a C 1s energy shift, indicating the influence of graphene's aromatic carbon multiple bonds on the CS chains [10], [24]. Furthermore, the proportional area of the characteristic signal of secondary amides increased, indicating the presence of newly formed amide bonds between the carboxylic groups of GO and the amine groups of CS.

The unexpected variations at the beginning of the TGA curve below $120\text{ }^{\circ}\text{C}$ can be attributed to the volatilization of stored water in the π -stacked structure of the nanocomposite [25]. The reaction used to compare the samples occurred at approximately $200\text{ }^{\circ}\text{C}$ and is attributed to the pyrolysis of labile oxygen-containing groups [26]. TGA also confirmed the union of GO-CS through the difference in degradation temperature between GO and GO-CS (from $240\text{ }^{\circ}\text{C}$ to $255\text{ }^{\circ}\text{C}$), which is associated with the enhanced thermal stability of GO resulting from the union with CS chains. Also, TGA indicated a mass composition of 44% CS on the nanocomposite, which was higher than the 32% reported by Bao *et al* (2011) in their work investigating GO-CS nanoparticle synthesis. The higher amount of CS in the composition of the GO-CS nanocomposite might be due to the higher average molecular weight (aMW) of the CS used in our synthesis. In this study, we used CS with a MW of 50 kDa, in contrast to the 3 kDa CS used by Bao *et al* (2011). A higher aMW of CS chains has a reported positive effect on the drug loading capacity of the carrier but also an adverse effect on the amount of drug released [27]. Nevertheless, a negative effect was not observed in our results, which showed higher cumulative drug release than the work of Bao *et al* (2011), possibly attributed to different mass transfer limitations or a different process of desorption between the grape extract used in this study and the nanocomposite.

Once we confirmed the covalent union of GO-CS, the nanocomposite morphology was studied using AFM. The particle images show CS bonded on the GO surface, especially on the borders of GO sheets, which could be caused by carboxylic groups at the GO edge, as part of the amidation reaction [26]. Additionally, the height profile shows a larger GO sheet width of 1.5 nm compared with the literature value of approximately 0.9 nm [5], which can be attributed to bilayer

GO sheet formation or oxygenated groups on the planar surface and borders of the GO [25]. The particle size determined from AFM images was higher than that obtained from DLS, probably due to the AFM sampling preparation technique, where isolating large GO particles on the silica wafer is easier than isolating smaller particles [25]. Based on the previous analyses, we achieved the successful formation of amidic bonds between GO and CS to produce a thermally stable nanocomposite.

The loading of Ext. on the nanocomposite was first studied via UV-vis, where a wavenumber shift of 30 nm between GO-CS and GO-CS-Ext. was observed and was explained by the strong π - π interactions and hydrogen bonds of Ext. with the GO's oxygenated groups [28]. Various drugs have been successfully loaded onto GO via π - π stacking interactions between the large π -conjugated structure of GO and aromatic structures, such as PAs, on the Ext. [29], The GO-CS-Ext. composite showed a good loading capacity of approximately 20 wt.% compared with studies of other graphitic materials and polyphenolic compounds³⁰ or other GO nanocomposites bound with CS and folic acid [31]. Furthermore, the incorporation of CS and Ext. stabilized the GO-CS-Ext. nanocomposite, changing the surface charge from negative to positive, which is a previously observed stabilizing property of CS [32].

The release profile of Ext. from GO-CS indicated rapid liberation, reaching a stable value in 25 min. In comparison to the results observed in the study of Bao *et al* (2011), who used camptothecin as a loading drug, our release profile was different. The faster liberation and the higher amount released can be attributed to different mass transfer limitations or a different process of desorption between the Ext. and the GO-CS nanocomposite [33]. One important and well-reported effect on synthetic phenolic drug loading and release is dependence on pH; for example, Khoe *et al* (2017) synthesized chitosan-coated GO mesoporous silica nanoparticles and showed that the cumulative release of doxorubicin at lower pH was higher than that at physiological pH³³. In another study, Chen *et al* (2014) showed the same behavior by a GO and CS xerogel loaded with doxorubicin when the nanocomposite was in acidic media [34]. This process might also affect the amount of Ext. released at physiological pH (7.4).

The total amount of released extract from the GO-CS-Ext. nanocomposite (165 mM) was comparable with the results of *in vivo* bioactivity studies of similar flavonoids. Van het Hof *et al* (1998) showed that after green tea consumption (3 g), which was equivalent to 0.9 g of catechins, the maximum blood concentration of catechins reached was 0.53 μ M (approx. 300 times lower

than our cell culture doses)[35]. Additionally, Hollman (2004) reported a maximum blood concentration of 0.08 μM in humans after an oral dose of 630 μmol PAs from chocolate ingestion[23]. Comparing our results with the abovementioned results, we can assume that the GO-CS-Ext. nanocomposite will have observable bioactivity in humans or animals, considering the higher bioeffect attributable to the use of the developed nanocomposite delivery system.

The synthesis of nanocomposites for drug delivery is usually designed to reduce the toxicity of their components [6], [24]. In our case, we evaluated the cell viability of kidney cells (HEK) in the presence of CS, GO, Ext. and nanocomposites at concentrations up to 500 $\mu\text{g mL}^{-1}$. The GO-CS nanocomposite had lower cytotoxicity than free GO and the GO-CS-Ext. complex was not cytotoxic compared with the raw extracts, probably due to CS interacting ionically with the negatively charged GO and Ext., forming polyelectrolyte complexes that interact better than their components with the negatively charged cell membrane, thus reducing cytotoxicity [9]. Liao *et al* (2011) showed that GO nanoparticles have good cell viability on fibroblasts (>90% by MTT assay at a concentration of 200 $\mu\text{g mL}^{-1}$)[36]. In another study, Sasidharan *et al* (2012) showed that GO nanoparticles have good hemocompatibility (>90% at a concentration of 75 $\mu\text{g mL}^{-1}$). These studies present models for some of the biological barriers to drug pharmacokinetics. Nevertheless, GO-CS toxicity using kidney cells as a biological model has not been reported until now, and the results showed no cytotoxicity of the developed nanocomposites.

Since Ext. molecules pass through the plasma membrane by passive diffusion [37], a high dose is needed to achieve cell permeation, which can be accomplished by delivery with this nanocomposite. Complexes of drugs and GO-CS may be internalized by cells mainly through an efficient endocytic process [21]. The positive charge of the nanocomposite, confirmed by the z-potential, may also improve the cellular uptake of GO-CS-Ext. via electrostatic interaction with the negatively charged cell membrane [6]. As a drug delivery system, the GO-CS-Ext. nanocomposite presents great potential as a support for the evaluated phyto drug.

4.6 Conclusion

Currently, in medicine, drug delivery is important for actual drug bioactivity, especially for phytodrugs, which have beneficial properties but are easily degraded under physiological conditions. In this study, we report the synthesis of CS-functionalized GO as a nanocomposite to deliver Ext., which is rich in flavonoids and evaluate its cytotoxicity on a human kidney cell line. Due to π - π stacking and hydrophilic interactions, GO-CS was reasonably efficient in binding Ext., with a high loading content of approximately 20 wt.%. Ext. release from the nanocomposite *in vitro* in simulated physiological media reached 28.4 wt.% of the mass originally loaded. The GO-CS-Ext. complexes were found to be nontoxic to kidney cells compared with the raw extract at the concentrations studied. Based on the above results, the GO-CS nanocomposite could increase the biocompatibility of Ext. and could be used as a new phytodrug delivery carrier. In further studies, we suggest *in vivo* confirmation of the biocompatibility of the loaded GO-CS-Ext. composite.



4.7 References

- [1] V. Georgiev, A. Ananga, and V. Tsoleva, "Recent advances and uses of grape flavonoids as nutraceuticals," *Nutrients*, vol. 6, no. 1, pp. 391–415, 2014, doi: 10/f5qzgb.
- [2] N. Vale, A. Ferreira, J. Matos, P. Fresco, and M. J. Gouveia, "Amino Acids in the Development of Prodrugs," *Molecules (Basel, Switzerland)*, vol. 23, no. 9, p. 2318, 2018, doi: 10.3390/molecules23092318.
- [3] T. Gunasekaran, T. Haile, T. Nigusse, and M. D. Dhanaraju, "Nanotechnology: an effective tool for enhancing bioavailability and bioactivity of phytomedicine," *Asian Pacific journal of tropical biomedicine*, vol. 4, no. Suppl 1, pp. S1-7, May 2014, doi: 10.12980/apjtb.4.2014c980.
- [4] R. Conte, I. De Luca, A. De Luise, O. Petillo, A. Calarco, and G. Peluso, "New Therapeutic Potentials of Nanosized Phytomedicine," *Journal of nanoscience and nanotechnology*, vol. 16, no. 8, pp. 8176–8187, Aug. 2016, doi: 10.1166/jnn.2016.12809.
- [5] C. emsp14N emsp14R Rao, A. emsp14K Sood, K. emsp14S Subrahmanyam, and A. Govindaraj, "Graphene: the new two-dimensional nanomaterial," *Angewandte Chemie International Edition*, vol. 48, no. 42, pp. 7752–7777, 2009, doi: 10.1002/anie.200901678.
- [6] S. Gooneh-Farahani, M. R. Naimi-Jamal, and S. M. Naghib, "Stimuli-responsive graphene-incorporated multifunctional chitosan for drug delivery applications: a review," *Expert opinion on drug delivery*, vol. 16, no. 1, pp. 79–99, 2019.
- [7] A. Sasidharan *et al.*, "Hemocompatibility and macrophage response of pristine and functionalized graphene," *Small*, vol. 8, no. 8, pp. 1251–1263, 2012.
- [8] N. V. Vallabani *et al.*, "Toxicity of graphene in normal human lung cells (BEAS-2B)," *Journal of biomedical nanotechnology*, vol. 7, no. 1, pp. 106–107, 2011, doi: 10/ckt2xq.
- [9] S. A. Agnihotri, N. N. Mallikarjuna, and T. M. Aminabhavi, "Recent advances on chitosan-based micro-and nanoparticles in drug delivery," *Journal of controlled release*, vol. 100, no. 1, pp. 5–28, 2004.
- [10] Y. Pan, T. Wu, H. Bao, and L. Li, "Green fabrication of chitosan films reinforced with parallel aligned graphene oxide," *Carbohydrate Polymers*, vol. 83, no. 4, pp. 1908–1915, Feb. 2011, doi: 10/bnn3fm.
- [11] X. Song *et al.*, "Construction of blood compatible chitin/graphene oxide composite aerogel beads for the adsorption of bilirubin," *Carbohydrate polymers*, vol. 207, pp. 704–712, 2019.
- [12] X. Zhao *et al.*, "Design and development of graphene oxide nanoparticle/chitosan hybrids showing pH-sensitive surface charge-reversible ability for efficient intracellular doxorubicin delivery," *ACS applied materials & interfaces*, vol. 10, no. 7, pp. 6608–6617, 2018, doi: 10/gd4t9k.

- [13]S. S. Saravanabhavan *et al.*, “Graphene oxide functionalized with chitosan based nanoparticles as a carrier of siRNA in regulating Bcl-2 expression on Saos-2 & MG-63 cancer cells and its inflammatory response on bone marrow derived cells from mice,” *Materials Science & Engineering C-Materials for Biological Applications*, vol. 99, pp. 1459–1468, Jun. 2019, doi: 10.1016/j.msec.2019.02.047.
- [14]F. Zhang *et al.*, “Chitosan and dextran stabilized GO-iron oxide nanosheets with high dispersibility for chemotherapy and photothermal ablation,” *Ceramics International*, vol. 45, no. 5, pp. 5996–6003, Apr. 2019, doi: 10.1016/j.ceramint.2018.12.070.
- [15]S. S. Bansal, M. Goel, F. Aqil, M. V. Vadhanam, and R. C. Gupta, “Advanced drug delivery systems of curcumin for cancer chemoprevention,” *Cancer prevention research*, vol. 4, no. 8, pp. 1158–1171, 2011.
- [16]C. Morales, M. Roeckel, and K. Fernández, “Microscopic modeling of país grape seed extract absorption in the small intestine,” *AAPS PharmSciTech*, vol. 15, no. 1, pp. 103–110, 2014.
- [17]K. Fernández, J. A. Kennedy, and E. Agosin, “Characterization of Vitis vinifera L. Cv. Carménère grape and wine proanthocyanidins,” *Journal of Agricultural and Food Chemistry*, vol. 55, no. 9, pp. 3675–3680, 2007, doi: 10.1021/jf063232b.
- [18]J. A. Kennedy and G. P. Jones, “Analysis of proanthocyanidin cleavage products following acid-catalysis in the presence of excess phloroglucinol,” *Journal of Agricultural and Food Chemistry*, vol. 49, no. 4, pp. 1740–1746, 2001.
- [19]V. M. Williams, L. J. Porter, and R. W. Hemingway, “Molecular weight profiles of proanthocyanidin polymers,” *Phytochemistry*, vol. 22, no. 2, pp. 569–572, 1983.
- [20]D. C. Marcano *et al.*, “Improved synthesis of graphene oxide,” *ACS nano*, vol. 4, no. 8, pp. 4806–4814, 2010, doi: 10/bp734k.
- [21]H. Bao *et al.*, “Chitosan-functionalized graphene oxide as a nanocarrier for drug and gene delivery,” *Small*, vol. 7, no. 11, pp. 1569–1578, 2011, doi: 10/c7k2nc.
- [22]M. Jerez, J. Sineiro, and M. J. Nuñez, “Fractionation of pine bark extracts: selecting procyanidins,” *European Food Research and Technology*, vol. 229, no. 4, pp. 651–659, 2009.
- [23]P. C. Hollman, “Absorption, bioavailability, and metabolism of flavonoids,” *Pharmaceutical biology*, vol. 42, no. sup1, pp. 74–83, 2004.
- [24]X. Yang, Y. Tu, L. Li, S. Shang, and X. Tao, “Well-dispersed chitosan/graphene oxide nanocomposites,” *ACS applied materials & interfaces*, vol. 2, no. 6, pp. 1707–1713, 2010.
- [25]D. Han, L. Yan, W. Chen, and W. Li, “Preparation of chitosan/graphene oxide composite film with enhanced mechanical strength in the wet state,” *Carbohydrate Polymers*, vol. 83, no. 2, pp. 653–658, Jan. 2011, doi: 10/ctv2gj.

- [26] T. Budnyak, I. Pylypchuk, V. Tertykh, E. S. Yanovska, and D. Kołodyńska, "Synthesis and adsorption properties of chitosan-silica nanocomposite prepared by sol-gel method," *Nanoscale research letters*, vol. 10, p. 87, Dec. 2015, doi: 10/gfb8w3.
- [27] A. R. Dudhani and S. L. Kosaraju, "Bioadhesive chitosan nanoparticles: Preparation and characterization," *Carbohydrate Polymers*, vol. 81, no. 2, pp. 243–251, 11 2010, doi: <http://dx.doi.org/10.1016/j.carbpol.2010.02.026>.
- [28] C.-P. Yu, C.-S. Shia, S.-Y. Tsai, and Y.-C. Hou, "Pharmacokinetics and relative bioavailability of flavonoids between two dosage forms of gegen-qinlian-tang in rats," *Evidence-Based Complementary and Alternative Medicine*, vol. 2012, 2012.
- [29] J. Liu, L. Cui, and D. Losic, "Graphene and graphene oxide as new nanocarriers for drug delivery applications," *Acta biomaterialia*, vol. 9, no. 12, pp. 9243–9257, 2013, doi: 10/gd4t9p.
- [30] E. Hashemi, O. Akhavan, M. Shamsara, R. Rahighi, A. Esfandiari, and A. R. Tayefeh, "Cytotoxicities of graphene oxide and reduced graphene oxide sheets on spermatozoa," *Rsc Advances*, vol. 4, no. 52, pp. 27213–27223, 2014, doi: 10/gd4t9n.
- [31] A. Deb and R. Vimala, "Camptothecin loaded graphene oxide nanoparticle functionalized with polyethylene glycol and folic acid for anticancer drug delivery," *Journal of Drug Delivery Science and Technology*, vol. 43, pp. 333–342, 2018, doi: 10/gdcp22.
- [32] M. Collado-González, M. G. Montalbán, J. Peña-García, H. Pérez-Sánchez, G. Vllora, and F. G. D. Baños, "Chitosan as stabilizing agent for negatively charged nanoparticles," *Carbohydrate polymers*, vol. 161, pp. 63–70, 2017.
- [33] S. Khoei, R. Bafkary, and F. Fayyazi, "DOX delivery based on chitosan-capped graphene oxide-mesoporous silica nanohybrid as pH-responsive nanocarriers," *Journal of Sol-Gel Science and Technology*, vol. 81, no. 2, pp. 493–504, 2017.
- [34] Y. Chen *et al.*, "Green fabrication of porous chitosan/graphene oxide composite xerogels for drug delivery," *Journal of Applied Polymer Science*, vol. 131, no. 6, 2014.
- [35] K. H. Van het Hof, G. A. A. Kivits, J. A. Weststrate, and L. B. M. Tjburg, "Bioavailability of catechins from tea: the effect of milk," *European Journal of Clinical Nutrition*, vol. 52, no. 5, p. 356, 1998.
- [36] K.-H. Liao, Y.-S. Lin, C. W. Macosko, and C. L. Haynes, "Cytotoxicity of graphene oxide and graphene in human erythrocytes and skin fibroblasts," *ACS applied materials & interfaces*, vol. 3, no. 7, pp. 2607–2615, 2011.
- [37] C. Manach, G. Williamson, C. Morand, A. Scalbert, and C. Remesy, "Bioavailability and bioefficacy of polyphenols in humans. I. Review of 97 bioavailability studies," *American Journal of Clinical Nutrition*, vol. 81, no. 1, pp. 230S–242S, Jan. 2005.

5 Synthesis and Characterization of Flavan-3-ols Reinforced Graphene Oxide Chitosan Aerogels as Hemostatic Agent

This chapter is part of a manuscript submitted for publication, which is currently under review by the journal Colloids and Surfaces B: Biointerfaces. The co-authors of the manuscript are listed below:

Toribio Figueroa^a, Satchary Carmona^a, Sebastian Guajardo^a, Jessica Borges^a, Claudio Aguayo^b, Katherina Fernández^a



^aLaboratory of Biomaterials, Department of Chemical Engineering, Faculty of Engineering, University of Concepción, Concepción, Chile.

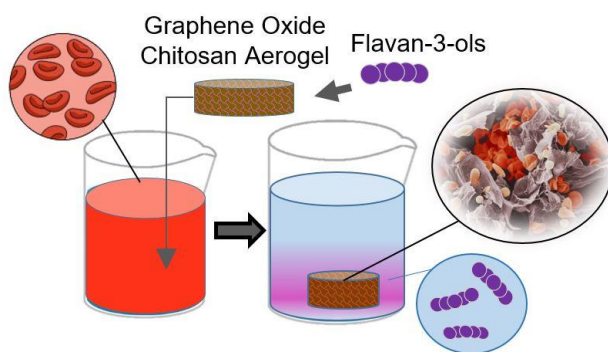
^bDepartment of Clinical Biochemistry and Immunology, Faculty of Pharmacy, University of Concepción, Concepción, Chile.

5.1 Abstract

The natural mechanisms of the body cannot control massive hemorrhaging, resulting in a requirement for hemostatic intervention. In this study, graphene oxide and chitosan aerogels reinforced with grape seed (SD) and skin (SK) extracts were developed for use as hemostatic agents by evaluating the influence of pH on their synthesis, as well as of the amount of grape extract added on the physical and chemical properties of the aerogels.

The materials were evaluated by FTIR, XRD, Raman spectroscopy, DLS, uniaxial compression tests and SEM. The capacity of the aerogels to absorb water, PBS and blood, as well as their coagulation capacity, were determined. In addition, the release profile for grape extracts in PBS and the material's cytotoxicity were determined.

The aerogels synthesized under basic conditions and loaded with grape extracts were more rigid and negatively charged, and they contained smaller pores than the un-loaded acidic aerogels. For all aerogels, hemoglobin absorption exceeded 90% in the first 30 seconds. A higher density of adsorbed blood cells was observed on aerogels loaded with a higher amount of grape extract. The maximum release of extract from the aerogels occurred for those loaded with SK extracts at a basic pH; the aerogels prepared under acidic conditions dissolved in the media. Aerogels loaded with SK extracts under alkaline conditions were not cytotoxic toward human dermal fibroblasts and exhibited cell viabilities above 90%. These findings indicate that such aerogels have the potential for use as hemostatic agents in wound management.



5.2 Introduction

Hemorrhage from a traumatic injury can cause cardiac arrest and organ failure and can lead to death without a timely and effective solution [1,2]. The natural mechanisms of the body are not able to control a massive hemorrhage, resulting in the requirement for hemostatic intervention [3]. Therefore, using safe and efficient hemostatic materials is essential to save lives [4].

Recently, chitosan (CS)-based aerogels have shown remarkable potential as hemostatic materials [5]. CS is a biodegradable and positively charged polysaccharide that is produced by the deacetylation of chitin, a polymer of N-acetylglucosamine found in the exoskeleton of crustaceans [6]. CS has been used to develop several biomaterials for tissue engineering and drug delivery [1,7] due to its biocompatibility, mucoadhesivity, and impressive range of therapeutic functions such as hemostatic, antimicrobial, antitumor and anti-inflammatory properties [8]. It is believed that the hemostatic property of CS arises from its electrostatic interaction with negatively-charged cell membranes of erythrocytes, leading to erythrocyte agglutination and formation of a hemostatic plug at the site of the injury, thereby preventing blood loss by adhering to tissues and injured vessels and sealing off the wound. However, CS-containing dressings that promote erythrocyte aggregation have been shown to be mechanically unstable [9].

Graphene oxide (GO) is one of the most important graphene derivatives and has high hardness, excellent flexibility, good biocompatibility, and low cost compared to carbon nanotubes; these characteristics make it a practical reinforcement component for new composite materials [10]. In addition, GO aerogels are hemostatic and have great potential for the treatment of traumatic bleeding [2]. Aerogels that contain GO adsorb plasma rapidly and accelerate coagulation; however, the shortcoming of GO sponges is that, in contact with blood, they cannot stimulate hemocytes to promote control of bleeding [6]. GO has been combined with CS at low concentrations to create robust, biodegradable and biocompatible GO-CS nanocomposites [6]. These GO-CS nanocomposites have superior mechanical and controllable drug delivery properties, rendering them suitable for use in drug delivery devices [11]. GO-CS composites have been used as carriers for the delivery of drugs, such as Doxorubicin [12], vitamin B₁₂ [13] and flavonoids [14].

One promising class of phytochemicals is the proanthocyanidins (PAs). PAs are flavanols, a class of polyphenols that have different substitution patterns in the C₆-C₃-C₆ rings and are present in fruits and vegetables. PAs possess several bioactivities that can be used for wound healing, including antiviral, anti-inflammatory and anti-aging effects, among others [15]. Furthermore, it

has been reported that the addition of grape extract to GO-based hemostatic aerogels decreases the coagulation time [16].

In this study, a GO-CS aerogel was developed that was reinforced with grape seed (SD) and skin (SK) extracts for hemostatic use. The influence of the pH on the synthesis and the amount of grape extract on the physical and chemical properties of the aerogels were evaluated, as well as their absorption and coagulation capacities. The release of grape extract from the aerogels and their cytotoxicity in human dermal fibroblasts were also determined.



5.3 Materials and Methods

5.3.1 Production of País grape seed extract

Natural extracts, rich in PAs, were produced from the seeds of cultivar País grapes, following the methodology described by Morales et al. (2014) [17]. The skin and seeds of 200 País grapes were separated manually and extracted individually in Erlenmeyer flasks with a solution of acetone in water (250 mL, 33% v/v) using a New Brunswick G24 gyratory shaker (New Brunswick Scientific Co., Edison, NJ) for 15 h at room temperature in the dark to avoid oxidation. The acetone was removed under reduced pressure and temperature (<35 °C) using a rotary evaporator (Bibby Sterilin Ltd., RE-100B, Stone Staffordshire, England) until 50 mL of extract remained. The liposoluble compounds in the grape extracts were removed by washing with n-hexane (50 mL, three times). Purification of the PAs is described in the supplementary information (SI). The PAs in each extract were characterized by the total phenol content, mean degree of polymerization (mDP) (determined by acid-catalyzed depolymerization -phloroglucinolysis- followed by HPLC detection) [18], average molecular weight (aMW), and molar composition of the extracts. The molecular weight distribution of the extracts was determined by gel permeation chromatography (GPC) [19]. The details of the methodology and results for these assays are presented in Table S1 and Table S2, which are included in Appendix 1 chapter 8.

5.3.2 Preparation of GO-CS aerogels

The GO precursor was synthesized from natural graphite powder using a modified Hummers method [20]. The aerogels were prepared as reported by Yu et al. (2013) with modifications [21]. To begin, a GO solution (0.5 mg mL⁻¹) and 600 mL of Milli-Q water at pH 6 were stirred for 30 minutes. Afterward, a CS solution (1 mg mL⁻¹, pH 2, 30 mL) was added dropwise slowly. The pH of the solution was adjusted to 4 or 10 to modify the solubility of the CS, then the grape seed (SD) and skin extracts (SK) were added (20 mg for 6% w/w or 40 mg for 12% w/w), stirred for 30 min, then allowed to stand for 20 minutes to separate the aqueous phase from the sol-gel phase by precipitation. Then, the supernatant was discarded, and the precipitate was washed three times with Milli-Q water, centrifugated at 3000 x g for 3 minutes and the precipitate was recovered. Finally, the solid was molded in Petri plates and then rapidly frozen in an ultra-freezer at -86 °C (BIOBASE Ultra freezer, China) and freeze-dried (LABCONCO Freeze Dryers,

USA) to obtain the aerogels. Aerogels were also synthesized without the addition of grape seed extracts. The nomenclature in Table 1 indicates the extract concentration and pH for the synthesis.

Table 5-1 Nomenclature for Aerogel samples.

Aerogel components	Extract type	Extract Concentration w/w	pH of the synthesis solution	Name	
Graphene Oxide (GO) and Chitosan (CS)	--	0%	10	GC0pH10	
	Seed (SD)	6%		GC6pH10 SD	
		12%		GC12pH10 SD	
	--	0%	4	GC0pH4	
	Seed (SD)	6%		GC6pH4 SD	
		12%		GC12pH4 SD	
	Skin (SK)	Skin (SK)	6%	10	GC6pH10 SK
			12%		GC12pH10 SK
		Skin (SK)	6%	4	GC6pH4 SK
			12%		GC12pH4 SK

5.3.3 GO-CS aerogels characterization

Fourier transform infrared (FTIR) spectrometry (Perkin Elmer UATR Two FTIR Spectrometer, USA) was used to characterize the GO and the powdered aerogel samples at wavenumbers ranging from 500 to 4000 cm^{-1} . X-Ray Diffraction (XRD) spectra of GO and powdered aerogel samples were measured using an X-ray diffractometer (Bruker AXS, D4 Endeavor) with Cu $K\alpha$ radiation ($\lambda=1.541841 \text{ \AA}$; 2.2 kW) as the reference target, a voltage of 40 kV, and a current of 20 mA. The samples were measured from 2° to 50° (2θ) with steps of 0.02°

and a measuring time of 141 s per step. Raman spectroscopy was used to characterize and compare the GC0pH10 and GC12pH10. The vibrational analysis was acquired through spectroscopy with a 633 nm excitation laser line with a power of 13.3 mW and 1.96 eV. The laser spot was centered on the sample using an Olympus 100x VIS lens and a NUV camera (B/S UV 50/50 + Lens F125 D25). The intensity of the laser remained constant to minimize any damage to the sample. The samples were measured using an object holder at room temperature ($\sim 22^{\circ}\text{C}$); none of the samples were characterized in solution. The uniaxial compression test was carried out by compressing a cylindrical sample (diameter ~ 4.5 cm, height ~ 1 cm) until constant compressive stress of 480 kN on the Instron model 4468 (loading capacity 0.001 \sim 500 kN) at a constant loading speed of 1 mm min^{-1} . The prepared samples for the compression test were freeze-dried in a Petri plate to get a regular cylindrical form. The compressive modulus was calculated in the first linear region (10-70 % stress). Dynamic light scattering analysis was used to determine the surface charge, using the SZ-100 Horiba Scientific (Nano Particle Analyzer), where the samples (1 cm^3 approx.) were dissolved in 30 mL of Mili-Q water, vigorously shaken and then sonicated for 30 minutes before they were measured. Scanning Electron Microscopy (SEM) was performed using a JEOL JSM-6380LV microscope at 10 kV. The lyophilized samples were coated using a gold sputter coater, and the surfaces were observed with different resolutions to compare the internal structures. The samples with blood were exposed to blood for 10 minutes, and glutaraldehyde was added to immobilize the cells, then the samples were dried with acetone and supercritical dried to be coated later. Also, the images were processed with the “Digital Gatan Microscopy 3.0” software for the distribution of the pore size

5.3.4 Absorption kinetics

The absorption kinetics of water and Phosphate Buffered Saline (PBS) were measured submerging 1 cm^3 of aerogel sample in 10 mL of Mili-Q water or PBS on a watch glass, then the excess liquid was extracted from the watch glass at different times (5, 10, 15, 30, 60, 300, 900 and 2700 seconds). The mass of the sample before (S_0) and after (S_w) of every immersion was measured, the ratio was calculated as:

$$\text{Absorption Ratio} = \frac{(S_w - S_0)}{S_0} \quad \text{Eq.(1)}$$

5.3.5 Coagulation assay

To evaluate the coagulation capacity of the aerogels, an *in vitro* coagulation time test was performed, which allowed the comparison of coagulation efficiency between the samples and the control, using the reported methodologies [24]–[26]. The aerogels were synthesized and freeze-dried in a 24-well plate to get a regular volume. In a 12-well plate, a total volume of 50 μL of fresh blood (from a volunteer) was dropped directly into each test group, including a blank and a sterile gauze sponge. Each group interacted for 30, 60, 120, and 240 s, at room temperature. After each time, 5 ml of Milli-Q[®] water was added slowly onto the sample to stop the coagulation process and quantify the uncoagulated blood from the supernatant. The hemoglobin content in the supernatant of each sample was estimated by measuring the absorption with a UV-VIS, using a Spectroquant[®] Prove 600 spectrometer (Merck KGaA, Germany) at 540 nm. As a reference value, the absorption of 50 μL fresh blood in 10 ml Milli-Q water (the blank) was measured. As a blood clotting index, the hemoglobin content in the resulting solution was quantified for each group at each time interval, using the following equation: Hemoglobin Absorbance = $I_s/I_r \times 100\%$, where I_s is the absorbance of the resulting sample, and I_r is the absorbance of the reference value. This experiment was repeated 3 times with the blood from the same individual under the same conditions.

In addition to the hemoglobin absorbance, a total blood counter (TBC) was used to distinguish between the absorbed red blood cells (RBC) and the absorbed white blood cells (WBC). In a 12-well plate, a total volume of 300 μL of blood (contained in a test tube Vacutainer[™] with EDTA) was dropped directly onto each test group, including a blank. Each group was allowed to interact for 30, 60, 120, and 240 s, at room temperature. After each time, 5 mL of PBS solution was added slowly onto the sample to stop the absorption process and quantify the diluted blood samples from the supernatant. From the supernatant is recovered 1mL of it, in an Eppendorf tube, and then a TBC is made using the Sysmex XS-1000i[™] (Sysmex, Japan).

5.3.6 Extract release profile

The kinetics of extract release from the aerogels were determined using the initial amount of extract incorporated (Table 1) and similar sizes ($\sim 2 \text{ cm}^3$). PBS (at 37 °C and pH 7.4) was used to simulate the blood plasma conditions and the exudate from a wound. The aerogels were weighed

and then immersed in 250 mL of PBS in a thermostatic bath (Thermostat Fried Electric TEPS-1 N° Series 1881). Samples (1 mL) of the solution were removed at 5, 10, 15, 30, 60, 300 and 900 seconds and the concentrations of the released extracts were determined. The samples that were removed were replaced with PBS at 37°C. The difference in the extract concentrations between the original PBS solution and the supernatant (containing the dissolved extract) was determined using a total phenol assay using the Folin-Ciocalteu reagent in a Spectroquant® Prove 600 spectrometer (Merck KGaA, Germany) at a wavelength of 765 nm. The amount of extract released from the aerogel, $Q_d(t_i)$, at time t_i was calculated using the following equation: $Q_d(t_i) = q_d(t_i)/m$, where $q_d(t_i)$ is the content of total phenols in the medium (mg eq gallic acid/mg extract) and m is the mass of aerogel (mg). The total phenol content in the samples that were extracted from the release medium was measured by spectrophotometry using the Folin-Ciocalteu reagent [25], which imparts a color to the solution in the presence of phenols. Thus, the concentrations of the phenols were determined and expressed as grams of gallic acid equivalents (See the determination of the total concentration of phenols in the S.I.). The relative amount of extract released from the aerogels was expressed as the content of total phenols in the medium at time t divided by the content of phenols in the medium at infinite time.

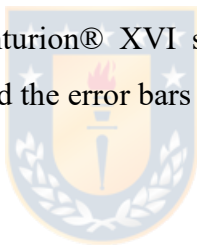
5.3.7 Cytotoxicity assay

Cytotoxicity was determined using the 3-(4,5-dimethylthiazol-2-yl)-2,5-diphenyltetrazolium bromide (MTT) assay. Human dermal fibroblast cells were used to evaluate the *in vitro* cytotoxicity of the materials and the synthesized aerogels. These experiments were conducted using a cell density of 10^4 cells/mL. First, 1 mL of DMEM medium was added to 10 mg of aerogel samples and also to the individual materials (GO, CS and Extracts) to promote full contact. After 24 hours of incubation at 37°C, the supernatant was recovered and mixed with 2% (v/v) fetal bovine serum (FBS), 1% (v/v) antibiotics (100 units/mL of penicillin and 100 units/mL of streptomycin) and 1% of amphotericin to avoid the proliferation of fungi in the cells. DMEM medium was used as a positive control. The supernatant from each sample was added to the cells and incubated for 48 h at 37°C under humidified air with 5% (v/v) CO₂. At the end of the incubations, the supernatants were removed, and the cells were washed with PBS, pH 7.4. Then, 100 µL of fresh DMEM medium was added to the cells and 5 mg/mL MTT solution was added for

the determination of cell viability. The plates were incubated for 4 h at 37°C with CO₂, then 85 µL of medium was removed and 50 µL of dimethyl sulfoxide (DMSO) was added to the wells. After 10 min, the supernatant was removed by aspiration, and the formazan crystals were dissolved in DMSO (100 µL per well), followed by shaking for 5 min. The absorbance was determined using a microplate reader (Spectra Plus, TECAN, USA) at a wavelength of 570 nm. The cell viability (%), relative to control cells, was calculated from $A_{\text{test}}/(A_{\text{control}}) \times 100\%$, where A_{test} and A_{control} are the absorbance values of the wells (with the aerogels) and control wells (without the aerogels), respectively

5.3.8 Statistical analysis

The spectrophotometric determinations were performed in duplicate, and OriginPro8® software was used to analyze the data. All experiments were performed in triplicate, and the results are expressed as arithmetic means and standard deviations (Mean ± Standard Deviation). ANOVA was performed using Statgraphics Centurion® XVI software, with a statistically significant average of $p \leq 0.05$. The mean values and the error bars are reported in each figure.



5.4 Results and Discussion

5.4.1 Formation of GO-CS aerogels

The FTIR spectra for GO and GC0pH10 are shown in *Figure 5-1* from 500-4000 cm^{-1} . Both spectra had a broad peak at 3300 cm^{-1} corresponding to $-\text{OH}$ groups and residual water in the samples. The peak at 1733 cm^{-1} corresponds to $\text{C}=\text{O}$ bonds in carboxylic groups from the GO layers that are present in both samples. The peak at 1628 cm^{-1} corresponds to $\text{C}=\text{O}$ bonds in carbonyl groups [26] and is intensified due to the addition of CS, which increases the concentration of carbonyl groups. In addition, the peak at 1235 cm^{-1} that appears in the aerogel spectrum indicates the presence of a $\text{C}-\text{N}$ bond (stretching) from the amine group in the CS structure [7]. The peak at 972 cm^{-1} can be attributed to $\text{C}-\text{O}$ bonds which are present in all of the aerogels.

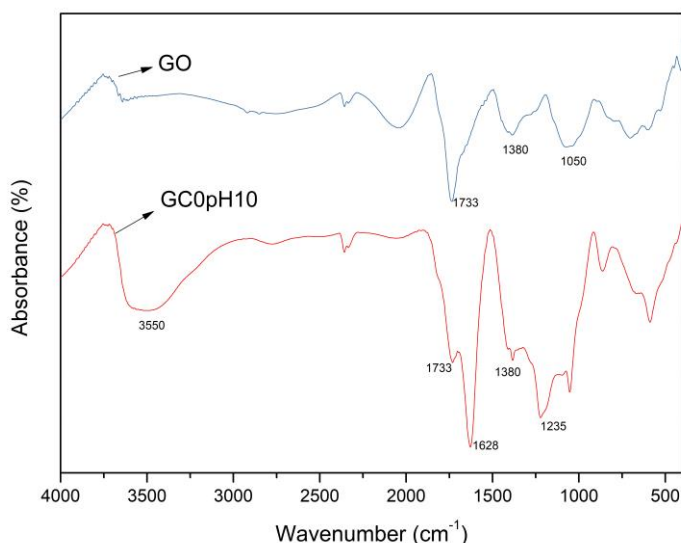


Figure 5-1 FTIR spectra of graphene oxide (GO) and not loaded aerogels synthesized under basic conditions (GC0pH10).

The XRD spectra for GO and GC0pH10 aerogels in *Figure 5-2* show a deformation of the peak for the GO sample at 10.12° [27], which is weaker and broader at 9.7° in GC0pH10, possibly due to exfoliation of the GO during the formation of the aerogel. The d-spacing was calculated from the Bragg equation and yielded values of 0.68 nm for GO and 3.49 nm for the aerogel, indicating successful exfoliation of the GO structure and thereby producing more space between the GO layers; as a consequence, CS chains were interconnected to create the 3D structure of the

aerogel [6]. In the XRD analysis, there is no indication of CS in the aerogel diffractogram, which may be due to its low content or because it has dissolved to form amorphous nanofibers and lost its crystallinity [28]

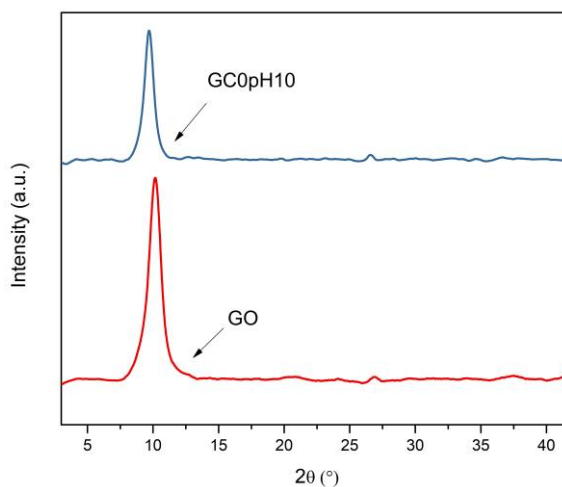


Figure 5-2 XRD patterns of graphene oxide (GO) and not loaded aerogels synthesized under basic conditions (GC0pH10).

The Raman spectrum of GC0pH10 (Figure 5-3) shows typical peaks for GO; the D band ($\sim 1339\text{ cm}^{-1}$) corresponding to carbon rings with sp^3 conjugation adjacent to a graphene edge or a defect [29]; the G band ($\sim 1590\text{ cm}^{-1}$), which is associated with plane vibration of carbon atoms with sp^2 conjugation [30]; and the 2D band ($\sim 2700\text{ cm}^{-1}$), which is associated with a disordered effect on the morphology of the samples [31]. The spectrum exhibits noise between 2000 and 3000 cm^{-1} due to the presence of CS [32]. The resulting ratio $I_D/I_G=3.57$ indicates the presence of defects on the GO surface due to the effect on sonication and stirring processes during aerogel synthesis.

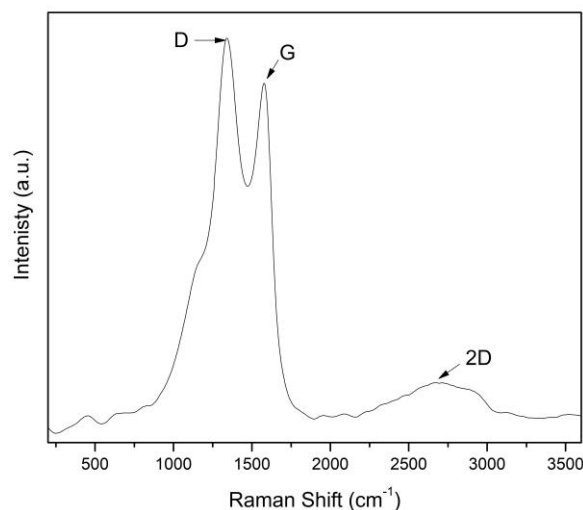


Figure 5-3 Raman spectrum of not loaded aerogel synthesized under basic conditions (GC0pH10).

5.4.2 Effects of addition of seed (SD) and skin (SK) extracts on aerogels.

Characterization of grape SK and SD extracts (see SI) demonstrated that the PAs molecules from SD extracts have a smaller molecular size than those from SK extracts, with an average molecular weight of 3019 ± 87 g/mol for SD and 7565 ± 221 g/mol for SK extracts. The structural compositions differed significantly since the skin extracts have no terminal (-)-epicatechin (EC) or epigallocatechin (ECG); alternatively, (-)-epicatechin-phloroglucinol (EGC-P) was not detected in the seed extract adducts. (+)-Catechins (C) were present in both terminal and extension subunit extracts. The total phenol content (measured as g equivalents gallic acid/g extract for 1 g/L solutions) was higher in the SD extracts (0.73 ± 0.47) than in the SK extracts (0.62 ± 0.15). This characterization of the extracts indicated differences between the compositions of the extracts, where a higher presence of the ECG monomer in the SD extract polymeric chain was observed, which was 6 times higher in extension subunits. Also, SK extracts had only C as a terminal subunit, as opposed to SD extracts which had C, EC, and ECG as terminal subunits of shorter polymeric chains. These variances could influence the wound healing potential [16] and the absorption of extracts by the aerogels.

During the synthesis of the aerogels, when the addition of extracts was made to the GO solution, we assumed complete adsorption of the grape extract (abundant in flavonoids) onto the GO surface.

This effect was reported by Xu et al. (2017), who used GO cotton fibers to adsorb flavonoids from crude extracts for the purification of polyphenols [33].

The Raman spectrum for an aerogel loaded with 12% seed extract (GC12pH10 SD) was compared with a not loaded (GC0pH10) aerogel at the same pH (*Figure 5-4*). The results show a shift of the D (-3 cm^{-1}) and G (-16 cm^{-1}) bands, and also an increase in the ratios of intensities to $I_D/I_G=4.33$. This result represents a slight softening of the bonds between the GO interlayers, increasing the calculated layer's thickness and the occurrence of exposed defects in the GO [34] with the addition of SD extract in the structure of the aerogel.

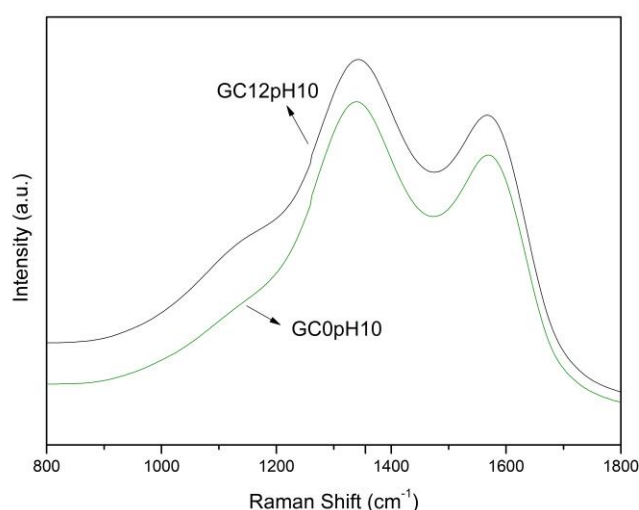


Figure 5-4 Raman spectra comparison between loaded aerogel with 12% of seed extract (GC12pH10 SD) and not loaded aerogel (GC0pH10) both at pH 10.

The deconvolution of the D and G bands from the GC0pH10 and GC12pH10 SD aerogels is presented in *Figures 5-5* and *Figure 5-6*, respectively. The D* band represents the presence of amorphous carbon and sp^3 carbon atoms [35], the D** band is due to the vibrations of C=C and C-H bonds in carbon compounds, with a single hydrogen-bonded carbon [36]. The D' band shows the presence of defects on the graphene layer plane [37], and the results indicate an increase of 3.3-fold in the signal of the D' band when the aerogel is loaded with extracts, demonstrating that the GO structure was modified by the incorporation of grape SD in their surface vibrational states, especially the defects of the GO layers that were activated [38] [36]. The grape extract present in the structure promoted separation of the GO sheets, leading to an increase in the interlayer space

in the 12% SD extract-loaded basic aerogel (GC12pH10 SD), possibly due to the positively charged zones of CS and the negatively charged grape extract promoting electrostatic repulsion between the oxygenated groups of the GO layer plane surface [39]. Also, by deconvolution, no significant variation was observed (<10%) of the D* and D** bands compared with GC0pH10. The presence of these bands could be due to the existence of nano-graphite or finite-sized crystallites [34] of residual graphite from the synthesis of GO, which are the same in both aerogels.

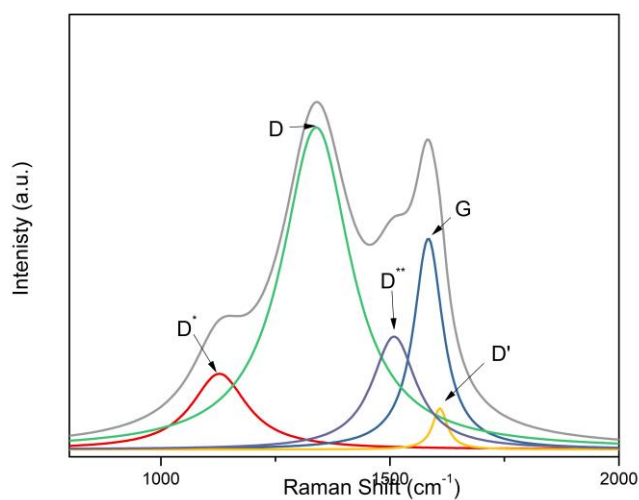


Figure 5-5 Deconvolution of Raman D and G peaks for not loaded aerogel synthesized under basic conditions (GC0pH10).

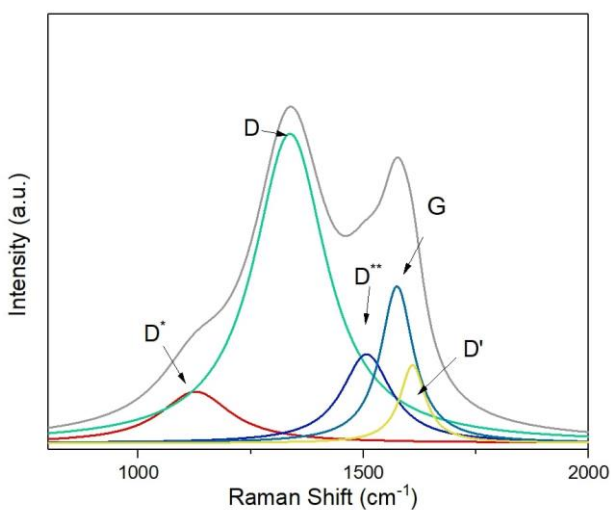


Figure 5-6 Deconvolution of Raman D and G peaks for aerogels loaded with 12% SD extracts synthesized under basic conditions (GC12pH10 SD).

5.4.3. Characterization of GO-CS aerogels

The elastic modulus (E) values for aerogels synthesized at different pH values and with and without loaded extracts are shown in *Figure 5-7*. Increasing the synthesis pH increased the value of E, as CS was less soluble in alkaline compared to acidic media [8]. This effect increased the rigidity of the aerogels when the pH increased. Furthermore, the addition of SD extracts also increased the E for the aerogels, in proportion with the mass of extract added ($p < 0.05$).

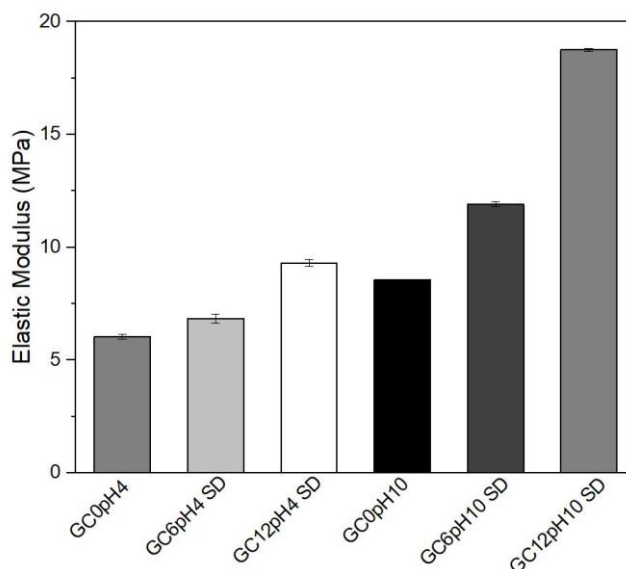


Figure 5-7 Elastic modulus calculated from the compression tests of SD extract loaded aerogel samples.

The surface charge of the aerogels exhibited negative values for both pH conditions (Table 2), even with the presence of positive ions (in the case of acidic media). The superficial negative charge of the aerogel increases as the amount of loaded extract increases, producing aerogels with higher charge for SD extract-loaded compared to SK-loaded aerogels. The highly negative charged surfaces can increase the adsorption of proteins and thereby initiate the coagulation cascade [40], increase the platelet activation levels and promote the release of intracellular Ca^{2+} [5], thus promoting the potential hemostatic use of the aerogel. In addition, CS promotes electrostatic stabilization, allowing the structure of the aerogel to form and simultaneously support immobilization of the grape extract on the GO, since CS can increase the efficiency of absorption of the components to GO sheets [6].

The isoelectric points of the raw materials (GO and CS) were pH 2 for GO and pH 5 for CS, which are close to the acidic pH used in this study. The acidic media protonates the surface of the samples, making CS chains more soluble due to the presence of free amino groups and resulting

in an untangled structure [7]. In addition, the negatively charged GO sheets attract positively charged ions and render the overall charge close to neutral. On the other hand, in neutral and alkaline pH media, the CS chains agglomerate and separate from the water, producing a viscous precipitate. Thus, the aerogels synthesized in alkaline media were more rigid than those synthesized in acidic media, as shown in *Figure 5-7*.

The changes in the superficial charges played a central role in the interaction between these materials and the blood coagulation system. Charged surfaces enhance the Vroman effect, promoting protein adsorption that can immobilize fibrinogen or fibrin directly, and the activation of platelets can promote rapid coagulation [40].

Table 2 Surface charge of aerogels.

Sample	Surface charge (mV)
GC0pH10	-5.5 ± 0.1
GC6pH10 SD	-43.0 ± 1.6
GC12pH10 SD	-55.7 ± 0.2
GC6pH10 SK	-38.4 ± 1.7
GC12pH10 SK	-39.2 ± 0.8
GC0pH4	-1.5 ± 0.1
GC6pH4 SD	-52.0 ± 4.1
GC12pH4 SD	-60.9 ± 0.2

The SEM images showed that the pH conditions affected the rugosity of the samples; as the pH increased, an enhancement in the wrinkles was observed (*Figure 5-8a* at pH 4 vs *Figure 5-8d* pH 10). This effect is caused by the decreasing solubility of CS in basic media and the presence of insolubilized aggregates of CS in the matrix of aerogels. The incorporation of the extracts also affects the macrostructure (*Figure 5-8a* vs *5-8b* and *Figure 5-8d* vs *5-8e*), and the increase from 6% to 12% of SD extract concentrations on the aerogels made more intricate and heterogeneous structures, compared with the aerogels synthesized without the extracts.

SEM images of aerogels obtained under alkaline conditions without extracts (GC0pH10, *Figure 5-8d*) and aerogels loaded with 12% SD extracts (GC12pH10 SD, *Figure 5-8f*) and 12%

SK extract loaded aerogels (GC12pH10 SK, *Figure 8-1* on Appendix B) at the same pH were compared, and their pore sizes were determined by analysis of the images. The pore size was 10.2-13 μm for aerogels without extract incorporated (GC0pH10), 2.2-7.2 μm for the aerogels with 12% SD added (GC12pH10 SD), and between 3.8-5.6 μm for 12% of the SK extract loaded aerogels (GC12pH10 SK). This behavior suggested a reduction in the pore size of the aerogels and an increase of the crosslinking density with the incorporation of grape extracts in the aerogels and increasing pH, which gives higher rigidity to these aerogels, in accordance with the elastic modulus values presented above.

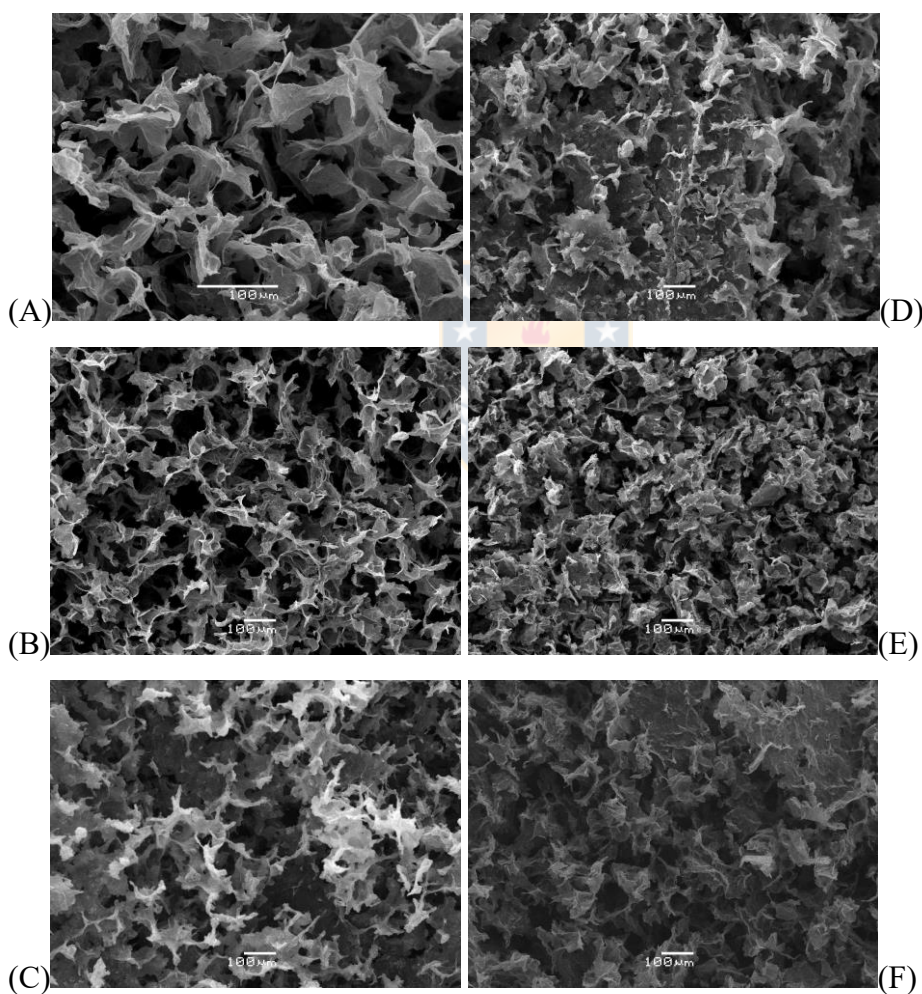


Figure 5-8 SEM images of aerogels under acidic conditions, GC0pH4 (A); aerogel loaded with 6% SD extract, GC6pH4 SD (B); aerogel loaded with 12% SD extract, GC12pH4 SD (C); aerogel under alkaline conditions, GC0pH10 (D); aerogel loaded with 6% SD extract, GC6pH10 SD (E); and aerogel loaded with 12% SD extract, GC12pH10 SD (F).

5.4.4 Absorption capacities of the aerogels

Figure 5-9 shows water absorption (dotted lines) for not loaded acid and alkaline aerogels (GC0pH4 and GC0pH10, respectively). Rapid absorption is observed in the first 60 seconds that reached a plateau value of ~55 g water/g aerogel for GC0pH10 and ~48 g water/g aerogel for GC0pH4 at 900 seconds, demonstrating an increased absorption capacity for the aerogels synthesized under basic condition.

PBS absorption (solid lines) reached a stable value after 60 seconds for all the samples. However, the not loaded alkaline aerogel (GC0pH10) had a higher absorption capacity of ~70 g PBS/g aerogel compared to the acidic aerogel (GC0pH4) with ~26 g PBS/g aerogel. This difference may be attributed to a higher capillarity in the basic structure of the aerogel. Ramesha et al. (2011) used GO and reduced GO to absorb charged dye compounds and observed a minimal removal efficiency of orange G's (negatively charged dye agent) close to pH=4 [41], demonstrating a pH dependence of ionic absorption capacity similar to our results with PBS. With alkaline aerogels, the presence of insolubilized CS aggregates produced a heterogeneous matrix (shown in the SEM images) that can display CS hemostatic effects similar to the mucoadhesive mechanism that may involve tissue adherence, hemocyte binding, and platelet activation [6]. In addition, Jayakumar et al. (2011) [42] reported that CS accelerates wound contraction and healing, preventing infections, with greater oxygen permeability. Zhang et al. (2019) [5], reported a water absorption capacity of 48 g/g for synthetic N-alkylated CS/graphene aerogels; a similar value compared with the aerogels described here and concluded that the N-alkylated CS/graphene aerogels shorten the reaction time for coagulation and accelerates the formation of fibrin. They also demonstrated that fibrins are entangled with activated erythrocytes and platelets through both coagulation pathways, intrinsic and extrinsic; thus, blood clots are formed successfully on the matrix of aerogels and on wounds [5]. These coagulation pathways could occur in our materials as well. Although their reported material is positively charged, in contrast to our aerogels, contact activation in plasma is also triggered and propagated on hydrophobic and positively charged surfaces, although at a much slower rate than on negative surfaces [40].

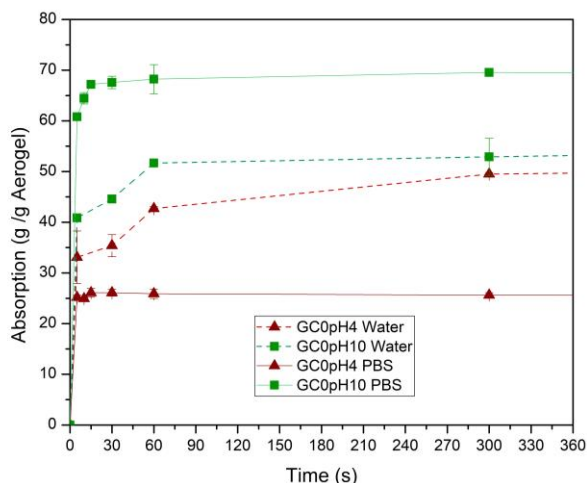


Figure 5-9 Absorption of water (dotted lines) and PBS (straight lines) on aerogels synthesized under acidic conditions GC0pH4 (red) and alkaline conditions GC0pH10 (green) not loaded with extracts.

3.5 Coagulation capacity

The capacity of the aerogels for human blood coagulation, measured as hemoglobin absorbance at 540 nm, is presented in Figure 5-10. The gauze (commonly used in hemorrhage treatments) produced no evident coagulation effect during the experiment. The aerogels had almost a total blood absorption after 30 seconds in contact, reaching 95% of the absorption maximum. There were no differences in blood absorption between 30 and 120 seconds for the aerogels ($p > 0.05$).

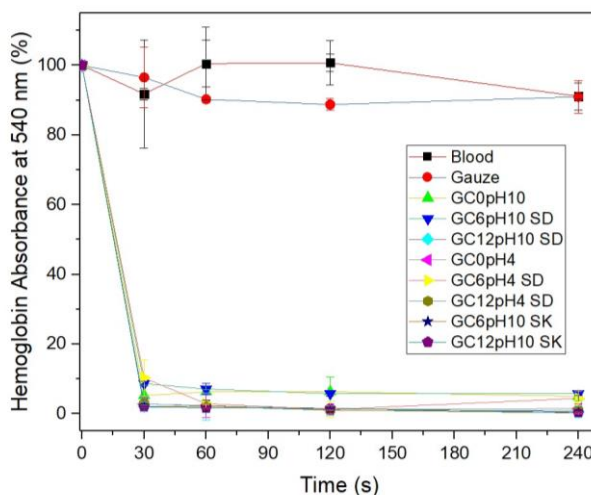


Figure 5-10 Hemoglobin UV absorbance of supernatants for blood absorption tests with aerogels.

Table 5-2 shows the total blood count (TBC) in supernatants after blood absorption to aerogels. The values present a rapid absorption of blood into the aerogels without added extracts. The acidic aerogels reached total absorption within the first 30 seconds and the alkaline aerogels within 60 seconds. This is a favorable result for our purpose of blood immobilization since motionless blood tends to coagulate [43]. Also, no selectivity for RBC or WBC absorption was observed with regard to the pH difference used in the synthesis. Instead, blood was absorbed as a whole, and then the processes of coagulation was likely initiated by the Vroman effect [40]. The structure of acidic aerogels collapsed due to capillarity forces, and then these materials dissolved in the media, which can be a problem for use on irritated skin [44].

Table 5-2 Total Blood Count results of supernatant after blood absorption in aerogels.

	Time (s)	0	30	60	120	240
RBC	GC0pH4	100%	0%	0%	0%	0%
	GC0pH10	100%	42.4% \pm 2.9%	0%	0%	0%
WBC	GC0pH4	100%	0%	0%	0%	0%
	GC0pH10	100%	42.0% \pm 1.6%	0%	0%	0%
HGB	GC0pH4	100%	0% \pm 5%	0%	0%	0%
	GC0pH10	100%	43.0% \pm 5.8%	0%	0%	0%

* red blood cells (RBC), white blood cells (WBC), hemoglobin (HGB)

The surface of the aerogels after blood absorption was analyzed by SEM (*Figure 5-11*). In *Fig 5-11*, the presence of RBCs and WBCs was observed in the 6% SD extract-loaded basic aerogel (GC6pH10 SD). An increase in the 12% SD extract loaded on basic aerogel sample (GC12pH10 SD, *Fig 5-11B*) promotes rugosity formation on the surface, which can be caused by fibrin production after the activation of fibrinogen by the negatively charged surface [40]. Additionally, the amount of RBCs and WBCs that accumulated between the aerogel layers was higher in the 12% loaded basic aerogel (GC12pH10 SK) (*Figure 5-11 D*) compared to aerogels with 6% SK loading (*Figure 5-11 A*). Finally, a visible difference in the pore structure was also observed between the SD (*Figure 5-11 A and B*) and SK extract loaded aerogels (*Figure 5-11 C and D*), as was observed in the SEM images in *Figure 4*. Some crystallization is shown in *Figure 5-11 C*, possibly due to the glutaraldehyde that was used in the sample preparation.

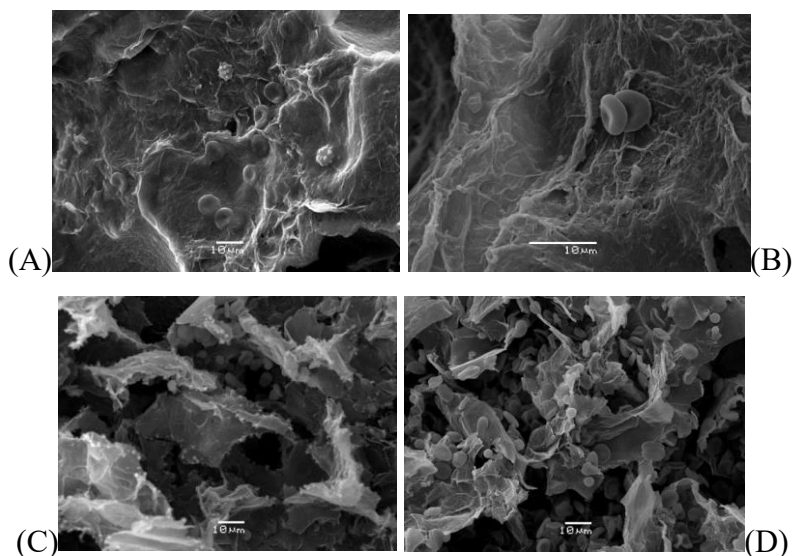


Figure 5-11 SEM images of absorbed blood aerogels synthesized under basic conditions loaded with 6% SD extracts. (A), GC6pH10 SD; (B), GC12pH10 SD; (C), GC6pH10 SK; and (D), GC12pH10 SK aerogels.

5.4.5 Aerogels and media interaction

Figure 5-12 presents the release profiles for SD and SK extracts in PBS (pH 7.4, 37.5 °C). A general slow release was observed for the samples up to 30 minutes. After 60 minutes, acid and basic aerogels with 6% SD loaded grape extracts showed no significant differences in their profiles (GC6pH4 SD and GC6pH10 SD aerogels), reaching a cumulative release of 3% at 720 minutes, and the 6% SK loaded aerogel (GC6pH10 SK) achieved the lowest cumulative release of 2.8% at this time. The 12% SD extract loaded basic aerogel (GC12pH10 SD) had a final cumulative release of approximately 14%, and the loaded acidic aerogel (GC12pH4 SD) reached 24% of the cumulative release at 720 minutes. At the same time, the GC12pH10 SK reached the second-highest value of 23.8%. This highest release of acidic samples could be caused by the dissolution of aerogel in the media, reducing mass transfer limitations, which may explain the increase in the release velocity. Similarly, mass transfer limitations can explain the slower release with the SK loaded aerogels, which only after 720 minutes presented a significant release due to the larger molecule with a high average molecular weight (aMW). Another effect that may explain higher release in acidic aerogels is that the extracts are degraded and oxidized under basic conditions [45]. Under these conditions for synthesis, the SD extract was more affected due to its lower aMW (see Appendix B). In addition, the integrity of this aerogel was damaged when the experiments were

performed and dissolved in media. Therefore, we considered that the alkaline aerogels were more suitable as hemostatic agents due to their rigidity, porosity, superficial charge, PBS and blood absorption capacities, and their resistance after absorption of the physiological media.

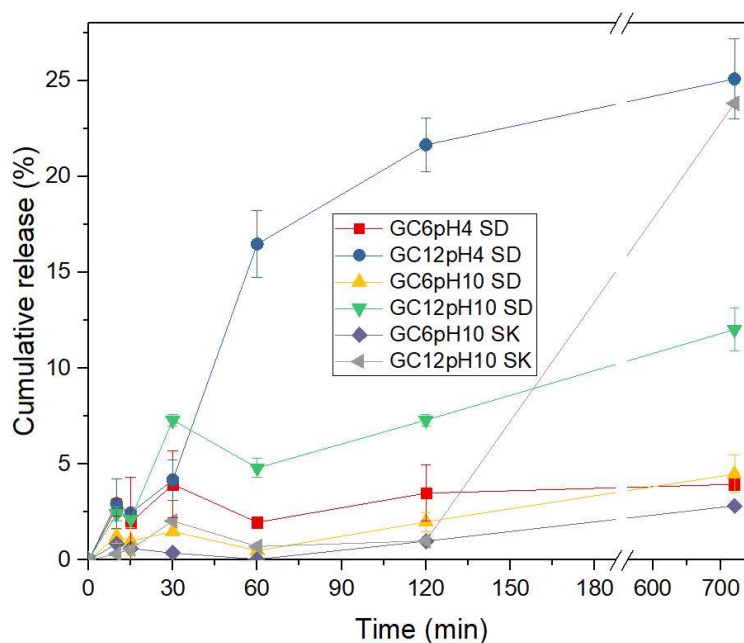


Figure 5-12 Release profiles of extracts from aerogels in PBS (pH 7.4, 37 °C)

3.7 Cytotoxicity assay

Cytotoxicity assays were conducted using the aerogel exudate media after 24 hours of incubation with human dermal fibroblast cells to modulate the exudate effect in wounds after blood absorption (Figure 5-13). The SD extract showed lower viability (81%) compared with the SK extract (94.2%). The CS sample enabled cell proliferation to reach 116 %, This behavior has been described in the literature [46] and demonstrates the compatibility of this biopolymer [8]. The GO sample had no apparent cytotoxic effect, producing nearly 96% cell viability. Using the not loaded aerogel (GC0pH10) the cell viability was 72.8%. The SD extract loaded aerogels produced no significant differences between them ($p\text{-value} > 0.05$), yielding 65.5% and 66% in the GC6pH10 SD and GC12pH10 SD samples, respectively. The aerogels loaded with grape 6% SK extract (GC6pH10 SK) resulted in 91.8%, and the 12% SD (GC12pH10 SK) yielded 88% cell viability. It is worth mentioning that the cytotoxicity was dependent on the type of extract loaded, increasing the viability from 65% with SD to 93% with SK.

The principal difference between SD and SK extracts is the nature of the monomers in their structures (shown in Appendix B). Different cytotoxic effects of polyphenol subunits were reported in the work of Babich et al. [43], who compared the *in vitro* cytotoxicity of C, EC, EGC and ECG in normal cells from the human oral cavity (HGF-2 fibroblasts cells). Their results showed that after a 3 day exposure to the cells, ECG was highly cytotoxic with a cytotoxicity midpoint (NR₅₀) of $100 \pm 9.5 \mu\text{M}$; however, C, EC and EGC were slightly cytotoxic with an NR₅₀ > 500 μM [43]. Considering that the SD extract has 8 times more ECG than SK in their extension and terminal subunits, the toxicity of ECG may explain differences in extract cell viability of exudates from loaded aerogels. Moreover, in the work of Hashimoto et al. (1999), it was determined that the number of tea polyphenols incorporated into lipid bilayers was in the order ECG > EC > EGC [47]. This effect could enhance the toxic effect of the SD extract compared to the SK extract. Furthermore, it has been reported that the incorporation of compounds into cells decreases as procyanidin oligomerization increases [45], generating less capacity for SK extracts to penetrate the cell membrane, which produced a long chain flavanol structure compared to the SD extract.

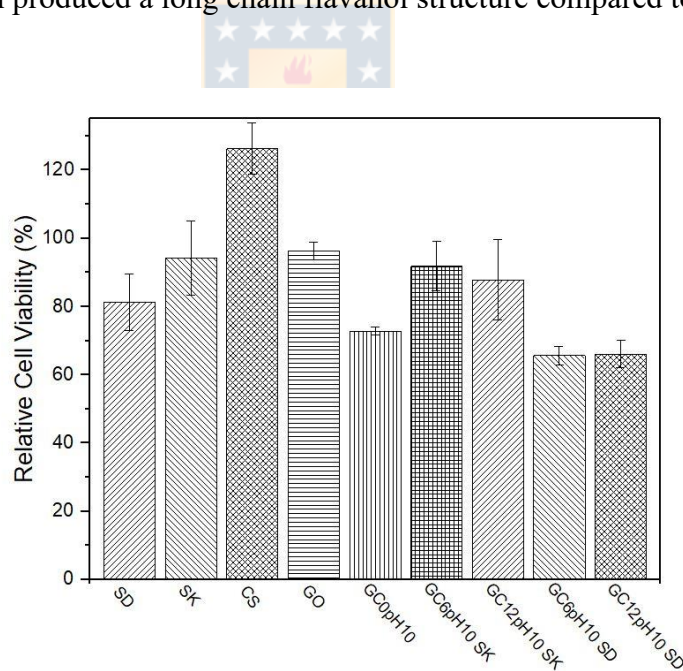


Figure 5-13 Cell viability of human dermal fibroblast cells after 24 h of incubation with exudate from aerogel samples and GO, CS, and extracts.

5.5 Conclusion

In this study, GO-CS aerogels loaded with SD and SK extracts were developed and demonstrated to have the potential to be effective hemostatic agents and also to be useful in a drug delivery platform. Coupling the negative superficial charge of aerogels with their high crosslink density gives them the ability to absorb physical media, mainly blood, rapidly over time. These properties are relevant and pertinent for hemostasis, causing a localized aggregation of red blood cells and platelets while retarding blood coagulation. The addition of grape seed and skin extracts with high contents of flavanols enhanced the roughness and stiffness structures of the aerosols, rendering them suitable for blood absorption. The aerogels have the ability to promote the accumulation of red blood cells through electrostatic interactions. The loaded aerogels showed slight cytotoxicity; however, the use of SK instead of SD increased the cell viability, making them acceptable for hemostatic applications. Additional studies are necessary to completely understand the mechanisms by which coagulation is promoted.



5.6 References

- [1] T.S. Yan, F. Cheng, X.J. Wei, Y.D. Huang, J.M. He, Biodegradable collagen sponge reinforced with chitosan/calcium pyrophosphate nanoflowers for rapid hemostasis, *Carbohydrate Polymers*. 170 (2017) 271–280. <https://doi.org/10.1016/j.carbpol.2017.04.080>.
- [2] Y.P. Liang, C.C. Xu, G.F. Li, T.C. Liu, J.F. Liang, X. Wang, Graphene-kaolin composite sponge for rapid and riskless hemostasis, *Colloids and Surfaces B-Biointerfaces*. 169 (2018) 168–175. <https://doi.org/10.1016/j.colsurfb.2018.05.016>.
- [3] K. Irita, Risk and crisis management in intraoperative hemorrhage: Human factors in hemorrhagic critical events, *Korean Journal of Anesthesiology*. 60 (2011) 151.
- [4] L.W. Chan, C.H. Kim, X. Wang, S.H. Pun, N.J. White, T.H. Kim, PolySTAT-modified chitosan gauzes for improved hemostasis in external hemorrhage, *Acta Biomaterialia*. 31 (2016) 178–185. <https://doi.org/10.1016/j.actbio.2015.11.017>.
- [5] Y. Zhang, J. Guan, J. Wu, S. Ding, J. Yang, J. Zhang, A. Dong, L. Deng, N-alkylated chitosan/graphene oxide porous sponge for rapid and effective hemostasis in emergency situations, *Carbohydrate Polymers*. 219 (2019) 405–413.
- [6] S. Gooneh-Farahani, M.R. Naimi-Jamal, S.M. Naghib, Stimuli-responsive graphene-incorporated multifunctional chitosan for drug delivery applications: a review, *Expert Opinion on Drug Delivery*. 16 (2019) 79–99.
- [7] H. Bao, Y. Pan, Y. Ping, N.G. Sahoo, T. Wu, L. Li, J. Li, L.H. Gan, Chitosan-functionalized graphene oxide as a nanocarrier for drug and gene delivery, *Small*. 7 (2011) 1569–1578. <https://doi.org/10/c7k2nc>.
- [8] A. Baranwal, A. Kumar, A. Priyadarshini, G.S. Oggu, I. Bhatnagar, A. Srivastava, P. Chandra, Chitosan: An undisputed bio-fabrication material for tissue engineering and bio-sensing applications, *International Journal of Biological Macromolecules*. (2018). <https://doi.org/10/gdchxn>.
- [9] R. Gu, W. Sun, H. Zhou, Z. Wu, Z. Meng, X. Zhu, Q. Tang, J. Dong, G. Dou, The performance of a fly-larva shell-derived chitosan sponge as an absorbable surgical hemostatic agent, *Biomaterials*. 31 (2010) 1270–7. <https://doi.org/10.1016/j.biomaterials.2009.10.023>.
- [10] H.Y. Mao, S. Laurent, W. Chen, O. Akhavan, M. Imani, A.A. Ashkarran, M. Mahmoudi, Graphene: Promises, Facts, Opportunities, and Challenges in Nanomedicine, *Chemical Reviews*. 113 (2013) 3407–3424. <https://doi.org/10.1021/cr300335p>.

- [11] R. Justin, B. Chen, Characterisation and drug release performance of biodegradable chitosan–graphene oxide nanocomposites, *Carbohydrate Polymers*. 103 (2014) 70–80.
- [12] H. Wen, C. Dong, H. Dong, A. Shen, W. Xia, X. Cai, Y. Song, X. Li, Y. Li, D. Shi, Engineered redox-responsive PEG detachment mechanism in PEGylated nano-graphene oxide for intracellular drug delivery, *Small (Weinheim an Der Bergstrasse, Germany)*. 8 (2012) 760–9. <https://doi.org/10.1002/sml.201101613>.
- [13] H. Bai, C. Li, X. Wang, G. Shi, A pH-sensitive graphene oxide composite hydrogel, *Chemical Communications (Cambridge, England)*. 46 (2010) 2376–8. <https://doi.org/10.1039/c000051e>.
- [14] N. Rahmanian, H. Hamishehkar, J.E. Dolatabadi, N. Arsalani, Nano graphene oxide: a novel carrier for oral delivery of flavonoids, *Colloids and Surfaces. B, Biointerfaces*. 123 (2014) 331–8. <https://doi.org/10.1016/j.colsurfb.2014.09.036>.
- [15] P.M. Aron, J.A. Kennedy, Flavan-3-ols: Nature, occurrence and biological activity, *Molecular Nutrition & Food Research*. 52 (2008) 79–104. <https://doi.org/10.1002/mnfr.200700137>.
- [16] C. Mellado, T. Figueroa, R. Báez, R. Castillo, M. Melendrez, B. Schulz, K. Fernández, Development of Graphene Oxide Composite Aerogel with Proanthocyanidins with Hemostatic Properties As a Delivery System, *ACS Applied Materials & Interfaces*. 10 (2018) 7717–7729. <https://doi.org/10.1021/acsami.7b16084>.
- [17] C. Morales, M. Roeckel, K. Fernández, Microscopic modeling of país grape seed extract absorption in the small intestine, *AAPS PharmSciTech*. 15 (2014) 103–110.
- [18] J.A. Kennedy, G.P. Jones, Analysis of proanthocyanidin cleavage products following acid-catalysis in the presence of excess phloroglucinol, *Journal of Agricultural and Food Chemistry*. 49 (2001) 1740–1746.
- [19] V.M. Williams, L.J. Porter, R.W. Hemingway, Molecular weight profiles of proanthocyanidin polymers, *Phytochemistry*. 22 (1983) 569–572.
- [20] D.C. Marcano, D.V. Kosynkin, J.M. Berlin, A. Sinitskii, Z. Sun, A. Slesarev, L.B. Alemany, W. Lu, J.M. Tour, Improved synthesis of graphene oxide, *ACS Nano*. 4 (2010) 4806–4814. <https://doi.org/10/bp734k>.
- [21] B. Yu, J. Xu, J.-H. Liu, S.-T. Yang, J. Luo, Q. Zhou, J. Wan, R. Liao, H. Wang, Y. Liu, Adsorption behavior of copper ions on graphene oxide–chitosan aerogel, *Journal of*

Environmental Chemical Engineering. 1 (2013) 1044–1050.
<https://doi.org/10.1016/j.jece.2013.08.017>.

[22] A.M. Behrens, M.J. Sikorski, T. Li, Z.J. Wu, B.P. Griffith, P. Kofinas, Blood-aggregating hydrogel particles for use as a hemostatic agent, *Acta Biomaterialia*. 10 (2014) 701–8. <https://doi.org/10.1016/j.actbio.2013.10.029>.

[23] K. Quan, G. Li, D. Luan, Q. Yuan, L. Tao, X. Wang, Black hemostatic sponge based on facile prepared cross-linked graphene, *Colloids and Surfaces B: Biointerfaces*. 132 (2015) 27–33. <http://dx.doi.org/10.1016/j.colsurfb.2015.04.067>.

[24] M.F. Shih, M.D. Shau, M.Y. Chang, S.K. Chiou, J.K. Chang, J.Y. Cherng, Platelet adsorption and hemolytic properties of liquid crystal/composite polymers, *International Journal of Pharmaceutics*. 327 (2006) 117–25. <https://doi.org/10.1016/j.ijpharm.2006.07.043>.

[25] M. Jerez, J. Sineiro, M.J. Nuñez, Fractionation of pine bark extracts: selecting procyanidins, *European Food Research and Technology*. 229 (2009) 651–659.

[26] D.W. Lee, L. De Los Santos V, J.W. Seo, L.L. Felix, A. Bustamante D, J.M. Cole, C.H.W. Barnes, The Structure of Graphite Oxide: Investigation of Its Surface Chemical Groups, *The Journal of Physical Chemistry B*. 114 (2010) 5723–5728. <https://doi.org/10.1021/jp1002275>.

[27] T.N. Blanton, D. Majumdar, X-ray diffraction characterization of polymer intercalated graphite oxide, *Powder Diffraction*. 27 (2012) 104–107. <https://doi.org/10.1017/S0885715612000292>.

[28] X. Song, X. Huang, Z. Li, Z. Li, K. Wu, Y. Jiao, C. Zhou, Construction of blood compatible chitin/graphene oxide composite aerogel beads for the adsorption of bilirubin, *Carbohydrate Polymers*. 207 (2019) 704–712.

[29] D. Popa, Z. Sun, F. Torrisi, T. Hasan, F. Wang, A. C. Ferrari, Sub 200 fs pulse generation from a graphene mode-locked fiber laser, *Applied Physics Letters*. 97 (2010) 203106. <https://doi.org/10.1063/1.3517251>.

[30] A.C. Ferrari, Raman spectroscopy of graphene and graphite: Disorder, electron–phonon coupling, doping and nonadiabatic effects, *Solid State Communications*. 143 (2007) 47–57. <https://doi.org/10.1016/j.ssc.2007.03.052>.

[31] A.C. Ferrari, D.M. Basko, Raman spectroscopy as a versatile tool for studying the properties of graphene, *Nature Nanotechnology*. 8 (2013) 235–246. <https://doi.org/10.1038/nnano.2013.46>.

- [32] A. Zając, J. Hanuza, M. Wandas, L. Dymińska, Determination of N-acetylation degree in chitosan using Raman spectroscopy, *Spectrochimica Acta Part A: Molecular and Biomolecular Spectroscopy*. 134 (2015) 114–120. <https://doi.org/10.1016/j.saa.2014.06.071>.
- [33] Z. Xu, R. Peng, X. Chen, R. Ghosh, H.P.V. Rupasinghe, Isolation of flavonoids from apple peel using novel graphene oxide cotton fiber, *Natural Product Research*. 31 (2017) 2559–2563.
- [34] M. S. Dresselhaus, A. Jorio, R. Saito, Characterizing Graphene, Graphite, and Carbon Nanotubes by Raman Spectroscopy, *Annual Review of Condensed Matter Physics*. 1 (2010) 89–108. <https://doi.org/10.1146/annurev-conmatphys-070909-103919>.
- [35] R.E. Shroder, R.J. Nemanich, J.T. Glass, Analysis of the composite structures in diamond thin films by Raman spectroscopy, *Physical Review. B, Condensed Matter*. 41 (1990) 3738–3745.
- [36] Adarsh Kaniyoor, Sundara Ramaprabhu, A Raman spectroscopic investigation of graphite oxide derived graphene, *AIP Advances*. 2 (2012) 032183. <https://doi.org/10.1063/1.4756995>.
- [37] L.M. Malard, M.A. Pimenta, G. Dresselhaus, M.S. Dresselhaus, Raman spectroscopy in graphene, *Physics Reports*. 473 (2009) 51–87. <http://dx.doi.org/10.1016/j.physrep.2009.02.003>.
- [38] C. emsp14N emsp14R Rao, A. emsp14K Sood, K. emsp14S Subrahmanyam, A. Govindaraj, Graphene: the new two-dimensional nanomaterial, *Angewandte Chemie International Edition*. 48 (2009) 7752–7777. <https://doi.org/10.1002/anie.200901678>.
- [39] M. Fang, K. Wang, H. Lu, Y. Yang, S. Nutt, Single-layer graphene nanosheets with controlled grafting of polymer chains, *Journal of Materials Chemistry*. 20 (2010) 1982–1992.
- [40] J.L. Brash, T.A. Horbett, R.A. Latour, P. Tengvall, The blood compatibility challenge Part 2: protein adsorption phenomena governing blood reactivity, *Acta Biomaterialia*. (2019).
- [41] D. Han, L. Yan, Supramolecular hydrogel of chitosan in the presence of graphene oxide nanosheets as 2D cross-linkers, *ACS Sustainable Chemistry & Engineering*. 2 (2014) 296–300.

[42] R. Jayakumar, M. Prabakaran, P.S. Kumar, S.V. Nair, H. Tamura, Biomaterials based on chitin and chitosan in wound dressing applications, *Biotechnology Advances*. 29 (2011) 322–337.

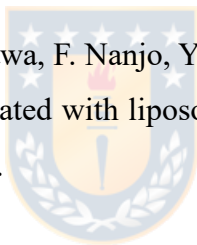
[43] H. Babich, M.E. Krupka, H.A. Nissim, H.L. Zuckerbraun, Differential in vitro cytotoxicity of (-)-epicatechin gallate (ECG) to cancer and normal cells from the human oral cavity, *Toxicology in Vitro*. 19 (2005) 231–242.

[44] J. Boateng, O. Catanzano, Advanced Therapeutic Dressings for Effective Wound Healing--A Review, *Journal of Pharmaceutical Sciences*. 104 (2015) 3653–80. <https://doi.org/10.1002/jps.24610>.

[45] A.G. Erlejman, C.G. Fraga, P.I. Oteiza, Procyanidins protect Caco-2 cells from bile acid-and oxidant-induced damage, *Free Radical Biology and Medicine*. 41 (2006) 1247–1256.

[46] S.A. Agnihotri, N.N. Mallikarjuna, T.M. Aminabhavi, Recent advances on chitosan-based micro-and nanoparticles in drug delivery, *Journal of Controlled Release*. 100 (2004) 5–28.

[47] T. Hashimoto, S. Kumazawa, F. Nanjo, Y. HARA, T. NAKAYAMA, Interaction of tea catechins with lipid bilayers investigated with liposome systems, *Bioscience, Biotechnology, and Biochemistry*. 63 (1999) 2252–2255.



6 Conclusions

The results obtained from the topics explored in this work allow us to conclude that the materials developed were able to adsorb the grape extracts thanks to π - π stacking in the planar graphene oxide zones and electrostatic interactions with graphene oxide and chitosan. It was then shown that the loaded grape extract was released into the simulated physiological environment, and both materials released an amount comparable with those reported in existing studies (20% nanocomposite and 12% aerogel by weight).

The materials loaded with grape extract were not cytotoxic to human kidney cells at the concentrations tested and were also not cytotoxic against human dermal fibroblast. This is due to the compatibility of chitosan and its interaction with graphene oxide and the extract.

The synthesized graphene oxide and chitosan based aerogel show enhanced roughness and stiffness structures with grape seed and skin extracts. Due to the rich presence of flavan-3-ols and electrostatic interactions, the aerogels could promote blood absorption and red blood cells accumulation, revealing potential as hemostatic agents. The cell viability results for the aerogels also show a difference in the type of extract used, whether the extract is from seed or skin of the grapes, with grape skin extract being less cytotoxic than seed extract. This effect was attributed to its degree of polymerization and to the composition of the subunits of the proanthocyanidins, which have different monomers according to the extract origin.

Thus, this work delivers two materials capable of effectively transporting the phyto drug to physiological media with good cell viability since each one achieved the following conditions:

In the case of the covalently functionalized nanocomposite of GO with CS.

- The nanocomposite GO-CS was found to be thermally stable, which can be suspended in a physiological medium with a negative surface charge due to the oxygenated groups on the extract and graphene oxide.
- The extract was loaded in the nanocomposite with efficiency compared to literature and then released into a simulated physiological medium.
- The nanocomposite and extract complex was not cytotoxic against human kidney cell models (HEK 293).

In the case of the graphene oxide and chitosan based aerogels with added extract:

- Results highly porous and rigid, with negative surface charge and the capacity to absorb water, PBS and blood.

- The addition of extract increased the negative charge of the aerogels surface, their stiffness, and change their 3D structure, making them more porous. Also, part of the extract was released to physiological media.
- The loaded aerogel proved to be no cytotoxic to human dermal fibroblasts.

6.1 The direction of future work

In this work, progress was made in predicting the biocompatibility of synthesized materials, but more extensive studies are needed to be able to define this property. It would be vital to complete cytotoxic studies at different times of incubation, and also be able to perform in-vivo tests of the optimal samples shown in this work to see their effect on animals before their use in humans. Studies could be made of the bioactivities of the transported extract comparing with the injected and ingested via of administration, to see if any bioactivity is affected by being carried in these composites.

6.2 Publications

- Mellado, C., Figueroa, T., Báez, R., Castillo, R., Melendrez, M., Schulz, B., & Fernández, K. (2018). Development of graphene oxide composite aerogel with proanthocyanidins with hemostatic properties as a delivery system. *ACS applied materials & interfaces*, 10(9), 7717-7729.
- Mellado, C., Figueroa, T., Baez, R., Melendrez, M., & Fernandez, K. (2019). Effects of probe and bath ultrasonic treatments on graphene oxide structure. *Materials Today Chemistry*, 13, 1-7.
- Figueroa, T., Aguayo, C., & Fernández, K. (2020). Design and Characterization of Chitosan-Graphene Oxide Nanocomposites for the Delivery of Proanthocyanidins. *International Journal of Nanomedicine*, 15, 1229.
- Borges-Vilches, J., Figueroa, T., Guajardo, S., Meléndrez, M., & Fernández, K. (2020). Development of gelatin aerogels reinforced with graphene oxide by microwave-assisted synthesis: influence of the synthesis conditions on their physicochemical properties. *Polymer*, 122951.

6.3 Posters and Presentations

- Primer taller chileno de materiales de carbono (TChMC 2018), April 2018, Valparaiso, Chile. “Citotoxicidad de nanopartículas a base de óxido de grafeno y quitosano cargadas con proantocianidinas”, Oral presentation. (Third place winner for best presentation).
- VI Congreso Internacional de Biomateriales, March 2018, La Habana, Cuba. “Synthesis and characterization of biocompatible polymer and Graphene oxide-based nanoparticles for drug delivery” and “Chitosan-graphene oxide aerogels synthesis for drug delivery”.
Oral presentations
- V Curso Internacional de Biomateriales, March 2018, La Habana, Cuba.
- Segundo Taller Latinoamericano sobre materiales carbonosos (TLMC 2), December 2016, Termas de Chillán, Chile. Attendee.
- 13° Simposio en compuestos Bio-Basados en la Cuenca del pacífico Biocomp 2016, November 2016, Concepción, Chile. Attendee
- 15° Congreso internacional de metalurgia y materiales, Dicember 2015, Concepción, Chile. “Estudio termogravimétrico de nanopartículas biocompatibles cargadas con proantocianidunas de Uvas”. Oral presentation.

7 Appendix A

This chapter contains supplementary information to chapter 3



7.1 Phloroglucinolysis

A solution of 0.1 mol eq./HCl in methanol containing 50 g L⁻¹ of phloroglucinol was reacted with the seed and skin extracts (5 g L⁻¹) at 50°C for 20 min. Then, the mixture was combined with 5 volumes of aqueous sodium acetate 40 mM, to stop the reaction. The procedure was performed in duplicate for all tested samples. The compounds were detected with an HPLC Merck-Hitachi chromatograph LaChrom L7000 Series, with a gradient pump L-7100, Autosampler L-7200, UV detector L-4250 (wavelength 280 nm) and two Chromolith Performance Series RP-18e columns (Merck, Darmstadt, Germany). The mobile phase consisted of Milli-Q water with 1% v/v aqueous acetic acid (mobile phase A) and acetonitrile with 1% v/v acetic acid (mobile phase B) and elution was performed with 3% B for 4 min. The linear gradients used were 3–18% B for 14 min and 80% B for 2 min at a flow rate of 3 mL min⁻¹ and 30°C. The column was washed with 3% B for 2 min before the next injection was performed. To quantify the samples, an external standard of catechin (100 mg of C L⁻¹) was used. The extract characterization gave values of mean degree of polymerization (mDP), average molecular weight (aMW), the proportion of their components ((+)-catechin (C), (-)-epicatechin (EC), (-)-epigallocatechin (EGC), (-)-epicatechingallate (ECG), (-)-epicatechin-phloroglucinol (EC-P), (d)-epicatechingallatephloroglucinol (ECG-P), (d) epigallocatechin-phloroglucinol (EGC-P)), yield (>80 g 100 g⁻¹), and concentration.

Table 7-1 Structure composition, mean degree of polymerization (mDP), average molecular weight (aMW) and concentration of the grape extract.

Compound ^a	Extract
C	166 ± 13
EC	88 ± 3
ECG	445 ± 18
C-P	459 ± 18
EC-P	2937 ± 46
ECG-P	1604 ± 19
EGC-P	nd
mDP ^b	9.2 ± 0.3
aMW ^c	3019 ± 87
PAs content ^d	329.5 ± 6.7

nd: not detected. (C) (+)-catechin. (EC) (-)-epicatechin. (EGC) epigallocatechin. (C-P) (+)-catechin-phloroglucinol. (EC-P) (-)-epicatechin-phloroglucinol. (ECG-P) epicatechin gallate-phloroglucinol. (EGC-P) epigallocatechin-phloroglucinol. Values are mean±standard deviation (n=2)

^a Flavan-3-ol subunit expressed as micromolar (μM) of (+)-catechin equivalents.

^b Mean degree of polymerization dimensionless.

^c Average molecular weight of PA.

^d Total Proanthocyanidin concentration in the extract ($\text{mg CE (g extract)}^{-1}$).

7.2 Gel permeation chromatography (GPC).

Samples (50 mg) were acetylated with pyridine and acetic anhydride (2 mL, 1:1, v/v) overnight at room temperature. The solvents were evaporated and the acetylated extracts were dissolved in tetrahydrofuran THF (10–15 mg mL⁻¹), and the molecular weight distribution of the extracts was determined with the HPLC (ACME 9000, Young Lin Instrument Co. Ltd., Anyang, Korea) which was equipped with a UV/VIS detector and two PSS SDV gel columns (5 μm, 100 and 500 Å) of 30 cm and a PSS SDV gel precolumn (5 μm) equilibrated at 23°C. Analytes were detected at 254 nm at a flow rate of 1 mL min⁻¹ of the mobile phase (THF) and with an injection volume of 20 μL. Ten standards of polystyrenes with different molecular weights were used, Mw 162–19,950 Da.

Table 7-2 Molecular weight distribution of grape seed extract

Molecules percentage (%)	Molecular weight range (g mol ⁻¹)
15.9	21928-13944
25.1	13944-9263
58.9	9263-800

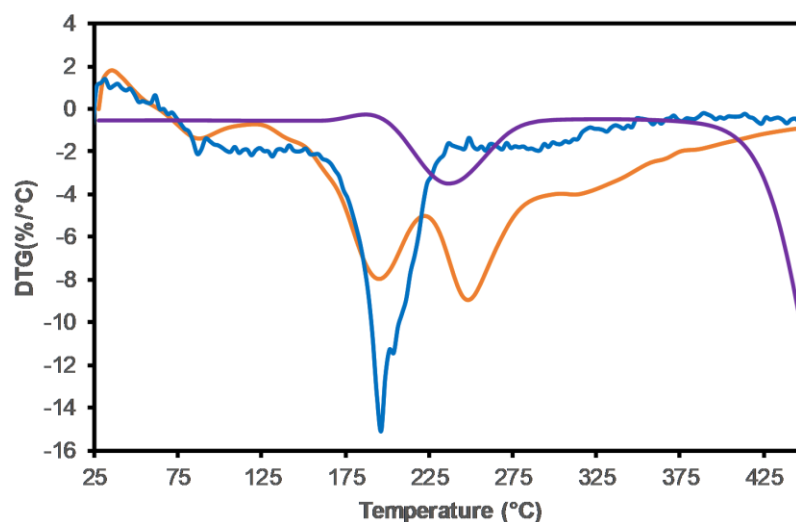


Figure 7-1 DTG curves of GO (blue), CS (purple) and GO-CS (orange).

8 Appendix B

This chapter contains supplementary information to chapter 4



Table 8-1 Structure composition, mean degree of polymerization (mDP), average molecular weight (aMW) and concentration of the grape extract.

Compound ^a	Skin	Seed
C	156 ± 22	166 ± 13
EC	nd	88 ± 3
ECG	nd	445 ± 18
C-P	92 ± 5	459 ± 18
EC-P	2900 ± 152	2937 ± 46
ECG-P	267 ± 15	1604 ± 19
EGC-P	574 ± 46	nd
mDP ^b	25.5 ± 0.8	9.2 ± 0.3
aMW ^c	7565 ± 221	3019 ± 87
PAs content ^d	230.6 ± 14.7	329.5 ± 6.7

nd: not detected. (C) (+)-catechin. (EC) (-)-epicatechin. (EGC) epigallocatechin. (C-P) (+)-catechin-phloroglucinol. (EC-P) (-)-epicatechin-phloroglucinol. (ECG-P) epicatechin gallate-phloroglucinol. (EGC-P) epigallocatechin-phloroglucinol. Values are mean±standard deviation (n=2)

^a Flavan-3-ol subunit expressed as micromolar (μM) of (+)-catechin equivalents.

^b Mean degree of polymerization dimensionless.

^c Average molecular weight of PA.

^d Total Proanthocyanidin concentration in the extract (mg CE (g extract)⁻¹).

Table 8-2 Molecular weight distribution of grape seed extract

Molecules percentage (%)	Molecular weight range (g mol ⁻¹)
Grape Seed Extract	
15.9	21928-13944
25.1	13944-9263
58.9	9263-800
Grape Skin Extract	
10.5	25807 – 14149
22.7	14149 – 8866
55.9	8866 – 1582
3.8	1582 – 1156
3.9	1156 - 791
3.1	791 - 451



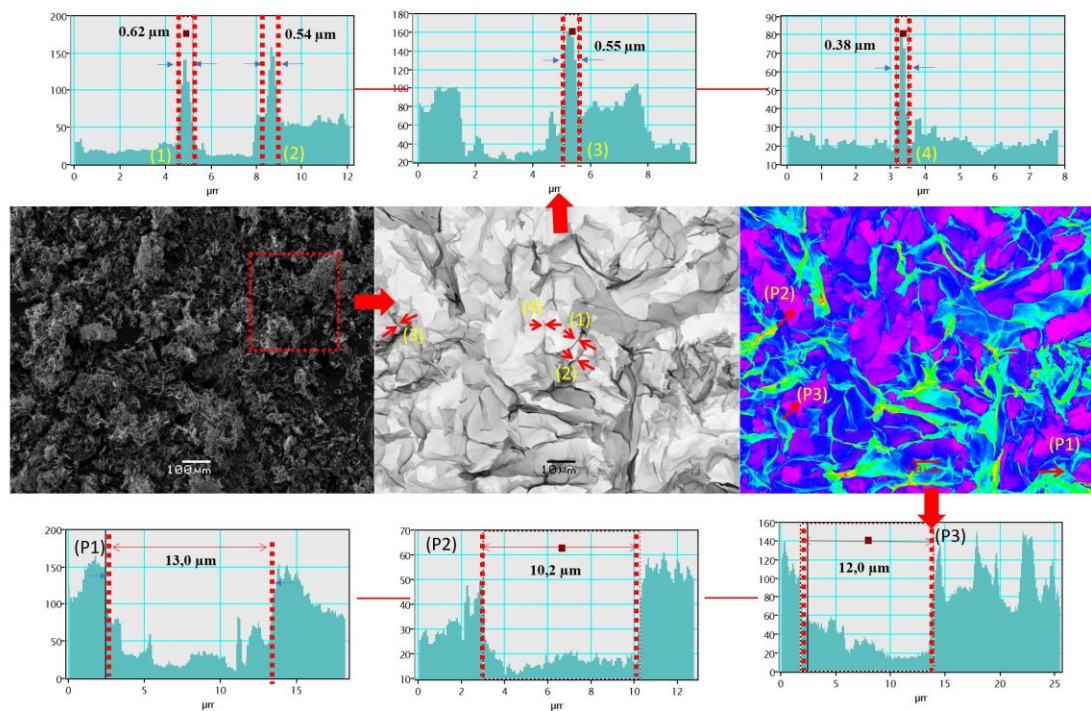


Figure 8-1 Outline of the method for determining the pore size of aerogels (P1), (P2) and (P3) are the pore size determined from the SEM image using contrast comparison, and (1), (2), (3) and (4) are the determination of the wall width of the 3D aerogel structures